Photonic Engineering for Atom Based Quantum Sensors

By

Xuting Yang

A dissertation submitted in partial fulfillment of

the requirements for the degree of

Doctor of Philosophy

(Materials Science & Engineering)

at the

UNIVERSITY OF WISCONSIN-MADISON

2024

Date of final oral examination: 12/17/2024

The dissertation is approved by the following members of the Final Oral Committee:

Jennifer Choy, Assistant Professor, Electrical & Computer Engineering

Mikhail Kats, Professor, Electrical & Computer Engineering

Paul Evans, Professor, Materials Science & Engineering

Ramathasan Thevamaran, Associate Professor, Mechanical Engineering

Deniz Yavuz, Professor, Physics

Photonic Engineering for Atom Based Quantum Sensors

Xuting Yang

Abstract

Quantum sensing exploits the quantum properties of matter, such as superposition and entanglement, to measure physical quantities with exceptional accuracy. Neutral atoms, with their long coherence times and ability to interact strongly with their surroundings, are ideal for applications in timekeeping, magnetometry, and inertial sensing. Despite their potential, neutral atom quantum sensors are not widely deployed due to high implementation costs and operational complexity. The lasers and optics required to manipulate atomic states often occupy more space than the sensing unit. Nanophotonics offers unique opportunities to miniaturize atomic sensors by enabling precise light control at subwavelength scales, enhancing atom-light interaction and boosting sensor performance.

In this work, I report our research on photonic integration of atomic sensors, with specific focus on passive metasurface optics tailored for quantum sensing applications. I have designed multiple metasurfaces which can play important roles in the optical measurements of neutral atom quantum systems, including waveplates, polarizing beam splitters and lenses with polarization-dependent deflection. I have identified silicon on sapphire (SOS) as a suitable material platform for metasurface optics aimed at wavelengths that atomic sensors commonly operated in, with excellent optical, mechanical and thermal properties and CMOS-compatibility. Together with my collaborators, we then fabricated metasurface polarizing beam splitter (PBS) and bottle beam trap generator that enables miniaturized atomic sensors. We characterized the optical performance of the metasurface devices and confirmed their functionalities, in agreement with our simulations. Next, I developed a multi-physics model that connects the optical performance of the metasurface components with the atomic sensing performance that demonstrated the feasibility and limitation of metasurface integration in atomic sensors, and realized nanophotonic integration in a nonlinear magneto-optical rotation rubidium magnetometer, with the above metasurface PBS detecting the optical rotation as magnetometry signal, and achieved an integrated sub-nanotesla sensitivity across a detection bandwidth of 500 kHz. Finally, I report our progress on building a cold-atom gravimeter as the testbed for nanophotonic integration with cold-atom systems and describe our future plans to integrate the cold-atom setup with nanophotonic components to miniaturize the optical system and boost the sensitivity of cold-atom sensors.

Acknowledgement

First, I would like to express my heartfelt gratitude to my advisor, Dr. Jennifer Choy. When I first reached out to her as a new graduate student, I was quickly impressed by her depth of knowledge in quantum physics and enthusiasm in quantum sensing. But what made me finalize the decision to officially join her group is her unwavering kindness and genuine care for her students, which became obvious from day one. She has always been considerate of the challenges her students face, no matter if they come from coursework, research or life, and willing to offer her help. During the COVID-19 pandemic when funding and equipment challenges arose, she would try her best to advocate for her students and find solutions to keep our project moving forward. In addition to academic guidance, she has been committed to my personal and professional development, constantly seeking opportunities like academic exchanges, workshops, and career fairs for me to participate in, and connecting me with people in academia and industry, which opened doors that might otherwise have been inaccessible. I feel incredibly fortunate to have had the opportunity to work under her guidance, and her example will continue to inspire me in my future endeavors.

I would also like to thank my wonderful colleagues, without whom this work would not be possible. I am deeply grateful to Steven Carpenter, who was actively involved and contributed to nearly every part of the cold atom experiment, including the vacuum setup, lasers, optics and electronics. Steven is a brilliant experimentalist with an incredible ability to devise solutions even with limited resources. His dedication and expertise have been invaluable to the success of our experiments. I also want to thank Pree Mukherjee for her significant contributions to the metasurface simulation, characterization and atomic magnetometry experiment, as well as her help with the cold atom interferometry setup, particularly the new experiment control system. Pree's quick learning ability and her collaborative spirit have made her an indispensable member of the team, and I have no doubt she will continue to excel in future research projects. Additionally, I am immensely grateful to all other group members, who have helped me both in research and in life. Their valuable advice, constructive feedback, and unwavering support have been instrumental in shaping this work. They have cultivated a positive and inspiring group environment, which has made this journey enriching and rewarding.

I would like to extend my gratitude to our collaborators for their significant contributions to this work. Professor Mikhail Kats and his research group provided invaluable support with nanophotonic design, simulation, characterization, and testing. I am also deeply thankful to Dr. Alan Dibos and Dr. Dave Czaplewski from Argonne National Laboratory for their exceptional work in fabricating our metasurface devices. Additionally, I sincerely appreciate the assistance and insightful advice offered by Professor Deniz Yavuz, Professor Mark Saffman, and their group members, which greatly benefited our cold atom experiment.

This work is supported by the Office of Naval Research (N00014-20-1-2598), National Science Foundation QuSeC-TAQS (2326784) and Wisconsin Alumni Research Foundation (WARF).

Contents

List of Figures

List of Tables

1 Introduction

1.1 Background and motivation

Quantum sensing utilizes the intrinsic energy levels in quantum systems (which can be atoms, trapped ions, defects in solid, etc.) to measure classical or quantum physical quantities. Owing to their extreme sensitivities to external perturbations and the fact that their response or behavior towards such perturbations can be well modeled and predicted, unprecedented measurement precision and sensitivity has been achieved. The application of quantum systems to sensing is unique in the field of quantum technologies in the sense that it capitalizes on the weakness of quantum system: their fragility towards external perturbance and noises, which remains the greatest obstacle in quantum computing and quantum communication (Degen, Reinhard, & Cappellaro, 2017). Such an intriguing aspect of quantum sensing is partially why it is the most mature field of quantum technologies and has already enjoyed decades of fruitful research and developments before it emerges as a distinct field of research, with successful applications including atomic clocks, high resolution spectroscopy and superconducting quantum interference devices (Degen, Reinhard, & Cappellaro, 2017).

Among all the quantum objects utilized as sensors, neutral atoms stand out as a promising platform since they enjoy the following advantages: (1) each atom being identical with no imperfections; (2) no performance degradation over time; (3) long coherence time in isolated environments (vacuum, vapor cell, etc.); (4) the ability to form strong interaction with environment (ex. Rydberg atoms). As a result, unparalleled sensing performances have been demonstrated in neutral atom sensors. Prominent examples of achievements in atomic sensing and metrology include vapor cell magnetometry with sub-femto tesla level sensitivity (Bui Dang & Romalis, 2009), atomic clock with extremely low systematic uncertainty (Aeppli, Kim, Warfield, Safronova, & Ye, 2024) and atomic inertial sensor with high sensitivity and stability (Battelier, et al., 2016; Wright, et al., 2022; Garrido Alzar, 2019).

Despite their performance in research labs, atomic sensors are not yet widely used in real world applications. This is unfortunately due to their high cost and complexity in instrumentation. For quantum sensing to be successfully implemented, the following procedures are necessary: (1) state initialization; (2) coherent manipulation of the quantum states; (3) state readout. For neutral atoms, these steps are typically accomplished through optical excitation. Therefore, free space lasers and optics are widely implemented in atomic sensing systems, which tend to occupy enormous amount of space together with their control electronics and are costly and power hungry. Moreover, the atomic medium in an atom-based sensor is often required to be isolated from environmental factors that lead to performance deteriorations and needs to reside in surroundings with well-controlled parameters. Consequently, special experiment chambers and cells, vacuum apparatus and electromagnetic sheidings are often necessary, resulting in serious encumbrance and footprints. Conversely, many classical sensors or quantum sensors based on other mediums have enjoyed

successful real-life applications due to their simple infrastructures, low operation complexity, mass fabrication potential as well as high dynamic range and bandwidth. For example, compared to atomic magnetometers, magnetometers based on fluxgate, Hall effect and magnetoresistance dominate the market as they can be mass fabricated with integrated-circuit technology and integrated into other devices and systems as electronic components. For applications involving ultralow field and ultrahigh sensitivity, SQUIDs enjoy the advantages in dynamic range and bandwidth (Grosz, Haji-Sheikh, & Mukhopadhyay, 2017; Huber, et al., 2001; Cantor, Lee, Matlashov, & Vinetskiy, 1997).

Miniaturization and integration of atomic sensors to bring down their size, cost and complexity in installation would therefore be an essential step to achieve commercial success and widespread application. Various research efforts have been made towards this goal, including breakthroughs in microfabricated vapor cells (Liew, et al., 2004; Wang, Chekhova, & Kivshar, 2022), chip-scale photonic technologies such as VCSELs (Koyama, 2006; Ledentsov, et al., 2022), and scaled-down vacuum apparatus (Basu & Velásquez-García, 2016). However, the arguably most important and promising step lies in the integration of nanophotonic components with atomic systems. The immense amount of photonic and optical elements necessary for the generation of laser beams with precisely controlled direction, intensity, polarization and wavefront can easily take up a large amount of the total sensor volume. Replacing these elements with potentially foundry compatible, nano-scale photonic components thus offers a straightforward method in reducing the size of atomic sensors as well as improving their reliability. On the other hand, the flexibility and customizability of manipulating the behavior of electromagnetic waves offered by nanophotonics can be beneficial in optimizing atom-light interaction that is essential in boosting the performance of atom-based sensors.

Atomic magnetometer works by detecting the property change of light that is resonantly coupled with an atomic medium exposed to the external magnetic field. The atomic medium is prepared in a magnetic-sensitive state through optical pumping, and the magnetic field information encoded in atomic state is extracted from the stokes parameters of the probe laser or from laser-induced fluorescence. To the best of our knowledge, the first nanophotonic integration attempt for atomic magnetometry was made by Y. Sebbag et al. in 2020 (Sebbag, Naiman, Talker, Barash, & Levy, 2020). Operating on the nonlinear magneto-optical rotation based magnetometry scheme, they fabricated a guided wave photon spin sorter (PSS) which resolved the handedness of the incident photon by directing them into two separate waveguides. Magnetic field information encoded in circular dichroism was then retrieved by a differential intensity measurement of the output of the two waveguides. In a follow up paper, they improved their PSS design to a more convoluted structure generated by inverse design using a direct-binary-search (BDS) algorithm (Sebbag, Talker, Naiman, Barash, & Levy, 2021). The figure of merit (FOM) was set to be the coupling efficiency of the circular polarized light into the fundamental modes of the collecting waveguides. The new design demonstrated effective spin-sorting capability with improved polarization distinction ratio. Using a microfabricated Rubidium vapor cell with an interaction

volume of 300 μm^3, a magnetic sensitivity of 700 $pT \cdot Hz^{-1/2}$ was reported. Recently, a variety of nanophotonic components have been proposed or realized for atomic magnetometry, including polarization splitting grating coupler (Hu, et al., 2022), spin-selective dielectric metasurface (Xu, et al., 2024; Talker, et al., 2022), metasurface polarizing beam splitter (Hu, et al., 2024), beam deflecting metasurface (Liang, et al., 2022) and metasurface-based optical system (Li, et al., 2024).

Owing to their extremely long coherence time and length, cold atom-based quantum sensors have enabled measurements of physical quantities with unparalleled precision and accuracy. The rapid development of cooling and confining techniques for netural atoms has enabled the significant reduction in uncertainties associated with Doppler shifts and AC stark effects, leading to optical lattice clocks with unprecedented precision (Aeppli, Kim, Warfield, Safronova, & Ye, 2024). For magnetic field sensing, well-controlled, highly localized cold atom clouds have enabled all-optical magnetometry measurements with high precision and micrometer scale spatial resolution and could lead to potential applications in magnetic field mapping and field rectification in neutral atom quantum science (Schäffner, Schreiber, Lenz, Schlosser, & Birkl, 2024). Despite their revolutionary potential, the employment of cold atom quantum sensors outside of controlled lab environments has been challenging because of the complexity associated with the optical setup for the necessary cooling and trapping processes to produce a well-controlled cold atom medium. Moreover, the large number of optical elements involved render the whole sensor system vulnerable to thermomechanical instability that leads to alignment deterioration. Therefore, nanophotonic research aiming at reducing the complexity of the optical system for cold atom sensors has been an active area of interest. Prominent examples include diffractive gratings for magneto-optical trap (MOT) (Vangeleyn, Griffin, Riis, & Arnold, 2010; Nshii, et al., 2013; McGilligan, et al., 2017; McGehee, et al., 2021; Chen, et al., 2022), integrated photonic circuit based beam delivery for 3D-MOT (Isichenko, et al., 2023) and metasurface for generation of cold atoms and atom traps (Hu & Li, 2024; Huang, et al., 2024).

1.2 Overview of this work

The optical engineering with nanophotonic components on quantum systems for various applications have undergone dramatic advancements thanks to recent developments in materials science, fabrication techniques, laser and optical technology, electronics and computational algorithms. In collaboration with several researchers and groups, we have successfully developed and improved fabrication techniques and characterization methods on single crystalline silicon-on-sapphire (SOS) platform for our transmissive metasurface optics and are able to fabricate millimeter scale metasurfaces efficiently with highly replicable results. Thanks to the spectroscopic ellipsometry techniques developed by Kats group, we have successfully obtained the complex refractive index across the visible and NIR spectrum for the SOS material as well as the thickness distribution of the SOS wafers, confirming their high optical quality and excellent uniformity and flatness. The optical data obtained are crucial in our design and simulation of

metasurface devices that operate across a variety of laser wavelengths, and demonstrated the suitability of SOS as a material platform for integrating with atomic sensors. I have designed and simulated multiple metasurface optics tailored for neutral atom based quantum applications, including a polarizing beam splitter (PBS) and a metalens with polarization sorting capability for magnetometry signal detection in rubidium based atomic magnetometers and a quarter and half waveplate operating at rubidium D1 transition. In addition, we succeeded in fabricating and characterizing millimeter scale metasurface PBS for magnetometry and bottle beam trap array generator for atom trapping in quantum computing applications, and confirmed their optical performances, including transmission, beam deflection efficiency, output polarization state and intensity profile.

Building on the success of metasurface fabrication, I have demonstrated atomic magnetometry using the metasurface PBS on the SOS platform. To our knowledge, this is the first demonstration of silicon-on-sapphire metasurface integration on an atomic magnetometer. First, I developed a multi-physics model capable of predicting the performance of metasurface-incorporated atomic magnetometer based on the measured/simulated optical parameters of the metasurface optics and the physics model of the adopted atomic magnetometry scheme, demonstrating the feasibility of integrating the metasurface PBS into in-line atomic magnetometers such as single beam spin exchange relaxation free (SERF) (Shah & Romalis, 2009) and nonlinear magneto-optical rotation (NMOR) magnetometers (Budker D. , Kimball, Rochester, Yashchuk, & Zolotorev, 2000) while maintaining their field sensitivity. We have then succeeded in achieving a integrated sub-nT sensitivity NMOR magnetometer with the magnetic optical rotation signal being detected by the metasurface PBS, which is impressive considering we did not incorporate any modulation techniques with phase sensitive detection and the detection bandwidth was over $0.5\ MHz$. We analyzed the experiment data and found out that the sensitivity was limited by laser and detector noise, and that the sensitivity can be improved further with a AR coated metasurface.

Finally, we present our work on achieving a robust, compact and high performing cold atom gravimeter based on Raman pulse. With the help of my colleagues and collaborators, I have succeeded in building our lab's first cold atom infrastructure, including the vacuum system, laser system and optical setup, RF electronics and experimental control instruments. We have realized both rubidium 85 and 87 magneto-optical traps (MOT) in the setup with temperature characterization using time-of-flight (TOF) measurement, and implemented polarization gradient cooling (PGC), obtaining rubidium 87 ensembles with sub-doppler temperatures, which is a crucial step towards high contrast cold atom interferometry. We have laid out future plans for achieving state preparation and interferometry sequence for measuring gravity and implementing nanophotonic integration to the cold atom gravimeter, including diffraction grating MOT (GMOT), metasurface optics for fluorescence detection/imaging/beam shaping and chip scale narrow linewidth laser for compactifying the laser system.

1.3 Thesis organization

This thesis is presented as follows. In chapter 2, we detail our design principles of metasurface optics and present examples of metasurface tailored for quantum applications in neutral atom systems, specifically focusing on the simulation, fabrication and optical characterization of the metasurface PBS for signal detection in atomic magnetometry and bottle beam trap generator for atom trapping in quantum computing. In chapter 3, we describe our effort in integrating metasurface polarizing optics in rubidium atomic magnetometers. We first present our theoretical analysis on the performance of metasurface incorporated atomic magnetometer, demonstrating the feasibility of the concept. We then realized a metasurface integrated atomic magnetometer based on nonlinear magneto-optical rotation with a detailed analysis on the sensitivity and noise sources. Finally, we describe our progress towards building the lab's first cold atom gravimeter, detailing the vacuum, optical and electronics system layouts, with experimental results of atom trapping and cooling. We then delve into future steps for the cold atom setup, including finishing the interferometry experiment, achieving grating MOT and integrating the gravimetry system with nanophotonic components, including metasurfaces and chip-scale lasers based on integrated photonics circuit technology. Chapter 5 concludes the thesis, with detailed future plans involving improving metasurface performance, implementing atomic interferometry experiments and integrating nanophotonics into the cold atom gravimetry system.

2 Transmissive, passive metasurface optics on silicon-on-sapphire platform for neutral atom based quantum applications

2.1 Introduction

Metasurfaces consist of planar, subwavelength scattering elements (meta-atoms) with size, shape, and orientation that can be tailored to modify the properties of the incoming light such as intensity, phase, wavefront, polarization and spectrum (Khorasaninejad, et al., 2016; Yu, et al., 2011). This in turn allows them to achieve the functions of conventional optics like waveplates, polarizers, lenses, gratings, prisms and filters. for complete control over the properties of the outgoing light, including polarization, phase, amplitude, and directionality. Metasurfaces present a tantalizing direction for polarization optics, which have historically relied on combinations of polarizers and birefringent waveplates (Ranjbar & Grbic, 2019), the latter of which require light propagation over the thickness of a birefringent material (typically many times longer than a wavelength) to achieve a desired phase delay between two orthogonal polarizations. Meanwhile, metasurfaces can enable this phase delay in an ultra-thin interface and provide an avenue for integrating multiple functionalities (e.g., Polarization and wavefront control) into a single device (Gao, Park, Lee, & Choi, 2019).

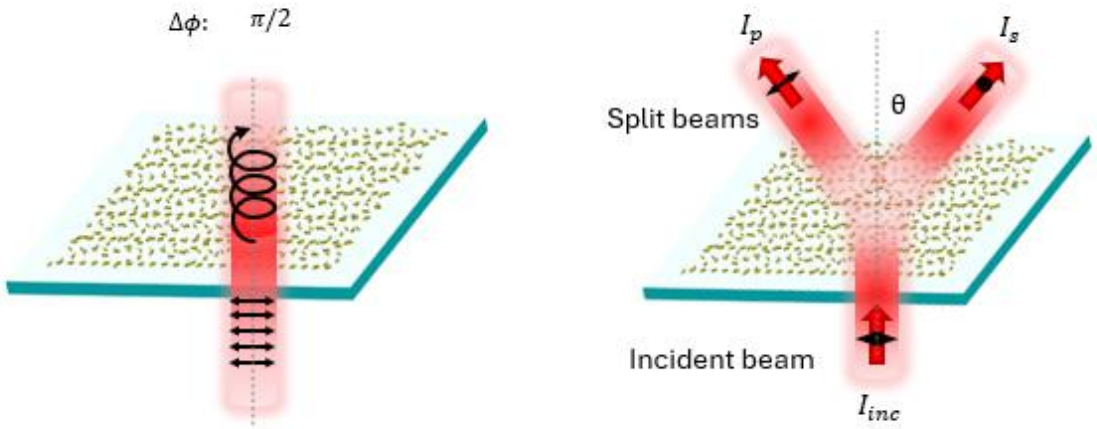

Figure 2-1 Metasurface is an engineered, two-dimensional (2D) array of subwavelength structures designed to manipulate electromagnetic waves in a precise manner. By adjusting the geometry, size, spacing, and material composition of these meta-atoms, metasurfaces can control various properties of incident electromagnetic waves, such as phase, amplitude, polarization, and direction.

Thanks to their extraordinary capabilities of manipulating electromagnetic fields at sub-wavelength scale, metasurfaces are playing an increasingly important role in quantum science and technologies, ranging from quantum computing, quantum simulation, quantum communication, quantum metrology and quantum memory (Tanuwijaya, et al., 2024; Bekenstein, et al., 2020; Wang, Chekhova, & Kivshar, 2022; Jiang & Henning, 2021). From directly participating in quantum processes such as generating and manipulating nonclassical state of light through nonlinear optical processes and enhancing light-matter interaction through local concentration of EM fields within small volumes, to compactify building blocks of optical systems in quantum applications to achieve necessary functions such as active light modulation, light coupling, beam splitting, polarization rotation and light focusing, the compact and versatile nature of metasurfaces, combined with their compatibility with integrated photonics, makes them a promising platform for the next generation of quantum technologies, facilitating the development of more scalable, efficient, and integrated quantum devices (Georgi, et al., 2019; Huang, et al., 2023; Santiago-Cruz, et al., 2022). Still, challenges remain in applying metasurfaces to quantum applications. The requirement of nanometer-scale precision in fabrication severely hinders their reliability and mass producibility (Seong, Jeon, Yang, Badloe, & Rho, 2024; Fu, Chen, Li, Yu, & Zheng, 2022). Furthermore, their extreme sensitivity to optical alignment and external disturbances makes their integration with quantum systems challenging and often requires advanced hybrid integration techniques (Solntsev, Agarwal, & Kivshar, 2021).

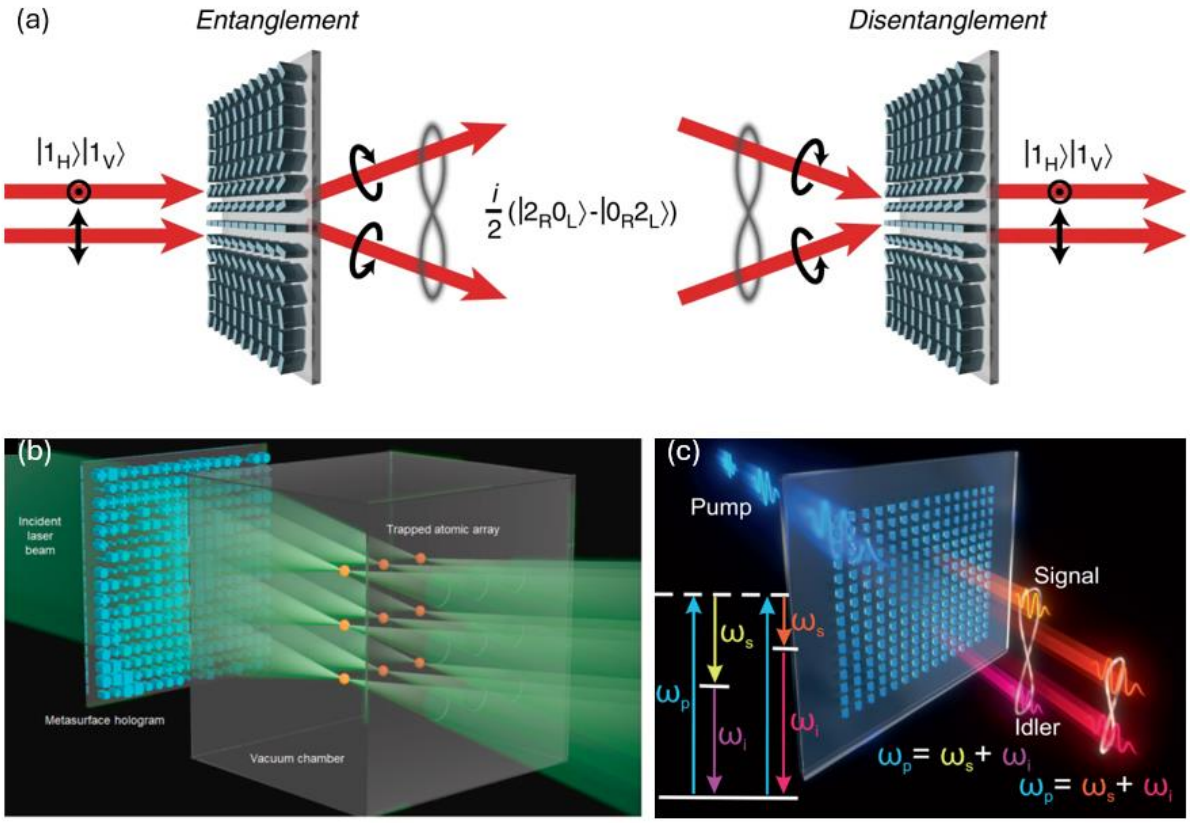

Figure 2-2 Examples of metasurface applications in quantum science and technology. (a): Spatial entanglement and disentanglement of a two-photon state at a metasurface *(reproduced from* (Georgi, et al., 2019)*)*; (b): Schematic illustration of a compact system to generate optical trap arrays for cold atoms using a metasurface hologram*(reproduced from* (Huang, et al., 2023)*)*; (c) Spontaneous parametric downconversion (SPDC) using symmetry-protected quasi-BIC resonances in a semiconductor metasurface*(reproduced from* (Santiago-Cruz, et al., 2022)*)*.

In recent years, there has been increased interest in all dielectric metasurfaces. Unlike plasmonic-type metasurfaces that suffer intrinsic ohmic loss, metasurfaces with high refractive index can achieve high efficiency and simultaneously manipulate both electric and magnetic multipole resonances, making them attractive candidates for efficient photonic devices (Hu, et al., 2020; Sautter, et al., 2015; Yang, Kravchenko, Briggs, & Valentine, 2014; Yang, et al., 2020; Wang, et al., 2018; Liu, et al., 2018). Figure 2.3 shows the complex refractive index of a common dielectric material - silicon. At near infrared wavelength region, silicon has great refractive index with relatively low absorption coefficient. As a result, efficient electric and magnetic dipole resonances can be excited within the silicon nanostrucutre which is crucial for amplitude, phase and polarization modulation required for metasurface devices. The high refractive index of silicon also means a full phase (2π) coverage can be easily achieved over sub-wavelength height structures, which is much easier to fabricate in high quality thanks to the low aspect ratio. The NIR working range of silicon makes it an ideal choice for various neutral atom species that are popular

candidates in quantum computing, sensing, metrology and simulation, such as alkali metals like rubidium (780 nm and 795 nm) (Steck, Rubidium 87 D line data, 2001), cesium (852 nm and 894 nm) (Steck, Cesium D line data, 2003), potassium (767 nm and 770 nm) (Tiecke, 2010), lithium (671 nm) (Gehm, 2003) and alkali-earth like metals such as strontium (689 nm) (Sorrentino, Ferrari, Poli, Drullinger, & Tino, 2006) and ytterbium (680 nm) (Antypas, et al., 2019). Aside from neutral atoms, the characteristic wavelength of many other popular quantum systems such as nitrogen vacancy (NV) center in diamonds also fall into this spectrum range.

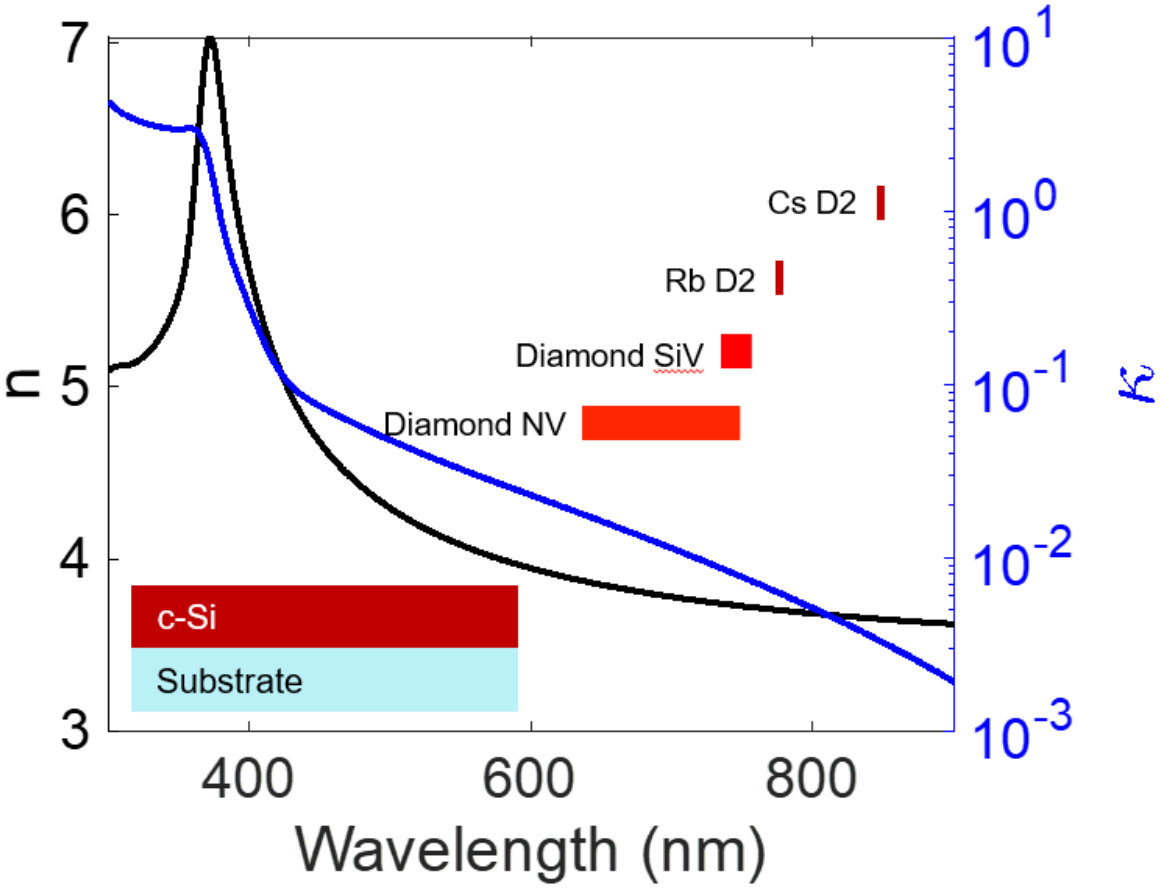

Figure 2-3 Refraction index (n) and absorption coefficient (κ) of crystalline-silicon across part of the visible and NIR spectrum that covers the characteristic wavelength of many quantum systems. The high n and low κ makes c-si a strong candidate material for metasurface.

Silicon-on-sapphire is an attractive material platform for fabricating transmissive metasurfaces operating in the near-infrared to infrared wavelengths. Besides the advantages listed above for (single-crystalline) silicon, sapphire serves as an excellent substrate for our metasurface devices. The wide bandgap (~10 eV) of sapphire ensures its transparency across a broad spectrum of light,

including the NIR region, while the high index contrast with respect to silicon on top strengthens optical confinement in meta-atoms and leads to better optical mode control in the metasurface device. Besides the superior optical properties, sapphire also exhibits excellent mechanical and thermal stability, making it suitable for deploying in harsh challenging situations such as high power (optical dipole trap, multi-photon transition) and high temperature (spin-exchange relaxation free magnetometry, vacuum bakeout) applications (Imthurn, 2007). Finally, SOS is a mature material platform fully compatible with CMOS technology, allowing full integration with silicon-based electronics and photonics (such as photonic integrated circuits) devices (Andreou, et al., 2001).

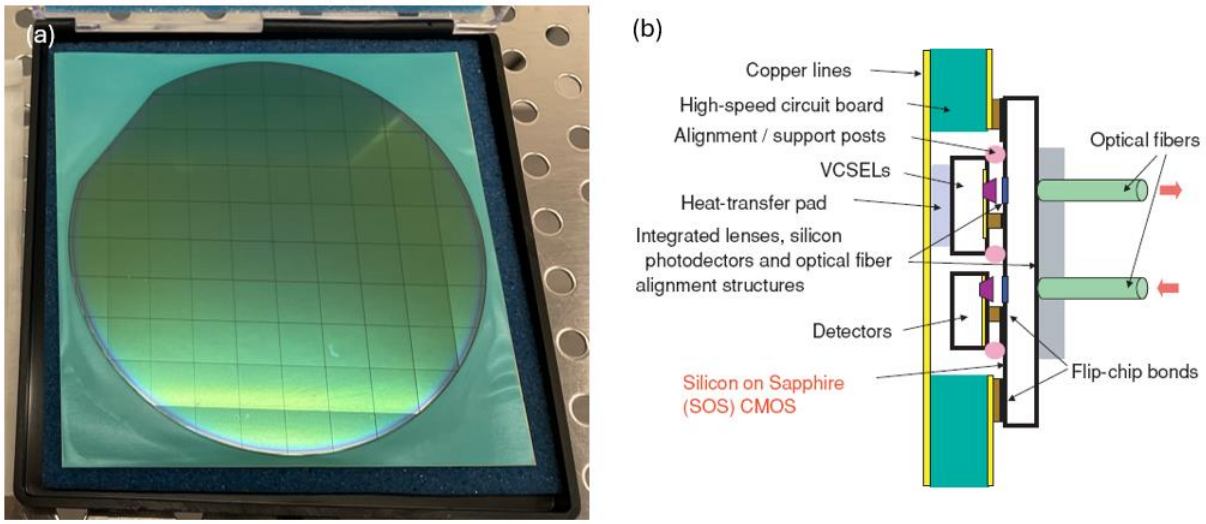

Figure 2-4 (a)The silicon-on-sapphire (SOS) wafer used in this work; (b) Example of an optoelectronic module combing a SOS CMOS die with chip scale active and passive optical components, showing the compatibility of SOS with CMOS technology. *Adopted from* (Andreou, et al., 2001).

In this chapter, we describe our research in the design, simulation, fabrication and characterization of silicon-on-sapphire (SOS) metasurface optics tailored for quantum sensing and quantum computing in neutral atom systems, which are reported in (Yang, et al., 2024) (Fang, et al., 2024). We will summarize two metasurface design algorithms – one based on a direct calculation of the phase profile and one using gradient descent optimization method (Xiao, et al., 2021) to improve the metasurfaces' figure of merit (FOM) for specific applications. Using the first method, we have designed metasurface polarizing optics for rubidium atomic magnetometry operating at the D1 transition (795 nm). These include quarter and half waveplates, a polarizing beam splitter (PBS) and a multifunctional device combining polarization splitting with light focusing. We then developed and improved the recipe for fabrication of SOS metasurface with

electron-beam lithography and reactive ion etching, and successfully fabricated millimeter-scale metasurface PBS. A homebuilt optical characterization setup measures the optical response of the fabricated metasurface and confirms its polarization splitting functionality. We describe a similar development for a SOS metasurface bottle-beam trap generator, which was designed with optimization method and fabricated by our collaborators in the Kats group, and optically characterized with a homebuilt microscope setup to measure the generated dark optical trap profile. Finally, we discuss the potential causes of deviation of optical performances of the metasurface devices and propose several methods for improvement in the future.

For this work, we would like to acknowledge Prof. Mikhail Kats and his lab group, in particular Chengyu Fang, Minjeong Kim, and Hongyan Mei, for their collaboration on developing the SOS fabrication procedures and for leading the bottle-beam trap generator development. We thank Chengyu Fang for providing a numerical tool based on angular spectrum method (ASM) to simulate the far-field response of large-area metasurfaces. Finally, we are grateful to Dr. Alan Dibos and Dr. David Czaplewski from Argonne National Laboratory for their invaluable support and help on fabricating the components described in this chapter.

2.2 Metasurface design methods

In this section, we review two methods used for designing metasurface optics for neutral atom quantum systems. The first method applies to situations where the field profile of the output light $\boldsymbol{E_d}(\boldsymbol{r})$ is known in prior (on the desired image plane) while the second method is more suitable for cases where only a figure of merit (FOM) for the field distribution such as beam directionality, intensity contrast or diffraction efficiency is provided based on the functionality of the metasurface device.

The first method is based on back propagating the expected output field $\boldsymbol{E_d}(\boldsymbol{r})$ back to the transmission plane right after the metasurface. Since the incident field $\boldsymbol{E_i}(\boldsymbol{r}, 0^-)$ is known, and under the assumption that only the zero order diffraction is concerned and no interference exists between the constructing components of the metasurface which is justified in (Arbabi, Horie, Bagheri, & Faraon, 2015), we simply need to solve the transmission coefficient profile $t(\boldsymbol{r})$ through the equation:

$$\boldsymbol{E_t}(\boldsymbol{r}, 0^-) = t(\boldsymbol{r})\boldsymbol{E_i}(\boldsymbol{r}, 0^-) \tag{2.1}$$

The solution is given in (Arbabi, Horie, Bagheri, & Faraon, 2015):

$$t(\boldsymbol{r}) = \frac{\left(\boldsymbol{H_d} \cdot (\boldsymbol{E_i} \times \boldsymbol{z})\right)^*}{|\boldsymbol{H_d} \cdot (\boldsymbol{E_i} \times \boldsymbol{z})|} \tag{2.2}$$

where

$$H_d(\boldsymbol{r}) = \frac{1}{4\pi}\nabla \times \iint_{\vec{\boldsymbol{r}'}\in P_d} d\boldsymbol{r}' E_d^*(\boldsymbol{r}')\frac{e^{ik|\boldsymbol{r}-\boldsymbol{r}'|}}{|\boldsymbol{r}-\boldsymbol{r}'|} \tag{2.3}$$

Therefore, ideally the metasurface should be a phase mask with $|t| = 1$. Notice that the equations here only apply to eigen polarization states of the metasurface, i.e. the polarization does not change after transmitting through the metasurface.

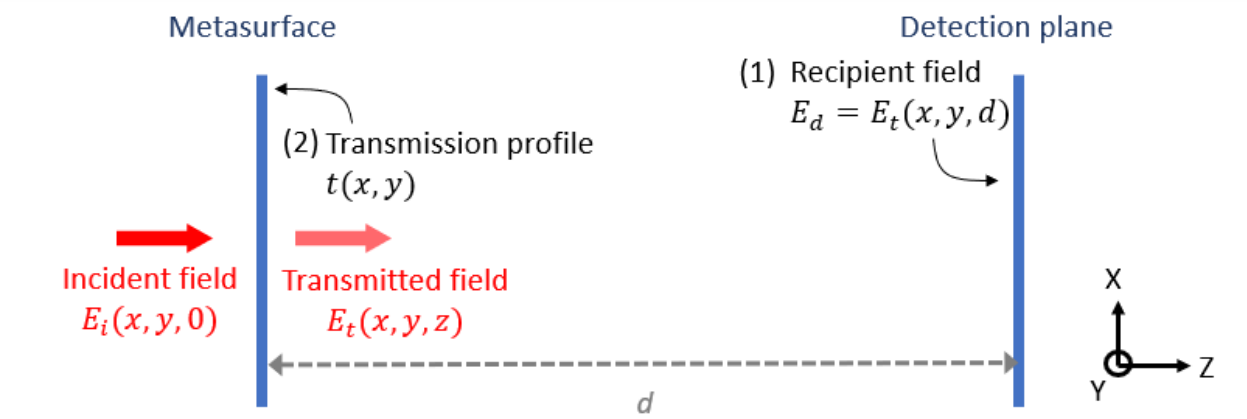

Figure 2-5 Direct calculation of the optimal transmission profile $t(x, y)$.

The second method to obtain the transmission profile is based on pointwise gradient ascent (descent) optimization (Xiao, et al., 2021). Here we assume the phase profile is discretized: $t(r) \rightarrow t_i = t(r_i)$, with being an ensemble of points (usually a lattice) that samples the transmission profile in continuum. First, an initial guess $t_0(r)$ is obtained usually based on physical intuition, or using back propagation detailed in the first method. Next, the incident field $\boldsymbol{E_i}(\boldsymbol{r})$ is multiplied by the phase profile $t_0(r)$ to form the transmitted field, and the initial FOM is calculated based on the field propagation. We then perturb the transmission profile $t(\boldsymbol{r})$ with respect to each optimization parameters (which would be the phase and amplitude of t for every point on the metasurface) and calculate the change of FOM, forming the gradient $\frac{\partial FOM}{\partial t}$ and the improved phase profile: $t'(r) = t(r_i) = t + \frac{\partial FOM}{\partial t}\Delta t$ (we assume the goal is to maximize FOM). Here Δt is the step size. If applicable, the incident beam profile (such as the beam waist of a gaussian beam) could also be an optimization parameter. To avoid getting stuck in local minimum, after the optimization is finished, we can add random perturbations to the transmission profile again and repeat the optimization process.

Once the transmission profile is obtained, a meta-atom with the transmission response closet to t_i will be placed on point r_i, forming the metasurface. For polarization-dependent optics such

as linear polarizers and polarization beam splitters, the meta-atoms will need to match different transmission profiles for different incident polarization states. To achieve the ideal transmission condition, it is essential to not only match the response of the meta-atom with the designed phase but also to force the transmission of the meta-atom to be maximized.

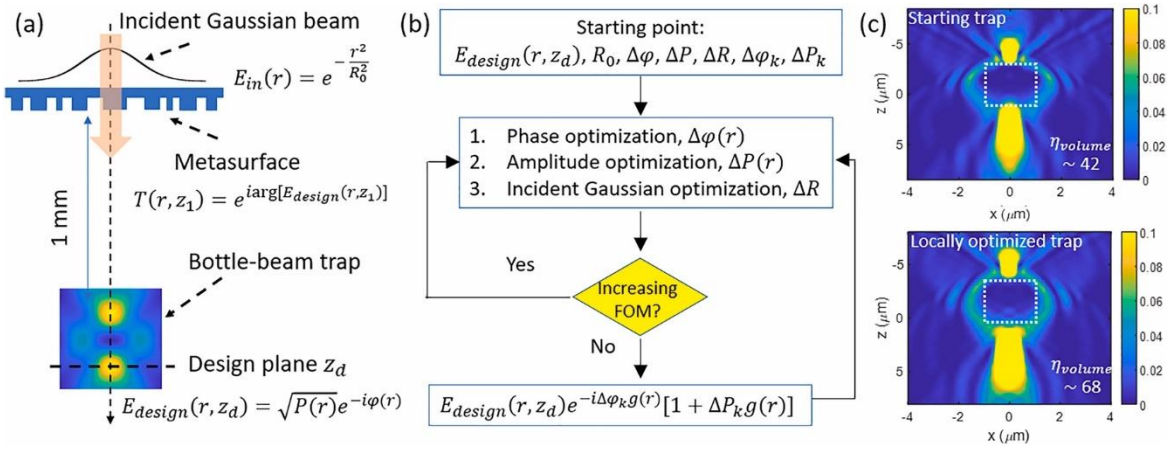

Figure 2-6 Designing a bottle beam trap metasurface with a point-by-point gradient ascent method. (a): Schematic of the gradient-ascent optimization setup; (b) Strategy of updating the phase profile of the netasurface based on improving FOM; (c) Result of the optimization showing an increase in the trap volume of the metasurface bottle beam trap. This figure is reproduced from (Xiao, et al., 2021).

2.3 A silicon-on-sapphire (SOS) metasurface polarizing beamsplitter

In this section, we design a metasurface polarizing beam splitter tailored for the polarimetry measurement in rubidium magnetometers. Part of this section is adopted from my work (Yang, et al., 2024). For implementing a beam splitting based on input polarization of a normally incident plane wave, the phase profile of the metasurface reduces to simple analytical form $t_{xpol} = e^{-ikxsin\theta}$ for an x-polarized beam and $t_{ypol} = e^{ikxsin\theta}$ for a y-polarized beam, where the wavenumber is $k = \frac{2\pi}{\lambda}$ and 2θ is the separation angle between the split beams. For this design, the phase shifts are invariant along y. We select $2\theta = 2\arcsin(\frac{2\pi}{9k}) \approx 25.5°$ to be the split angle which ensures the metasurface to be periodic along x, with a unit cell comprising 9 meta-atoms that is repeated along x, thus greatly reduces the design complexity and results in a simplified E-beam writing procedure.

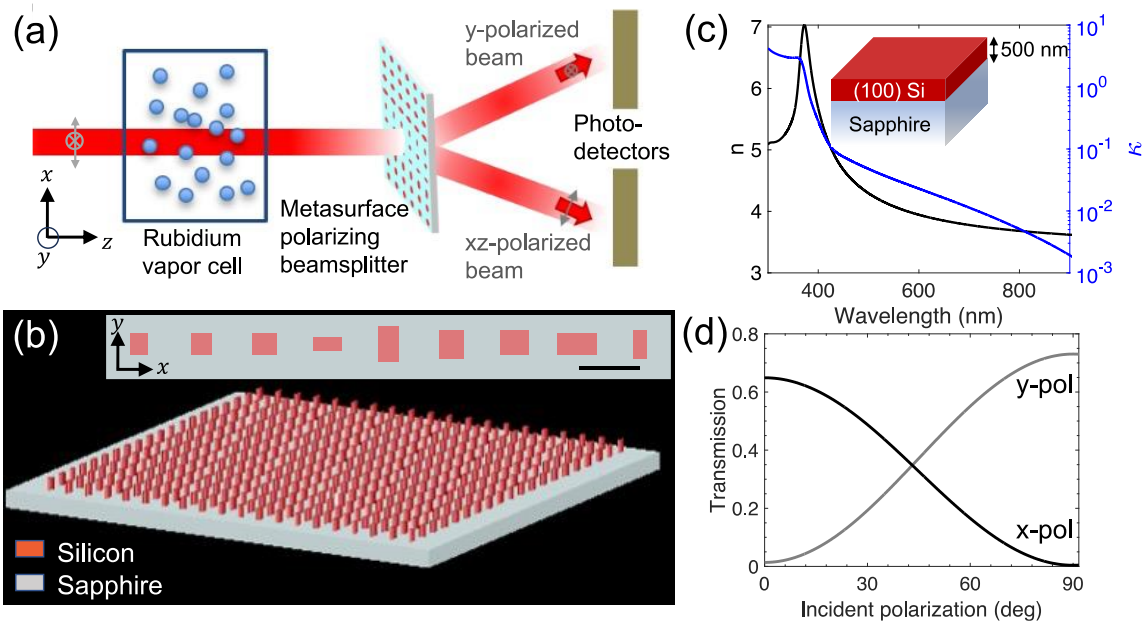

Figure 2-7 (a) Optical polarimetry measurement of atomic spins using a transmissive metasurface polarizing beamsplitter (PBS) based on a (b) silicon-on-sapphire (SOS) platform consisting of rectangular meta-atoms in single-crystal silicon on a transparent sapphire substrate. Inset shows the unit cell of the PBS design, which comprises of 9 meta-atoms. The scalebar is 400 nm. (c) Complex refractive index (n and κ) of silicon extracted using spectroscopic ellipsometry. The thickness of silicon layer is ~500 nm. Details on the ellipsometry are provided in the Supplementary Information A.5. (d) Simulated transmission into the first-order diffracted modes for the metasurface design (Yang, et al., 2024).

The metasurface, characterized by its phase profile, will be discretized and implemented by an array of rectangular posts, defined by the lattice constant a and individual post parameters (length along x and y axis). The lattice constant should be no larger than the operating wavelength in order to satisfy the zero-order diffraction approximation adopted in calculation. We have chosen 400nm for our operating wavelength of 795nm. The rectangular nature of the scattering element forms birefringence and independent phase shifts for two orthogonal linear polarizations. In parallel to determining the requisite phase profiles, the transmission and phase shifting properties of a wide range of silicon post parameters (axis length ranging from $0.2a$ to $1.4a$, where $a = 400nm$ is the lattice constant) are determined by full-wave simulations for each incident polarization (Figure 2.8). This forms a database that maps each post parameter to a polarization-dependent phase response. We can then select post parameters that best approximate the desired phase response at each metasurface lattice site with an error ε that measures how well the elliptical posts match the predetermined transmission profile t:

$$\varepsilon = \left|t_{x\,pol}^{post} - t_{x\,pol}\right|^2 + \left|t_{y\,pol}^{post} - t_{x\,pol}\right|^2 \tag{2.4}$$

The form of the error ε is chosen to ensure an optimal phase matching and high transmission on both polarizations. We have shown that for our polarizing beam splitter design implemented by a 2500×2500 array of posts, the maximum error is 0.0886 while the average error is 0.0166, a good indication of the successfulness of this method.

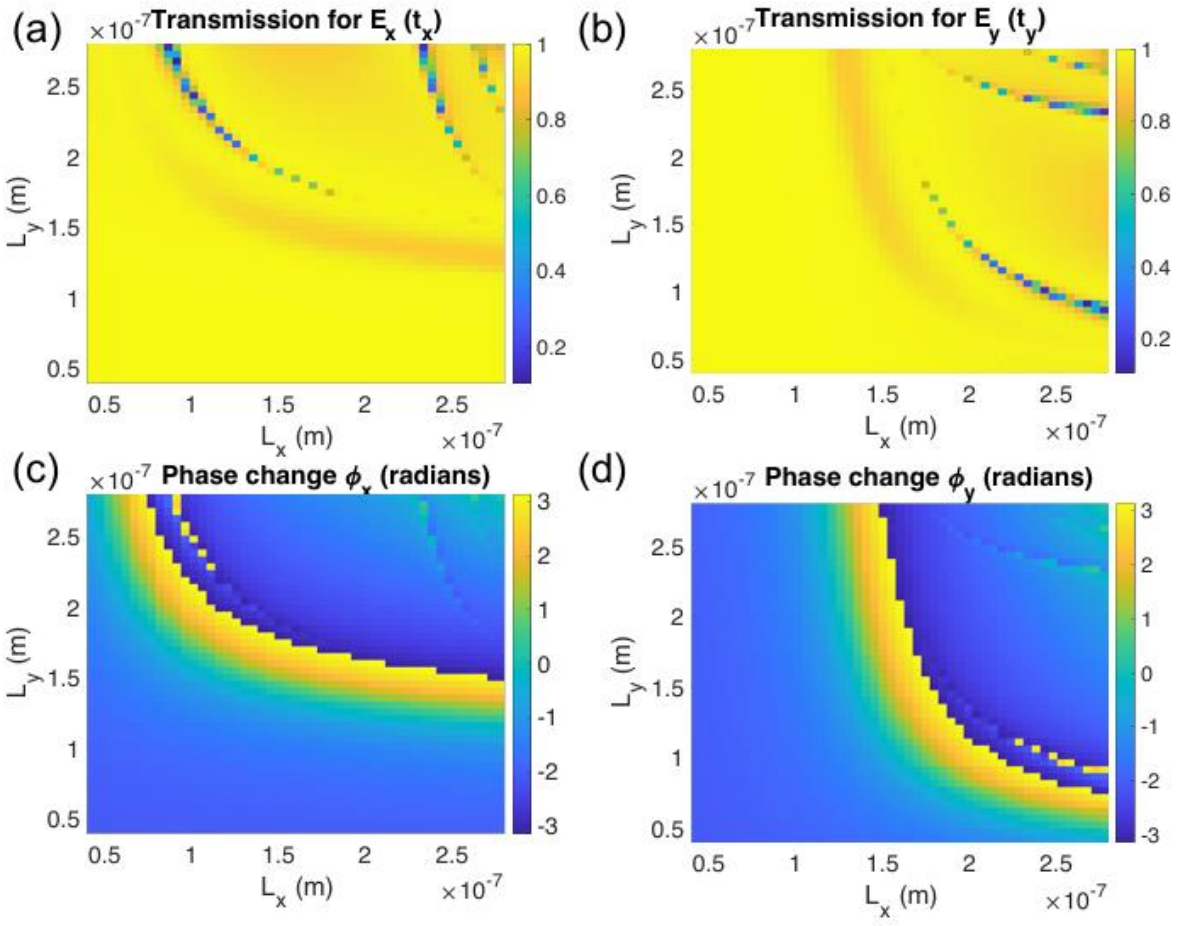

Figure 2-8 Calculated normalized transmission and phase shift of an incident x- or y- polarized plane wave, based on full-wave simulation of a square silicon array of rectangular rods with fixed lattice constant (a = 400 nm), post height (h = 500 nm), and swept transverse dimensions L_x and L_y.

It should be noted that while the calculation of the metasurface profile using formula (2.2) is rigorous as long as the desired output field profile E_d is physical, the intrinsic discretization process associated with metasurface construction as well as the phase matching using individual rectangular posts inevitably introduces imperfection and are the ultimate limiting factors in the performance of the metasurface device. Moreover, the matching error given by equation (2.4) does

not strictly correlate to the ultimate performance of the metasurface device (for example, the polarization extinction ratio of the metasurface PBS), since that is determined by the global behavior of the array of scattering elements, including their coupling with each other. Several optimization techniques for metasurface design have been invented to tackle this issue, including adjoint optimization and statistical-based efficient global optimization (EGO) method (Lalau-Keraly, Bhargava, Miller, & Yablonovitch, 2013; Mansouree, McClung, Samudrala, & Arbabi, 2021; Wambold, et al., 2020).

To characterize the optical performance of our metasurface beam splitter, we performed finite-difference time domain (FDTD) simulations (Lumerical) for a design with a device area of 16 μm × 16 μm using a Gaussian beam source (see Appendix A2 on justification of our simulated beam source, which shows that the metasurface PBS is compatible with any paraxial beam with a near-uniform phase profile at the plane of incidence). Although our design can be extended to a much larger (>1 mm^2) device footprint, this representative simulation area is chosen to limit computational time.

The setup for the simulation is as follows (Figure 2.9a): The incident beam of wavelength $\lambda = 795\ nm$ is propagating in the z-direction at normal incidence. Two frequency-domain field monitors are located at the back and front side of the metasurface device to measure the near field transmission and reflection field profile and total transmission/reflection. The polarization splitting behavior of the metasurface PBS, characeterized by the normalized transmitted light intensity into the designed direction specified by the split angle, is obtained through the built-in far field projection script in Lumerical.

We simulated the transmission characteristics of the metasurface for different input polarization angles. Figure 2.9b represents the normalized transmitted far-field intensity for an incident linear polarization at 45° (comprising of an equal superposition of x and y polarizations). As expected, the designed metasurface splits the 45° linearly polarized incident beam into x- and y-polarized beams propagated along different directions. The split beams have a slightly different transmittance with a split ratio of 40% and 35% for x and y polarization respectively. The transmittance among various input polarization angles is shown in Figure 2.7d. As shown in Figure 2.7d, our metasurface PBS design exhibits polarization dependent beam-splitting, with the polarization extinction ratio (PER, defined as the ratio of the transmitted powers into the split beams for each incident x or y polarization component) calculated to be 16.7 dB (for x-polarized input) and 22.6 dB (for y-polarized input). The total transmission efficiency of the simulated structure is over 70%, with roughly 20% of the incident light reflected and 6-7% absorbed by the structure (see appendix A6).

The transmission and PER discrepancies between the two orthogonal linear polarizations are still under investigation. As noted in section 2.2, the response of metasurface is determined by the collective behavior of meta-atoms and cannot simply be attributed to the local matching errors (formula 2.4). However, we suspect the better performance (higher transmission, lower

polarization crosstalk) for the y polarization is likely due to the metasurface elements being invariant along y.

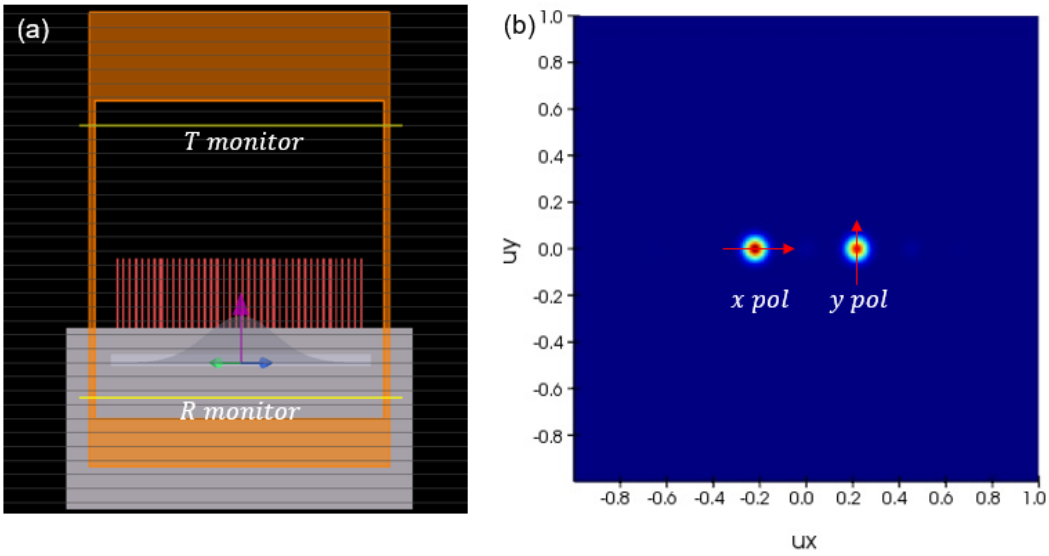

Figure 2-9 (a) FDTD Simulation setup. The orange box indicates the simulation region. (b) Far field projection of the metasurface PBS at 45 deg incident polarization demonstrating polarization splitting behavior.

2.4 Fabrication and characterization of metasurface polarizing beamsplitter

Our fabrication procedure is illustrated in Figure 2.10a. The metasurface PBS was fabricated on an SOS wafer with the silicon thickness $h = 500$ nm and resistivity > 100 Ω·cm. A 50-nm silicon dioxide (SiO_2) hard mask was first deposited on the silicon using plasma-enhanced chemical vapor deposition (PECVD), followed by spin-coating of a positive electron-beam resist (ZEP 520A). The metasurface pattern was written using electron-beam lithography at a beam current of 4 nA and patterned hard mask was subsequently formed by etching of the SiO_2 layer in a mixture of CHF_3 and O_2 gases. Finally, a mixture of HBr and O_2 gases was used to etch the silicon metasurface structure using inductively coupled plasma reactive ion etching (ICP-RIE). While the hard etch mask can be removed with a buffered oxide etch, based on simulations the remaining SiO_2 mask does not meaningfully affect the metasurface performance (Appendix A7).

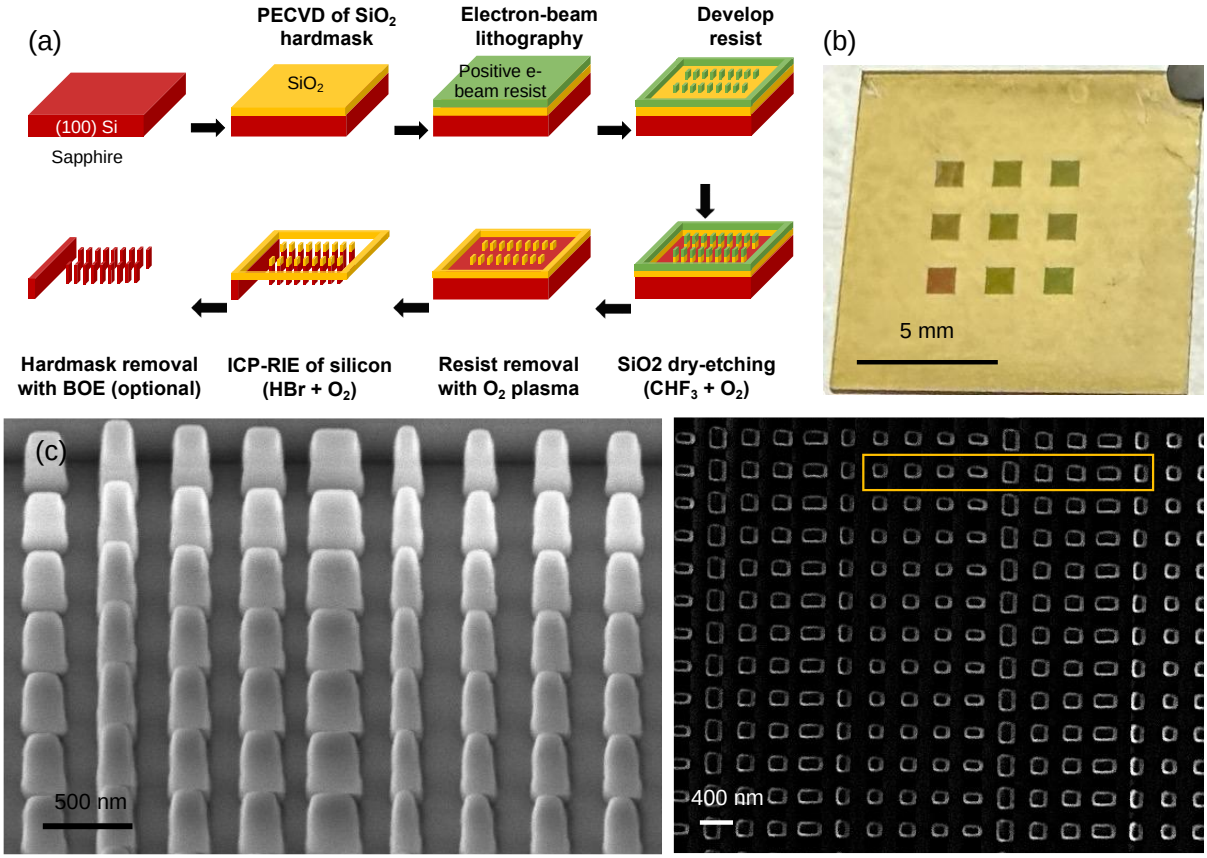

Figure 2-10 (a) Schematic of the fabrication process. BOE: buffered oxide etch. (b) Photo of arrays of metasurface PBS (each 1 mm by 1 mm) fabricated on an SOS sample. (c) Side profile (taken at 30 degrees) and top-down SEM images of the etched silicon posts. For the metasurface array shown, a unit cell is highlighted.

The SOS chip after fabrication can be seen in Figure 2.10b, with each 1 mm^2 array of etched silicon metasurfaces consisting of a different dose within the 3 × 3 array. Figure 2.10c show the scanning electron microscopy (SEM) images of the metasurface PBS. For the fabricated samples in this work, the silicon layer is estimated to be under-etched by ~10 nm and the sidewall profile for each meta-atom is slightly tapered with the angle estimated to be $7° \pm 2°$. Both these effects can be attributed to drifts in the silicon etch anisotropy and etch rate due to charging in the silicon and sapphire, which might be mitigated with the use of doped silicon in the future.

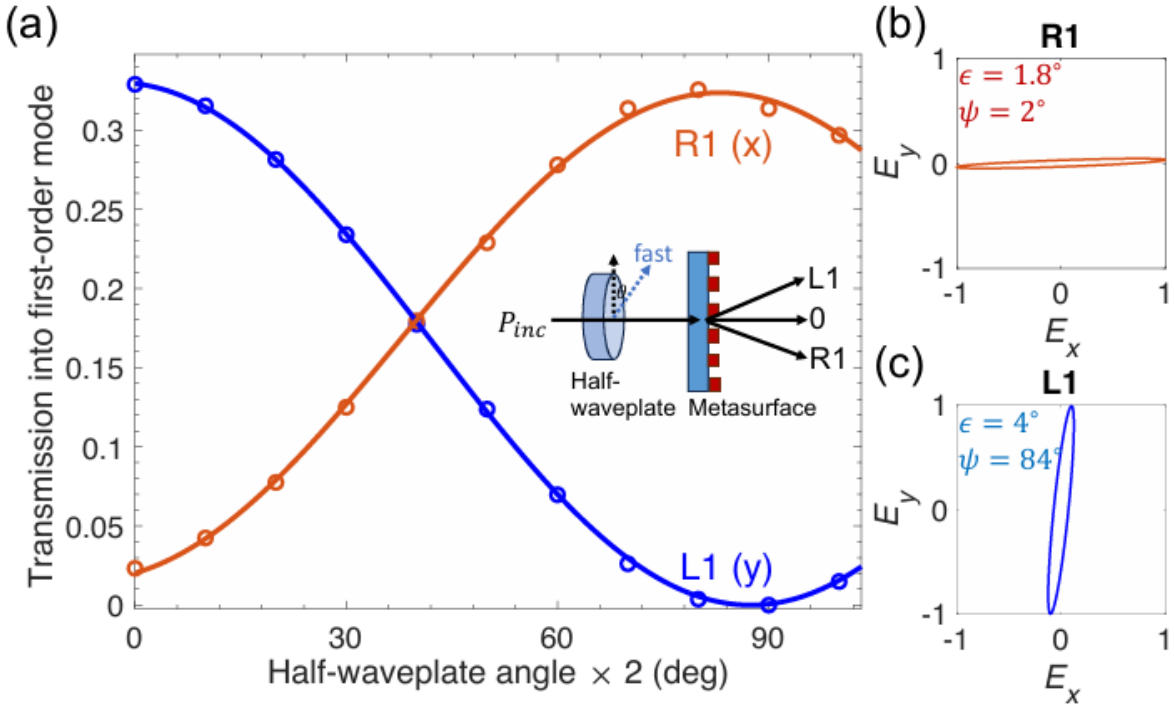

Figure 2-11 (a) Measured transmission (transmitted power divided by incident power Pinc) into each of the polarization-dependent modes as a function of incident polarization. The inset shows the labeling of the zeroth order ("0") and diffracted modes in the transmitted beam. (b,c) Polarization ellipses for the first-order diffracted modes, along with the ellipticity (ϵ) and azimuth (ψ) values, taken at an incident polarization that yielded balanced outputs at R1 and R1.

The optical performance of the metasurface was measured with a home-built characterization setup. The laser source is a 795nm distributed Bragg reflector (DBR) laser (Photodigm) powered by a precision laser diode controller (Vescent D2-105). The laser is coupled into a polarization maintaining fiber and launched in free space using a fiber collimator (Thorlabs). In order to characterize the metasurface PBS performance under different polarization angles, the collimated beam first goes through a linear polarizer (Thorlabs LPNIR050) to ensure a pure linear polarization. A quarter waveplate with its fast axis aligned 45° to the linear polarizer axis converts the light into circular polarization. Finally, a second linear polarizer sets the required polarization angle. The reason to use this more convoluted setup instead of the conventional linear polarizer and half waveplate is that the half waveplate usually introduces a little bit of ellipticity when rotating the polarization angle. The metasurface sample was mounted on a tip-tilt stage which allows for adjustment of laser incidence angle to obtain the optimal polarization splitting performance. We observed polarization-dependent splitting, shown in Figure 2.11a, of the transmitted beam into the first-order diffracted beams, which are labeled R1 (for the x-polarized incident beam) and L1 (for the y-polarized incident beam). The maximum transmission into each port (normalized to the incident power) is 33%. The PER is determined to be PER =460 (26.6 dB) and PER =16 (12 dB). The output polarization into each first-order mode was measured on a polarimeter observed to

largely correspond to the respective incident electric field components (Figure 2.11b and 2.11c). The slight ellipticity introduced in the transmitted beams and difference in PER between the two ports can be attributed to fabrication imperfection that leads to cross-polarization contamination of the output scattering orders.

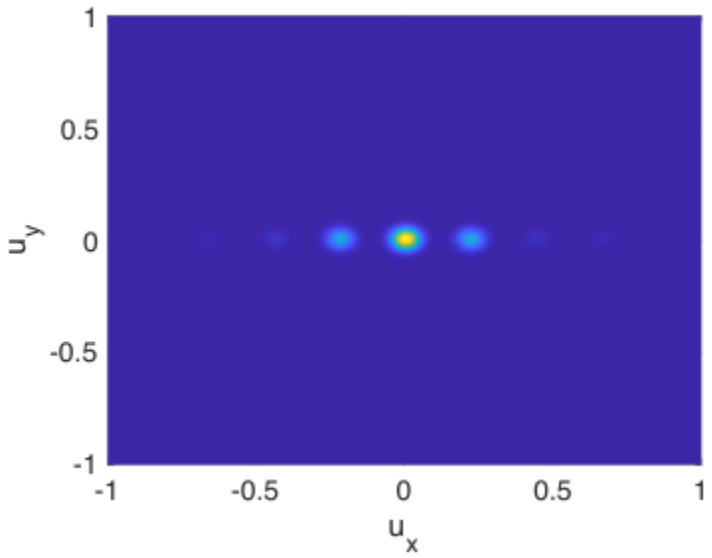

Figure 2-12 Simulated far-field profile of the metasurface design with a 5° taper in the sidewall angle.

The overall transmission through the structure is 62.5%, with significant reflection (not quantified) observed in agreement with simulations (appendix A6). This reflection may be reduced by incorporating anti-reflection (AR) coating in the future. Common anti-reflection coatings are fabricated using silicon dioxide (Nagel, Aberle, & Hezel, 1999; Prasad, Balakrishnan, Jain, & Jain, 1982). For a substrate with refractive index n_s, the index of refraction for the AR coating should be around $\sqrt{n_s}$. For our SOS platform, SiO2 and MgF2 are potential candidates for single-layer AR coating materials (see appendix A8) (Bruns, Vergöhl, Zickenrott, & Bräuer, 2016; Stern & Cole, 2008; Wang, Lv, Qi, Liu, & Long, 2022). In addition to the first-order modes, the transmitted light was distributed into zeroth-order mode (accounting for 11.8% of the signal) and additional higher-order modes amounting to a few percent of the total incident power (table 2.1). The occurrence of the zeroth-order and higher-order modes can be attributed to the tapered profile of the silicon meta-atoms, based on simulations (Figure 2.12). Whereas the designed geometry suppresses transmission into the zeroth- and higher-order modes so that over 95% of the transmitted light goes into the first-order modes, any deviation from a straight sidewall causes the incident power to be distributed into these undesired channels.

Table 2-1 Transmitted power into the zeroth, first, and second order modes, for an incident beam polarization that best balanced the outputs into R1 and L1.

Transmitted beam	Fraction transmitted (relative to P_{inc})
R1 (first-order)	13.66%
L1 (first-order)	13.50%
0 (zeroth-order)	11.83%
R2 (second-order)	1.92%
L2 (second-order)	3.17%

2.4 Metasurface waveplates

Waveplates uses birefringent materials to impose controlled phase shift between different electromagnetic field components – usually polarization states. They are often used when precise polarization control is required, such as converting linear polarization to circular polarization and rotating polarization axis. In quantum technologies based on neutral atoms such as atomic magnetometry and atom computing, waveplates are indispensable optical components, finding their applications in atom trapping and cooling, state preparation, quantum gate operations and state readout. Compared to conventional waveplates made from layers of birefringent materials like quartz, metasurface waveplates are thinner and more compact, making them ideal for integrating with other chip-scale photonic devices in miniaturized optical systems. Moreover, by controlling the geometry and arrangement of the meta-atoms, metasurface waveplates can impose customizable optical response to the incident field, such as achromatic phase retardation and spatial polarization control, and generating complex polarization states such as vector beams. With modern lithography technologies, mass production of large area metasurface waveplates should be a possibility, compared to conventional waveplates that often require precise and extensive cutting and polishing of birefringent materials.

Metasurface waveplate is one of the simplest metasurface optics to design, as it needs only one type of meta-atom to impose the desired linear birefringent response. Similar to the matching error criterion we used in designing the metasurface PBS, we use

$$\varepsilon = \left| \frac{t_{y\ pol}^{post}}{t_{x\ pol}^{post}} - e^{i\frac{2\pi}{m}} \right|^2 + \left| |t_{x\ pol}^{post}| - 1 \right|^2 + \left| |t_{y\ pol}^{post}| - 1 \right|^2 \tag{2.5}$$

when selecting the meta-atom geometry for $\frac{\lambda}{m}$ waveplate operating at 795 nm. The first term in the expression ensures the correct phase retardation while the second and third maximizes the metasurface transmission. Figure 2.13 shows our design for quarter and half waveplate, with a relative phase shift 90.22°/178.86° of and both exhibit high transmission amplitude for x and y polarization: $t_x = 0.9987/0.9981$, $t_y = 0.9838/0.9762$.

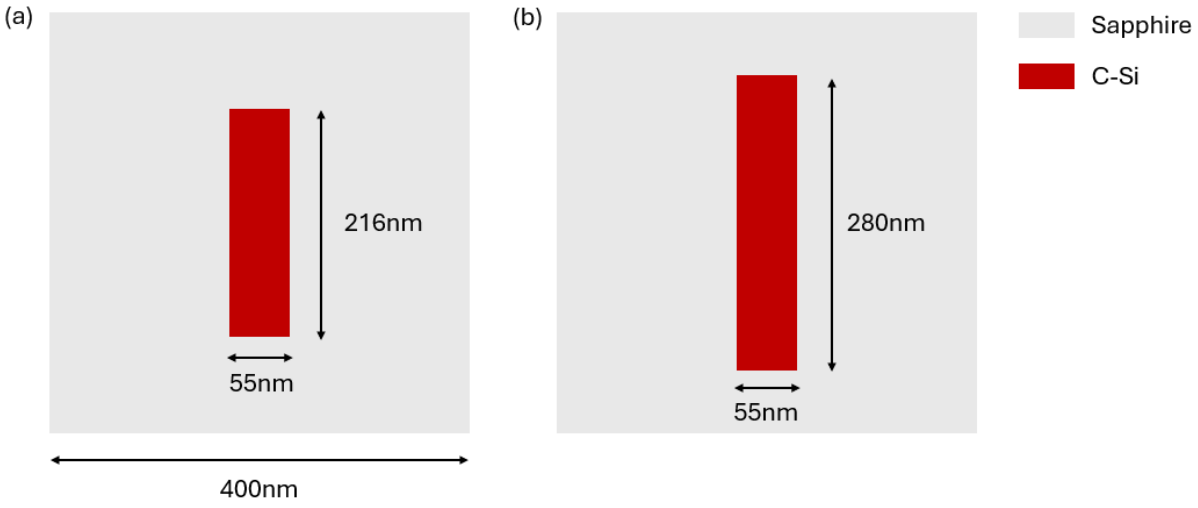

Figure 2-13 Unit cell of the metasurface for: (a) quarter waveplate; (b) half waveplate.

To simulate the actual performance of the metasurface waveplate, we use the polarization ellipse analysis tool from Lumerical, which is capable of outputting polarization angle and degree of circular polarization for all the diffracting orders and wavelengths using a single full wave simulation from the near field data. For metasurface optics, we ignore the higher order diffraction and focus on the transmitted order (0,0). To speed up the simulation and manage the memory resources, we use periodic boundary condition and a plane wave incidence. For both waveplate designs, the incident polarization is 45° linear with respect to metasurface x axis. An ideal quarter waveplate should convert it to circular polarization while a half waveplate would rotate it to $-45°$. Figure 2.14 shows the polarization ellipse for the transmitted light after quarter/half waveplate. Notice that the degree of circular polarization is determined by the ratio between the major and minor axis length of the polarization ellipse and the angle of the polarization is given by the angle between the major axis and x direction. For the quarter waveplate, the polarization of the transmitted light has an axis ratio of 1.09, while for half waveplate the ratio is 18.97 and the polarization angle is $-44.34°$. This simulated performance deviates from the expected value (QWP: ratio: 1.0156 HWP: ratio: 100.56 angle: $-44.36°$) based on the transmission coefficient of the individual meta-atoms composing the waveplates. Such inconsistencies likely emerge from the fact that different analysis methods are adopted when calculating the transmission coefficient of the meta-atoms and when calculating the output polarization of the transmitted light. For example, the transmission coefficients are obtained through scattering matrix parameter extraction where analysis is done in eigenmode (x/y polarization) and thus any orthogonal polarization in the output field are rejected.

Table 2-2 Theoretical vs. simulated performance of metasuface waveplates. The polarization angle and polarization ellipse axis ratio are from the output polarization state when the metasurface is incident with a 45° linearly polarized light.

Waveplate	Theoretical/simulated relative phase shift	Theoretical/simulated polarization angle	Theoretical/simulated r_{maj}/r_{min} of the ellipse
quarter	90.23°/94.28°	$NA/-29.33°$	1.0156/1.09
half	178.86°/173.96°	$-44.34°/-44.36°$	100.56/18.97

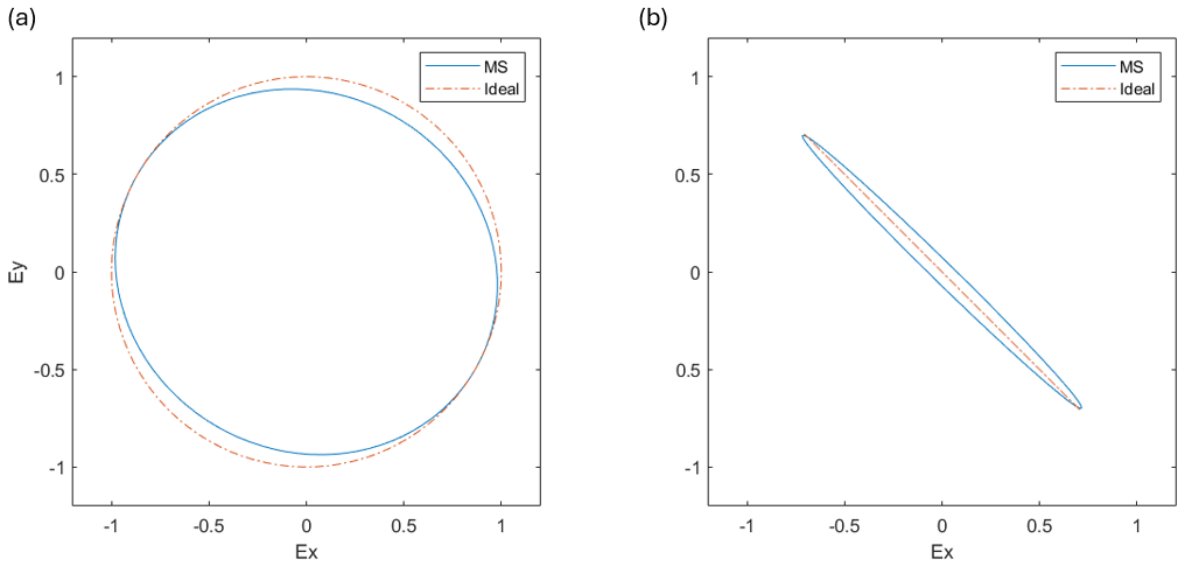

Figure 2-14 Ideal (red dash-dotted) and simulated (blue) far field polarization ellipse of the transmitted light with a 45° linearly polarized incidence for: (a) metasurface quarter waveplate; (b) metasurface half waveplate.

2.5 A metalens with polarization-dependent deflection

The true potential of metasurface optics lies in their capabilities of replacing multiple bulk optics with a single planar device thanks to their fully customizable optical response (Chen, Liu, Li, Cheng, & Tian, 2020; An, et al., 2021; Shirmanesh, Sokhoyan, Wu, & Atwater, 2020; Huang, et al., 2017; Liu, et al., 2021). Here, we demonstrate this powerful aspect by designing and simulating a multifunctional metasurface that is capable of simultaneously achieving polarization splitting as well as focusing the incident light. Such a device could potentially benefit the light collection efficiency during the balanced polarimetry and help further compactify the atomic magnetometry setup.

The phase profile for a metasurface that acts as a focusing lens for a normal incident beam with focal length f is (Khorasaninejad & Capasso, Metalenses: Versatile multifunctional photonic components, 2017):

$$\phi(x,y) = \frac{2\pi}{\lambda}\left(f - \sqrt{f^2 + x^2 + y^2}\right) \tag{2.6}$$

Here, λ is the wavelength of the incident light, (x, y) is the coordinate on the metasurface plane. Such phase profile ensures all rays arrive in phase at the focal point. To create a PBS with light focusing capability, we can impose different metalens phase profile for the two orthogonal linear polarizations with spatially separated focal points.

The phase profile for our PBS + lens design is:

$$\phi_x(x,y) = \frac{2\pi}{\lambda}\left(f - \sqrt{f^2 + (x + x_0)^2 + y^2}\right) \tag{2.7}$$

$$\phi_y(x,y) = \frac{2\pi}{\lambda}\left(f - \sqrt{f^2 + (x - x_0)^2 + y^2}\right) \tag{2.8}$$

which focuses the x polarized light into a diffraction limited spot at $(-x_0, 0)$ on the focal plane and $(x_0, 0)$ for the y polarized light.

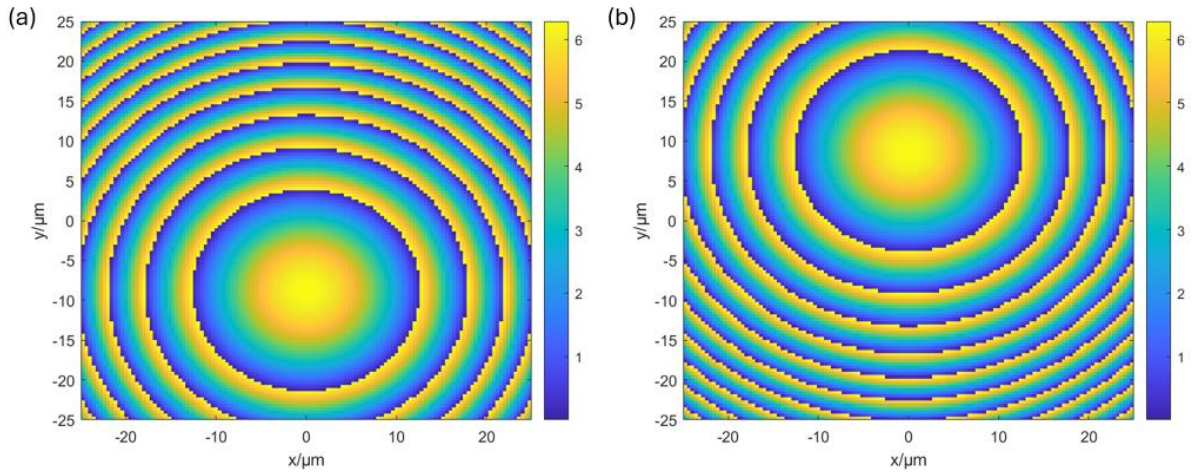

Figure 2-15 Phase profile of the designed multifunctional metasurface with focal length $f = 100\ \mu m$ and 10° polarization split angle for: (a) x polarization incidence; (b) y polarization incidence.

We will now construct the multifunctional metasurface with focal length $f = 100\ \mu m$ and polarization split angle $\frac{\theta}{2} = 5^{\circ}$ (corresponding to $x_0 = f tan\frac{\theta}{2} = 8.749\ \mu m$). First, notice that the phase profile oscillates rapidly as we move away from the metasurface center. Since we are effectively sampling the phase profile using a lattice of meta-atoms with periodicity $a = 400\ nm$, the Nyquist sampling theorem dictates that the radius (or half length) of the metasurface r satisfy:

$$r < \frac{\lambda f}{2a} = 99.375 \mu m \tag{2.9}$$

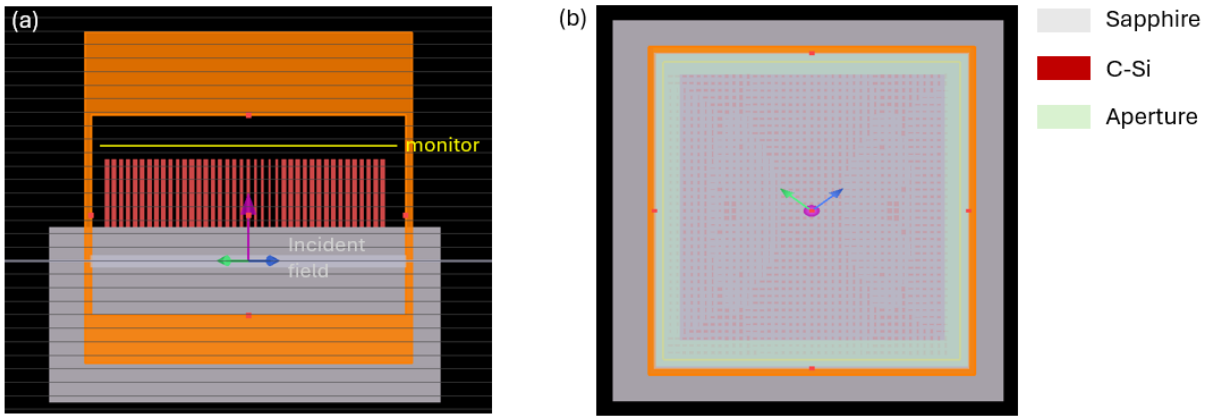

Figure 2-16 Schematics of the full-wave simulation setup. (a) xz plane view of the setup showing the simulation region (orange), near field monitor (yellow) and incident field (arrow); (b) Top view of the simulation setup and metasurface device. The green rectangle aperture ensures the field is confined to the metasurface region.

We follow the same procedure in Chapter 2.2 for constructing the metasuface. Figure 2.15 shows the phase profile for the metasurface with 125×125 meta-atoms. To simulate the optical performance of the metasurface, we adopt two methods. First, for a small version with 40×40 meta-atoms, we perform a full wave simulation in Lumerical. 795 nm plane wave source polarized at 45° impinges on a rectangular aperture before going through the metasurface. The aperture is set to be slightly smaller than the metasurface to avoid unwanted edge effects. Due to computational resource limitation, only a 40×40 array is simulated. A field monitor on top of the metasurface structure collects the near field data from which the far field projection is calculated. Figure 2.17 shows the distribution of the field intensity $|\boldsymbol{E}|^2$ within the xz plane where z is the propagation axis. The metasurface retains the polarization splitting behavior similar to the metasurface PBS in 2.2 while the maximum intensity located at $z \approx 60\ \mu m$ indicates the metalens aspect of the device. The transverse field profile taken at $z \approx 60\ \mu m$ also shows the incident beam being focused down to a few microns. The deviation of the simulated focal length from the $100\ \mu m$

designed value can be contributed to the small device size and the limited number of meta-atoms that map the 2π phase coverage across the metasurface.

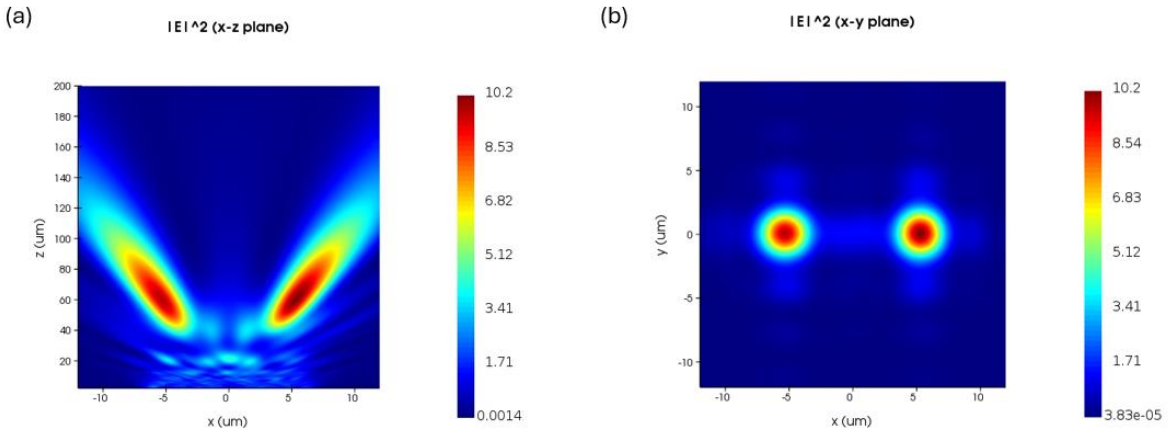

Figure 2-17 Full wave simulation & far field projection of the metasurface PBS with light focusing capability. (a) Field intensity distribution in the xz plane showing the polarization splitting and light focusing around $z = 60\mu m$. (b) Field intensity distribution in the xy plane at $z = 60\mu m$ showing the diffraction-limited spots. The cross pattern surrounding the light spot can be attributed to the artificially capped incident plane wave.

To fully capture the optical response of the metasurface device while keeping the simulation computationally efficient, we resort to the angular spectrum method (ASM). ASM models the propagation of the transmitted light by expanding the near field after metasurface as a summation of plane waves (for simplicity, the field are written in scalar form):

$$E_t(x, y, 0) = E_t^{(0)}(x, y) = \iint \tilde{E}_t(k_x, k_y) e^{i(k_x x + k_y y)} dk_x dk_y \tag{2.10}$$

Here $\tilde{E}_t(k_x, k_y) = \mathcal{F}(E_t^{(0)}(x, y))$ is the 2D Fourier transform of the near field. The far field response of the metasurface is simply obtained by letting each plane wave components propagate along $\hat{z}$:

$$E_d(x, y, z) = \iint \tilde{E}_t(k_x, k_y) e^{i(k_x x + k_y y + k_z z)} dk_x dk_y \tag{2.11}$$

where $k_z = \sqrt{k^2 - k_x^2 - k_y^2}$.

To simplify the computation, we approximate the transmitted field by assuming a piecewise uniform metasurface response within each individual unit cell u_j:

$$E_t(x, y, 0) = t_j E_i(x, y, 0) \; for \; (x, y) \in u_j \tag{2.12}$$

where t_j is the effective transmission coefficient of the meta-atom placed at the center of u_j. Here, we use the same type of incident beam as in the FDTD simulation (plane wave capped by an aperture slightly smaller than the metasurface). The transmitted field E_t is then propagated according to formula (2.11). Figure 2.18 shows the normalized field intensity distribution along the xz plane for incident light with x and y polarizations, clearly indicating the separation of polarizations and a focal plane at $z \approx 100\ \mu m$. The field at the focal plane is also calculated, demonstrating the original incident beam of $d = 50\ \mu m$ has been focused down to a few microns.

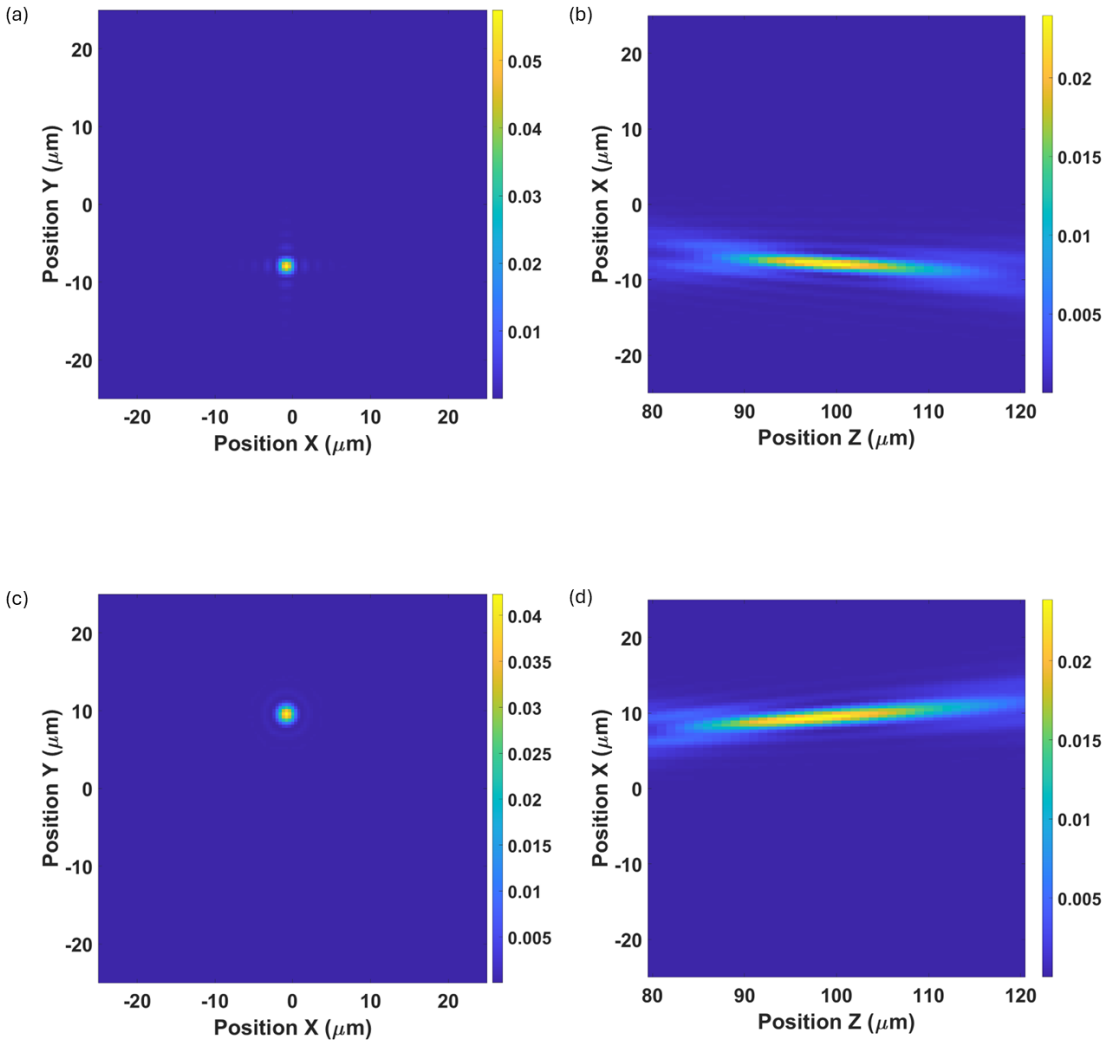

Figure 2-18 Simulation of the metasurface device using ASM method for: (a) xy plane, incident x-polarized light; (b) xz plane, incident x-polarized light; (c) xy plane, incident y-polarized light; (d) xz plane, incident y-polarized light;

As with the case in metasurface PBS, we also conducted a study on the effect of sidewall tapering during fabrication on the optical performance of the light-focusing PBS device. In the same full wave simulation with the 40 × 40 array, we modified the meta-atom to exhibit a 5° tapering and obtained the field distribution in the xz plane (Figure 2.19). It is clear that the geometrical distortion of the nano-atoms significantly alters the metasurface's response and most of the optical power is simply transmitted and focused on a different focal plane. In addition to the

two designed polarization deflection channels, higher order scattering modes are also visible, further decreasing the device's utility. Such behavior is very similar to what we have seen in the metasurface PBS (both simulation and experiment). In the metasurface PBS design, the higher order scattering is attributed to the periodic nature of the device acting as a 1D diffraction grating. Here, the existence of parasitic scattering orders requires further investigation as now the metasurface is aperiodic. Nevertheless, it is evident that the birefringence property of the meta-atom is very sensitive to geometric deviation, which makes the fabrication of metasurface polarizing optics challenging. In addition, any beam-deflecting metasurface will be impacted more severely than non-deflecting metasurface optics (such as beam-shapers), as structure imperfections cause parasitic scattering modes to appear, effectively diminishing the efficiency of the device.

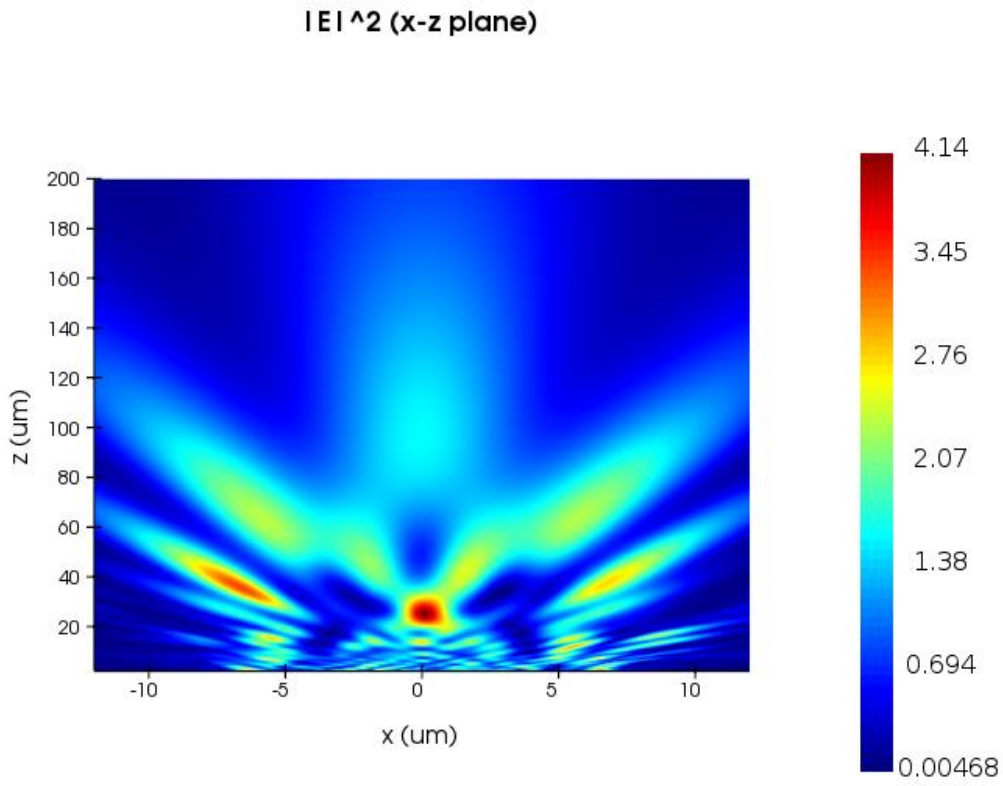

Figure 2-19 Field intensity distribution in the xz plane with a full wave simulation and far field projection of the 40 × 40 tapered meta-atom array.

2.6 A metasurface bottle beam trap generator

Optical bottle beam is characterized by a 3D beam profile that has a local intensity minimum surrounded by regions of higher intensity in all directions (Xiao, et al., 2021). Such beam profile

can serve as a dark trap for atoms when the wavelength is blue detuned from the atomic transition. Such dark trap (and its array) is an attractive candidate for applications in atom-based quantum sensing and quantum computing, since an atom residing in it has smaller photon scattering rate that could interfere desired quantum operations and the trap itself is more robust against laser intensity noise (Graham, et al., 2022). Therefore, efficiently generating high quality bottle beam traps with relatively simple optical setup is of interest in the field of engineering quantum systems.

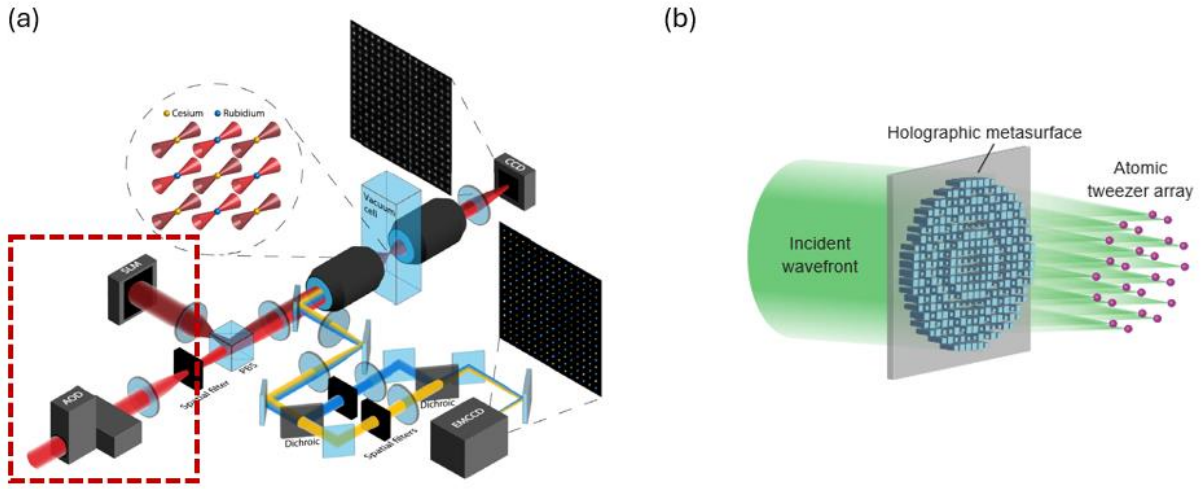

Figure 2-20 (a) Conventional schematic of forming trapped neutral atom arrays, which involves complicated optical setup and expensive active photonic components (red dashed region) including spatial light modulators (SLMs) and acousto-optic deflectors (AODs) (Singh, Anand, Pocklington, Kemp, & Bernien, 2022); (b) Metasurfaces can potentially simplify part of these setups and lead to a more compact trapping system (Holman, et al., 2024).

Due to its planar structure and flexible optical response, metasurface has the potential to achieve chip-scale bottle beam atom traps. In (Xiao, et al., 2021), an efficient metasurface generating a spherically symmetric bottle beam is designed based on gradient descent method. The figure of merit (FOM) η for the bottle beam trap is defined as

$$\eta = \frac{min_{\boldsymbol{u}}\{I_{max}(r, \boldsymbol{u})\} - I_0}{P} \tag{2.13}$$

Here, P is the incident optical power, I_0 is the intensity of the trap center, $I_{max}(r, \boldsymbol{u})$ is the maximum intensity with respect to distance r from the trap center and along fixed direction vector $\boldsymbol{u}$. Therefore, $min_{\boldsymbol{u}}\{I_{max}(r, \boldsymbol{u})\}$ characterizes the 'weakest direction' of the dark trap.

As mentioned in section 2.2, the parameters to optimize are the amplitudes A_j and phases φ_j (at some designated points after discretization) of the electric field $E_d(r,z)$ at some objective plane close to the trap center. $E_d(r,z)$ is then back propagate to the metasurface plane to obtain the field profile $E_d(r,0)$, where the real transmitted field is constructed as $E_t = E_0 e^{-\frac{x^2+y^2}{R^2}} e^{iarg(E_d(r,0))}$. Fresnel diffraction formula is then applied to E_t to get the 3D optical trap profile, where the change in FOM is calculated and field profile (A_j, φ_j) is updated based on the obtained based on the direction of the steepest ascent. The optimization process continues until a satisfied phase profile $\phi(x,y)$ is obtained. The profile for a single trap can then be easily extrapolated to a trap array by applying Fourier shift theorem to every lattice site in the array.

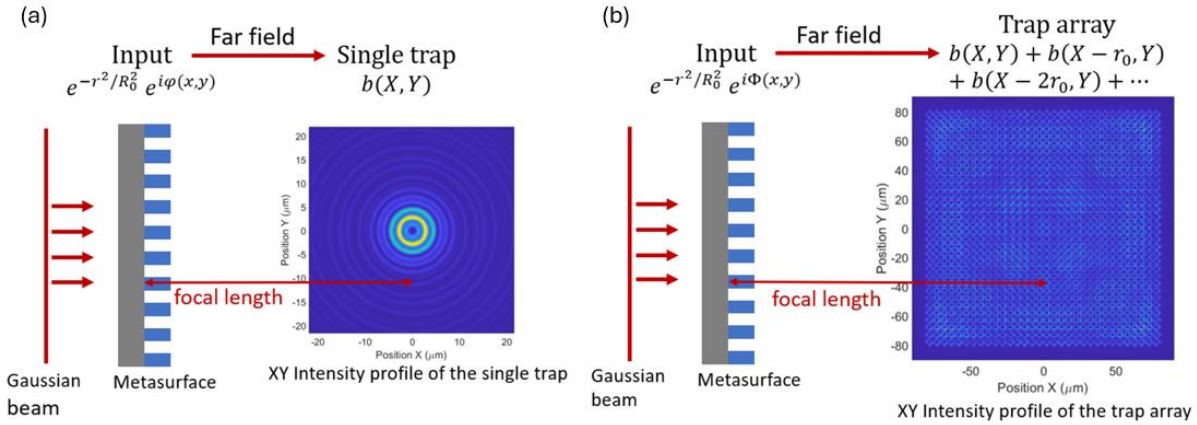

Figure 2-21 (a) Generation of a single bottle beam trap at designed focal length using a metasurface and a single gaussian beam; (b) Modification of the phase profile using Fourier shift theorem allowing the generation of a bottle beam trap array (Fang, et al., 2024).

We then realize a metasurface bottle beam trap generator for Rubidium arrays operating at 770nm using the silicon-on-sapphire (SOS) platform in section 2.3 (Fang, et al., 2024). The phase profile $\phi(x,y)$ is approximated by an array of cylindrical pillars with a periodicity of 360 nm and height of 500 nm. The fabrication method is similar to the procedure described in section 2.3. Figure 2.22b show the SEM image of the fabricated metasurface. The tapered sidewall of the meta-atoms and the missing element in the array indicates the same fabrication imperfection detailed in section 2.3.

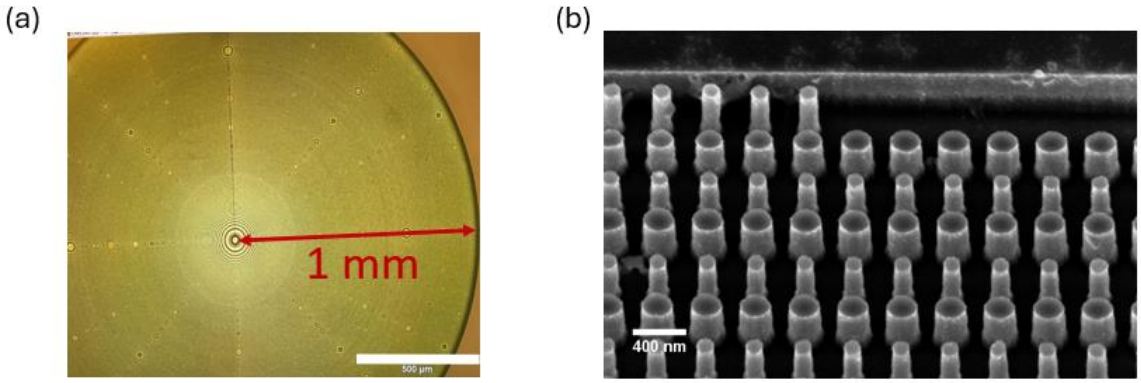

Figure 2-22 (a) Fabricated metasurface bottle beam generator with $r = 1\ mm$; (b) SEM image of the meta-atoms (Fang, et al., 2024).

We build an optical setup to characterize optical behavior of the bottle beam trap generator. The setup consists of a 795nm DBR laser as the light source since a 770nm laser is not readily available. Still, the low quality factor of the silicon pillar means that the optical response should not deviate too much from that of the designed wavelength. The light source is delivered to the setup by a PM fiber and launched by a fiber collimator. The laser beam is then expanded by a pair of lenses to achieve the designed incident waist diameter and directed onto the metasurface. The bottle beam trap array forms at the focal point of the metasurface and is being imaged by a microscope setup consisting of an objective lens, a tube lens and a NIR camera. Figure 2.23c shows the image taken on the focal plane of the metasurface where the bottle beam array profile is clearly visible, indicating that the overall feature of the dark trap (low intensity center + high intensity surrounding sphere) is fairly insensitive to the fabrication imperfection listed above.

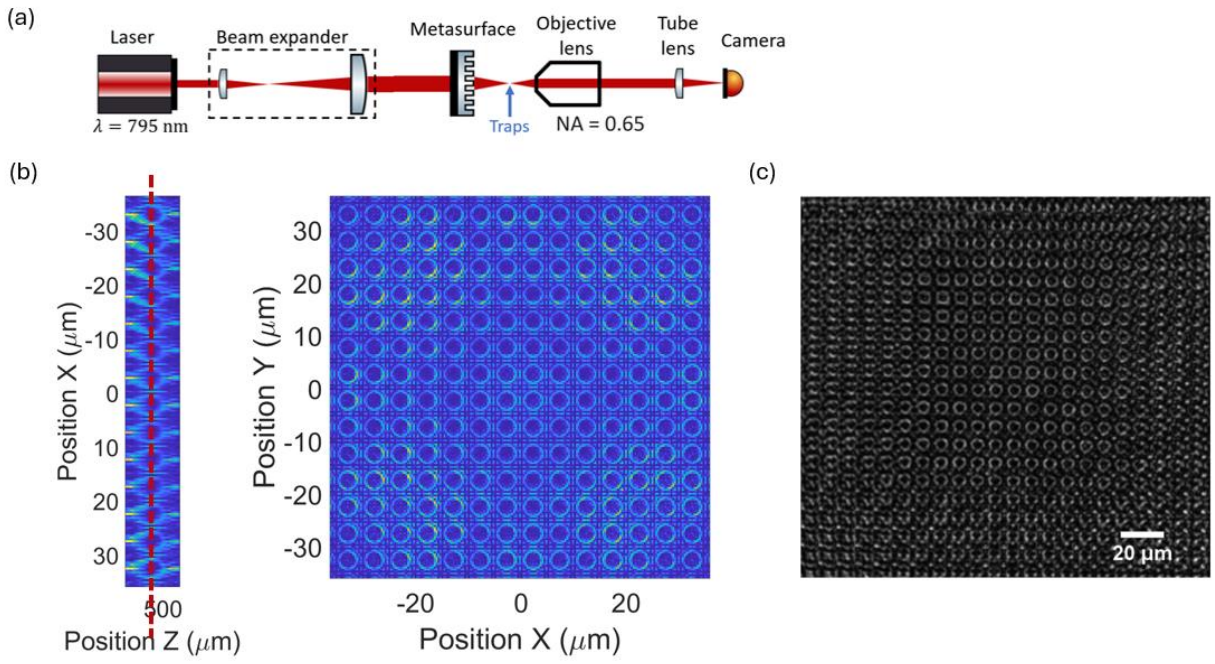

Figure 2-23 (a) Experimental setup for the optical characterization of the metasurface; (b) Simulated metasurface bottle beam trap profile; (c) Measured intensity profile of the array of bottle beams. The quality of the traps at the edge degrades due to lens distortion (Fang, et al., 2024).

2.7 Conclusion and outlooks

In this chapter, we have successfully designed, simulated, fabricated and characterized metasurface devices aimed for various applications in neutral atom based quantum systems. For designing the metasurface, two methods are developed – one based on direct calculations of phase responses with given input and output light field profiles, and one based on optimization method with gradient descent with respect to a given figure of merit of the metasurface device that depends on the specific application. For simulating the meta-atoms and metasurface devices, we have implemented a full wave FDTD simulation based on a commercially available software (Lumerical) for small-scale metasurfaces and approximate techiques based on angular spectrum method (ASM) for large scale metasurface devices. In collaboration with Kats group and Argonne National Laboratory (ANL), we have successfully fabricated and characterized a metasurface polarizing beam splitter for signal detection in rubidium based atomic magnetometry and a metasurface bottle beam trap generator for generating trapped rubidium atom (arrays) for quantum computing applications. Optical characterization shows that both devices have achieved their desired functionality (polarization splitting and bottle beam forming). In addition, we have designed and simulated a polarizing splitting meta-lens aimed at improving and compactifying the magnetometry signal detection and collection system for rubidium atomic magnetometers.

Despite the general success, the fabricated metasurface devices deviate significantly from their simulated performance primarily due to fabrication imperfection. The metasurface PBS suffers from significant transmission loss due to heavy reflection, and exhibits low polarization splitting efficiency due to the presence of undeflected zeroth order and higher order diffractions. Meanwhile, the dark trap generated by the metasurface bottle beam generator exhibits distortion of the trapping beam profile, causing potential leakage channels for the atom to escape. The less-than-ideal behavior can be contributed to fabrication imperfections, specifically the parameter drifting during E-beam writing and silicon etching, which results in distortion of meta-atoms from their designed geometries. Furthermore, metasurface devices are generally highly sensitive to optical alignment, which could be hard to achieve during optical characterizations. Potential mitigating strategies in the future includes improved metasurface designs that are insensitive to minor geometrical distortions, optimized fabrication techniques taking into consideration the parameter drifts and careful experiment setup designs to minimize alignment errors.

3 Atomic magnetometry with chip scale optics

In this chapter, we demonstrate atomic magnetometry using a metasurface polarizing beamsplitter fabricated on a silicon-on-sapphire (SOS) platform. The metasurface splits a beam that is near-resonant with the rubidium atoms (795 nm) into orthogonal linear polarizations, enabling measurement of magnetically sensitive circular birefringence in a rubidium vapor through balanced polarimetry. We incorporated the metasurface into an atomic magnetometer based on nonlinear magneto optical rotation (NMOR) and measured sub-nanotesla sensitivity, which is limited by low-frequency technical noise and transmission loss through the metasurface. To our knowledge, this work represents the first demonstration of SOS nanophotonics for atom-based sensing and paves the way for highly integrated, miniaturized atomic sensors with enhanced sensitivity and portability.

3.1 Introduction

Atomic magnetometers based on optically pumped atomic vapor are capable of some of the most sensitive measurements of magnetic fields, which are enabled by advances in semiconductor lasers and preparation of atomic spins with long coherence times (Budker & Romalis, Optical magnetometry, 2007; Kominis, Kornack, Allred, & Romalis, 2003; Keder, Prescott, Conovaloff, & Sauer, 2014). In combination with advances in miniaturized atomic vapor cell fabrication (Kominis, Kornack, Allred, & Romalis, 2003; Keder, Prescott, Conovaloff, & Sauer, 2014; Griffith, Knappe, & Kitching, 2010; Hunter, et al., 2018; Jiménez-Martínez, et al., 2009; Knappe, et al., 2010; Krzyzewski, Perry, Gerginov, & Knappe, 2019), atomic magnetometers are suitable for a host of field applications including biomagnetic imaging in ambient conditions (Johnson, Schwindt, & Weisend, 2013; Johnson, Schwindt, & Weisend, 2010; Wylie, 2012), and magnetic anomaly detection (Canciani & Raquet, 2016). In the most general configuration for an optically pumped atomic magnetometer involving a single optical axis, an optical beam nearly resonant with an atomic transition is used to simultaneously polarize atomic spins in an alkali vapor such as rubidium, and probe magnetically sensitive spin rotation within that medium through a polarization change induced on the input beam (Johnson, Schwindt, & Weisend, 2010; Shah & Romalis, 2009). This setup is compatible with miniaturized components for realizing chip-scale atomic magnetometers, but the utilization of bulk birefringent optics for polarization control and measurement in these devices still poses a limit on the ultimate sensor volume and scalability. Therefore, recent research has focused on the development of nanophotonic components (Sebbag, Naiman, Talker, Barash, & Levy, 2020; Sebbag, Talker, Naiman, Barash, & Levy, 2021; Hu, et al., 2022; Xu, et al., 2024; Yang, Benelajla, Carpenter, & Choy, 2023; Talker, et al., 2022) to replace bulk optical elements to achieve a higher degree of miniaturization and integration in atomic magnetometers.

In this work, we have proposed integration of inline optically pumped magnetometer (OPM) with metasurface-based polarization components, with specific focus on two OPM schemes: single beam spin exchange relaxation free (SERF) magnetometer and nonlinear magneto-optical rotation (NMOR) magnetometer for their simplicity and high sensitivity. We then evaluate the accuracy and sensitivity of atomic magnetometry using the miniaturized balanced detection scheme by developing an imperfect PBS model, taking into consideration of the fact that metasurface polarizing optics usually exhibit dichroism, non-ideal PER and multiple loss channels, and combining it with magnetometer response calculated through the evolution of spin polarization (and higher order multipole moments) under laser-atom-field interaction. Finally, we experimentally demonstrate atomic magnetometry with rubidium atoms, using the chip-scale polarizing beamsplitter (PBS) to analyze the atomic spin alignment through balanced polarimetry (Figure 2.7a). We have chosen silicon-on-sapphire (SOS) as the material system for our metasurface, which is a mature material platform widely used in the microelectronics industry (Ipri, 1981), due to its excellent thermal stability, electrical insulation, and radiation resistance (Cristoloveanu, 1987). The wide optical transparency window of sapphire combined with the high refractive index and moderately low absorption loss of single-crystalline silicon ($n = 3.69$ and $\kappa < 0.01$ at 795 nm, as measured with spectroscopic ellipsometry shown in Figure 2.7c) make the SOS platform an attractive candidate for nanophotonic components in the near-infrared (700 nm – 1100 nm), especially devices that do not require propagation over long distances or sharp resonances. The near-infrared wavelength range encompasses many atomic transitions (Steck, Rubidium 87 D line data, 2001; Steck, Cesium D line data, 2003) relevant for quantum sensing (Kitching, Knappe, & Donley, Atomic sensors–a review, 2011; Kitching, Chip-scale atomic devices, 2018) and information processing (Saffman, Walker, & Mølmer, 2010; Adams, Pritchard, & Shaffer, 2019) applications. In addition, sapphire has a low permeability to gases, is chemically stable, and has been used as a window material in microfabricated silicon alkali metal vapor cells (Kurashima, Matsumae, Yanagimachi, Harasaka, & Takagi, 2019; Matsumae, Kurashima, Higurashi, & Takagi, 2019; Sekiguchi, Sato, Ishikawa, & Hatakeyama, 2017; Neuman, Wang, & Gallagher, 1995; Lorenz, Dai, Green, Asnicar, & Cundiff, 2008). Therefore, SOS nanophotonic components can potentially be pre-patterned on sapphire windows prior to their bonding to vapor cells. To our knowledge, this work is the first experimental demonstration of the use of SOS nanophotonics in atom-based technologies. We have selected nonlinear magneto-optical rotation (NMOR) as the operating scheme for our prototype metasurface-incorporated atomic magnetometer and obtained a measured sensitivity below one nanotesla (nT), which is limited by our experimental apparatus and the optical loss through the metasurface. Our metasurface PBS splits the incident light into orthogonal linear polarizations and can be used in combination with a differential photodetector to directly measure the magnetically sensitive circular birefringence in the atomic medium (Figure 2.7a). In comparison to recent work demonstrating polarimetry of atomic spins using metasurfaces designed with the Pancharatnam-Berry phase (Sebbag, Talker, Naiman, Barash, & Levy, 2021; Xu, et al., 2024) (which separate polarization components into circular polarization bases and can therefore directly measure circular dichroism), our technique is more suitable for cases where the

circular birefringence is more magnetically sensitive than circular dichroism, including modulation-free NMOR (Zhang, Jin, Qu, & Xiao, 2021) and spin exchange relaxation-free (SERF) magnetometry (Shah & Romalis, 2009). Portions of this chapter have been published in (Yang, Benelajla, Carpenter, & Choy, 2023) and (Yang, et al., 2024).

3.2 Analysis of atomic magnetometry using metasurface optics for balanced polarimetry

In this section, we evaluate how the optical performance of our proposed metasurface PBS affects balanced polarimetry and thereby the sensitivity and accuracy of the atomic magnetometer. Our PBS design is compatible with millimeter-scale, microfabricated Rb cells involving separate non-parallel (Liang, et al., 2022) or inline pump and probe beams. Since microfabricated vapor cells usually allow only one optical access path, we focus on the magnetometry schemes that are compatible with inline pump-probe configurations such as the Mx (Arnold, Siegel, Grisanti, Wrachtrup, & Gerhardt, 2017), Bell-Bloom (Jiménez-Martínez, et al., 2009), Spin exchange relaxation free (Shah, Knappe, Schwindt, & Kitching, 2007), and nonlinear magneto-optical rotation (Budker D. , Kimball, Yashchuk, & Zolotorev, 2002) magnetometers. Of the above schemes proposed, we choose NMOR and SERF as platforms for performance evaluation against metasurface PBS. NMOR, which is capable of detecting very weak fields, has the advantage of technical simplicity, since the pump and probe beam can come from the same laser, and it does not require extensive heating. Unlike SERF which must be operated near zero field to maintain its high sensitivity, NMOR can be extended to relatively high fields (μT level) using light modulation techniques without compromising much of its sensitivity and accuracy.

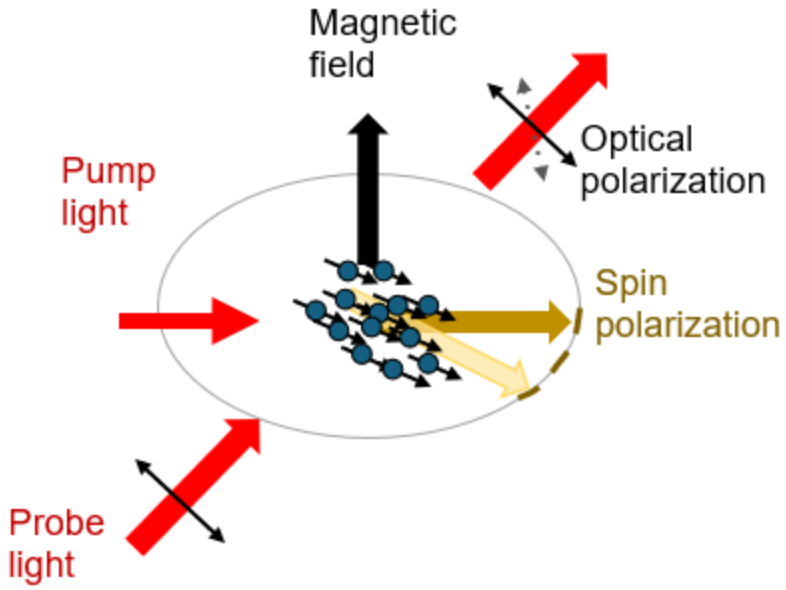

Figure 3-1 Working principle of atomic magnetometry. The pump light polarizes the atomic ensemble into magnetic-sensitive states while the magnetic field information is extracted by detecting the state change (amplitude, polarization) of the probe light.

Meanwhile, SERF is still an attractive candidate since it provides the highest sensitivities among all and has been demonstrated to achieve sub-picotesla sensitivity in microfabricated cells (Shah, Knappe, Schwindt, & Kitching, 2007). Moreover, while the shot-noise-limited sensitivity of SERF magnetometry is expected to degrade with decreasing cell size (Yang, Benelajla, Carpenter, & Choy, 2023), SERF operation relies on a high buffer gas pressure which is also necessary in very small ($\lesssim$ mm^3) vapor cells to prevent decoherence from collisions of the atoms with the cell wall. A high buffer gas pressure would broaden atomic transitions and preclude the operation of NMOR (Yang, Benelajla, Carpenter, & Choy, 2023). Finally, SERF using elliptically polarized light has shown very promising results with device scale down to 5 mm (Sebbag, Talker, Naiman, Barash, & Levy, 2021; Arnold, Siegel, Grisanti, Wrachtrup, & Gerhardt, 2017) and can require only a single optical beam to operate (Shah & Romalis, 2009; Johnson, Schwindt, & Weisend, 2010), and thus highly compatible with nanophotonic integration.

We thus choose SERF magnetometry using a single elliptical beam as the platform for evaluating the sensitivity of a metasurface-integrated magnetometer (Shah & Romalis, 2009). In this scheme, an elliptically polarized light close to the ^{87}Rb D1 transition interacts with a ^{87}Rb vapor cell of optical path length l and Rb number density n to generate atomic spin polarization. This same optical beam is used to detect spin polarization via balanced polarimetry. An amplitude-modulating field is applied along the direction of magnetic field measurement (along x) which

must be transverse to the light propagation direction; all other field components are nulled. The optical signal is then detected using lock-in detection at the modulation frequency (ω_{mod}). The theory of operation for SERF magnetometry with elliptical light was worked out in (Shah & Romalis, 2009) for the case of an ideal PBS with transmittance $T = 1$ and infinite polarization extinction ratio. In this scenario, the balanced polarimetry gives the polarization angle rotation ϕ via the differential signal of the two outputs from the PBS:

$$\mathcal{D} = E_0^2 e^{-\sigma n l} \cos(2\beta) sin\phi \tag{3.1}$$

where ϕ is proportional to the spin polarization along the optical axis, E_0 is the electric field amplitude, $e^{-\sigma n l}$ is related to light absorption by Rb atoms (whereby σ is the photon absorption cross section for unpolarized Rb atoms), β is the ellipticity of the light and is set to $\pi/8$. In the low polarization limit, the signal $\mathcal{D}$ is linear in terms of spin polarization P_z. This optical rotation will allow us to determine the transverse magnetic field.

3.2.1 Effects of polarization-dependent transmittance and PER on SERF magnetometry

Note that the differential signal $\mathcal{D}$ shown in equation (3.1) only includes the polarization rotation term induced by circular birefringence. Such simplicity cannot be assumed for our metasurface PBS which has a non-negligible transmittance difference for the two orthogonal linear polarization and polarization leakage. We thus modify the theory to incorporate these non-idealities. We model the metasurface PBS as a $2 \times N$ linear system, where the 2 input channels indicates the incident optical power in the two orthogonal linear polarization modes: $I_{x,in} = |\langle \hat{x}|\psi\rangle|^2, I_{y,in} = |\langle \hat{y}|\psi\rangle|^2$. Here, ψ is the input state of the incident beam. N represents the outputs from the metasurface, which consists of N scattered modes and can be usually cutoff at $|N| = 2$ as the power in higher order modes diminishes fast as $|N|$ increases. The output power distribution between the modes is therefore given by the transmission matrix T:

$$I_j = \sum_{k=x,y} T_{jk}\, I_{k,in} \tag{3.2}$$

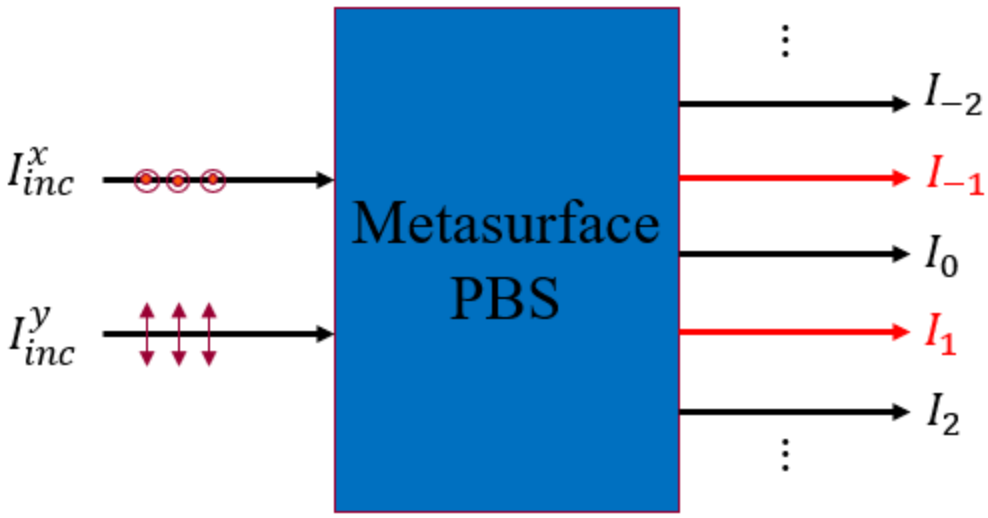

Figure 3-2 Model of an imperfect metasurface PBS with two input polarization modes (x and y) and multiple output channels. Channels in red ($I_{1/-1}$)are the designed output ports of the metasurface PBS, while I_0 represents the center undeflected order and $I_m(|m| > 1)$ represents the higher diffraction orders.

.

Here, I_j is the power scattered into the j-th mode, T_{jk} is the transmission for a purely k polarized incidence into the j-th mode.

For our design, x polarization goes into -1st mode while y polarization goes into +1st mode, and only the optical power of these two modes are detected in the experiment. We therefore denote T_{-1x} and T_{+1y} as the polarization splitting efficiency for x and y polarization, while T_{-1y} and T_{+1x} indicates the polarization crosstalks. The outputs of the PBS become:

$$\begin{aligned} I_{-1} &= T_{-1x}I_{x,in} + T_{-1y}I_{y,in} \\ I_{+1} &= T_{+1x}I_{x,in} + T_{+1y}I_{y,in} \end{aligned} \tag{3.3}$$

i.e. the two outputs are now a linear superposition of the light intensities along two orthogonal polarization axes. The direct consequence of this intensity mixture is that the differential signal will now contain an additional term due to circular dichroism that is proportional to σ.

We represent the electric field of the incident laser beam with arbitrary polarization and amplitude in the x and y polarization basis: $E = c_1\hat{x} + c_2 i\hat{y}$ where c_1 and c_2 are complex numbers. If the optical axes of the PBS are oriented with respect to the $x - y$ coordinate by angle δ, then the two outputs of the metasurface PBS are:

$$\begin{aligned} I_{-1} &= \mathcal{P}\left(T_{-1x}|c_1 cos\delta + ic_2 sin\delta|^2 + T_{-1y}|-c_1 sin\delta + ic_2 cos\delta|^2\right) \\ I_{+1} &= \mathcal{P}(T_{+1x}|c_1 cos\delta + ic_2 sin\delta|^2 + T_{+1y}|-c_1 sin\delta + ic_2 cos\delta|^2) \end{aligned} \tag{3.4}$$

Here $\mathcal{P}$ is some constant is related to vacuum permittivity and detection efficiency. With the differential signal being:

$$\begin{aligned}\mathcal{D} = I_{-1} - I_{+1} \\ &= \mathcal{P}[(T_{-1x} - T_{+1x})|c_1 cos\delta + ic_2 sin\delta|^2 - (T_{+1y} \\ &\quad - T_{-1y})|-c_1 sin\delta + ic_2 cos\delta|^2] \\ = \mathcal{P}[(T_{-1x} - T_{+1x})&(|c_1|^2 cos^2\delta + i(\bar{c_1}c_2 - c_1\bar{c_2})sin\delta cos\delta + |c_2|^2 sin^2\delta) \\ &- (T_{+1y} \\ &- T_{-1y})(|c_1|^2 sin^2\delta + i(c_1\bar{c_2} - \bar{c_1}c_2)sin\delta cos\delta + |c_2|^2 cos^2\delta)]\end{aligned} \tag{3.5}$$

In the absence of an atomic medium, $|c_1|^2 = cos^2\beta, |c_3|^2 = sin^2\beta, \bar{c_1}c_2 - c_1\bar{c_2} = 0$. Let $\mathcal{D} = 0$ and we get the expression for δ that balances the two outputs:

$$tan^2\delta = \frac{(T_{-1x} - T_{+1x})cos^2\beta - (T_{+1y} - T_{-1y})sin^2\beta}{(T_{+1y} - T_{-1y})cos^2\beta - (T_{-1x} - T_{+1x})sin^2\beta} \tag{3.6}$$

The interaction of the field with rubidium atoms causes polarization rotation and ellipticity change, with the coefficients now being:

$$\begin{aligned}|c_1|^2 = \frac{1}{2}[&\left(e^{-n\sigma l(1+P_z)} + e^{-n\sigma l(1-P_z)}\right) + \left(e^{-n\sigma l(1+P_z)} - e^{-n\sigma l(1-P_z)}\right)sin2\beta \\ &+ 2e^{-n\sigma l}cos2\beta\cos\phi]\end{aligned} \tag{3.7}$$

$$\begin{aligned}|c_2|^2 = \frac{1}{2}[&\left(e^{-n\sigma l(1+P_z)} + e^{-n\sigma l(1-P_z)}\right) + \left(e^{-n\sigma l(1+P_z)} - e^{-n\sigma l(1-P_z)}\right)sin2\beta \\ &- 2e^{-n\sigma l}cos2\beta\cos\phi]\end{aligned} \tag{3.8}$$

$$\bar{c_1}c_2 - c_1\bar{c_2} = -2ie^{-n\sigma l}cos2\beta\sin\phi \tag{3.9}$$

where $\phi = cr_e fnlP_z Re(L(\nu))$ is the polarization rotation angle. Here c is the speed of light in vacuum; r_e is the classical electron radius; $f \cong \frac{1}{3}$ is the oscillator strength of the rubidium D1 transition; l is the optical path length; n is the Rb number density; P_z is the atomic spin polarization along z direction; $L(\nu) = \frac{1}{\nu_0 - \nu + i\frac{\Delta\nu}{2}}$ is the pressure-broadened Lorentzian profile with a full width at half maximum $\Delta\nu$ centered at ν_0. Plug in the expressions for c_1, c_2 and δ into expression equation (3.5), and select $\mathcal{P}$ such that our result reduces to the expression given in formula (3.1) when $T_{-1x} = T_{+1y} = 1, T_{-1y} = T_{+1x} = 0$, we have:

$$\begin{aligned}\mathcal{D} = \frac{1}{8}E_0^2[&\Big((T_{-1x} - T_{+1x}) - (T_{+1y} - T_{-1y})\Big) \\ &\times \left(e^{-n\sigma l(1+P_z)} + e^{-n\sigma l(1-P_z)} + sin2\beta\left(e^{-n\sigma l(1+P_z)} - e^{-n\sigma l(1-P_z)}\right)\right) \\ &+2((T_{+1y} - T_{-1y}) - (T_{-1x} - T_{+1x}))e^{-n\sigma l}\cos\phi)\end{aligned} \tag{3.10}$$

$$+4\left((T_{-1x}-T_{+1x})+(T_{+1y}-T_{-1y})\right)$$
$$\times\sqrt{1-\left(\frac{(T_{+1y}-T_{-1y})-(T_{-1x}-T_{+1x})}{cos2\beta((T_{-1x}-T_{+1x})+(T_{+1y}-T_{-1y}))}\right)^2}\,e^{-n\sigma l}cos2\beta\sin\phi)]$$

Expanding and keep the first order of P_z, we have obtained the differential signal:

$$\mathcal{D}=E_0^2e^{-\sigma nl}(\eta\cos(2\beta)\sin\phi+\frac{\left((T_{+1y}-T_{-1y})-(T_{-1x}-T_{+1x})\right)}{4}\sigma nlsin(2\beta)P_z) \quad (3.11)$$

where

$$\eta=\frac{(T_{-1x}-T_{+1x})+(T_{+1y}-T_{-1y})}{2}\sqrt{1-\left(\frac{(T_{+1y}-T_{-1y})-(T_{-1x}-T_{+1x})}{\cos(2\beta)((T_{-1x}-T_{+1x})+(T_{+1y}-T_{-1y})}\right.} \quad (3.12)$$

We see that the imperfect PBS results in two modifications in the expression of the differential signal: first, the original polarization rotation signal is attenuated by a factor of η; second, the imperfect PBS introduces another term related to the change of the polarization ellipticity induced by the circular dichroism of the atomic medium, which is also proportional to P_z in the low polarization limit.

We will now compare the magnetometry signal of a metasurface-integrated magnetometer with one based on ideal optics (namely, a PBS with near unity transmittance, ultra-high PER, and no linear dichroism). We use identical excitation and cell conditions as in (Shah & Romalis, 2009), in which the Rb vapor cell is filled with 300 Torr helium and 100 Torr nitrogen and heated to 200 ℃. The laser frequency detuning is set to $v_0-\nu=45\ GHz$. These conditions lead to a linewidth $\Delta\nu$ of 7.97 GHz, optical pumping rate of 880 Hz, and a spin relaxation rate of 1200 Hz. Figure 3.3 shows the differential signal $\mathcal{D}$ as a function of the transverse magnetic field B_x for magnetometers based on ideal optics (red) and our metasurface design (blue) for a vapor cell with $l=5\ mm$. We can see from the Figure 3.3 that the incorporation of the metasurface PBS into the magnetometer does not change the dispersive character of the signal and only modifies the signal amplitude by a scaling factor ξ that is given by:

$$\xi=\eta+\frac{\left((T_{+1y}-T_{-1y})-(T_{-1x}-T_{+1x})\right)}{8}\frac{\Delta\nu}{\nu_0-\nu} \quad (3.13)$$

For our design, $\xi\cong 0.788$. The metasurface polarization extinction ratios are still sufficiently high, such that $T_{-1y},T_{+1x}\ll 1$. Additionally, there is no significant linear dichroism $|T_{-1x}-T_{+1y}|\ll 1$ and the laser detuning is sufficiently larger than the pressure-broadened linewidth.

Under these conditions, the signal amplitude is simply attenuated by the mean transmittance of $\hat{x}$ and $\hat{y}$ polarization: $\xi \cong \frac{T_{-1x}+T_{+1y}}{2}$. Finally, it may be possible to further improve the metasurface design using adjoint optimization methods (Lalau-Keraly, Bhargava, Miller, & Yablonovitch, 2013; Mansouree, McClung, Samudrala, & Arbabi, 2021; Wambold, et al., 2020) that minimize the figure of merit (FOM) defined as $FOM = \left|\frac{(T_{+1y}-T_{-1y})-(T_{-1x}-T_{+1x})}{(T_{-1x}-T_{+1x})+(T_{+1y}-T_{-1y})}\right|$. This analysis can also serve as a useful guideline for designing nanophotonic components for other quantum sensors.

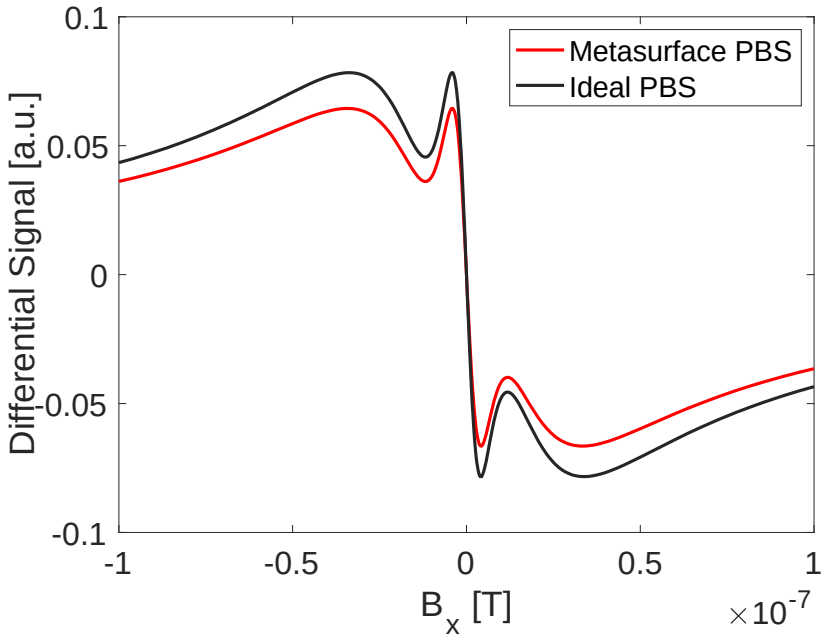

Figure 3-3 Simulated differential signal $\mathcal{D}$ with lock-in detection at the modulating frequency ω_{mod} as a function of B_x with an ideal PBS (red) and metasurface PBS (blue).

Let us now discuss what conditions the transmittance and PER of the PBS should satisfy to generate a dispersive signal with discernible amplitude. Note that under the SERF condition, the atomic vapor is usually dense enough that the modification of the optical absorption due to spin polarization $\Lambda = n\sigma l P_z$ is no longer small enough for the first order approximation to remain valid (except for sufficiently small vapor cells, see Figure 3.4). Therefore, the polarimetry signal from circular dichroism (which is the one related to $Im(L(\nu))$) is no longer dispersive due to the even power terms in the expansion. We thus require this term to be suppressed compared to the term due to polarization rotation:

$$\frac{|(T_{+1y}-T_{-1y})-(T_{-1x}-T_{+1x})|}{8}tan2\beta\frac{\Delta\nu}{\nu_0-\nu} \ll \frac{(T_{-1x}-T_{+1x})+(T_{+1y}-T_{-1y})}{2}\sqrt{1-\left(\frac{(T_{+1y}-T_{-1y})-(T_{-1x}-T_{+1x})}{cos2\beta((T_{-1x}-T_{+1x})+(T_{+1y}-T_{-1y}))}\right)} \quad (3.14)$$

In addition, the relative amplitude $\mathcal{A}$ of the polarization rotation signal

$$\mathcal{A} = e^{-\sigma nl}cos2\beta\frac{(T_{-1x}-T_{+1x})+(T_{+1y}-T_{-1y})}{2} \times\sqrt{1-\left(\frac{(T_{+1y}-T_{-1y})-(T_{-1x}-T_{+1x})}{cos2\beta((T_{-1x}-T_{+1x})+(T_{+1y}-T_{-1y}))}\right)^2} \quad (3.15)$$

should be maximized once equation (3.14) is satisfied.

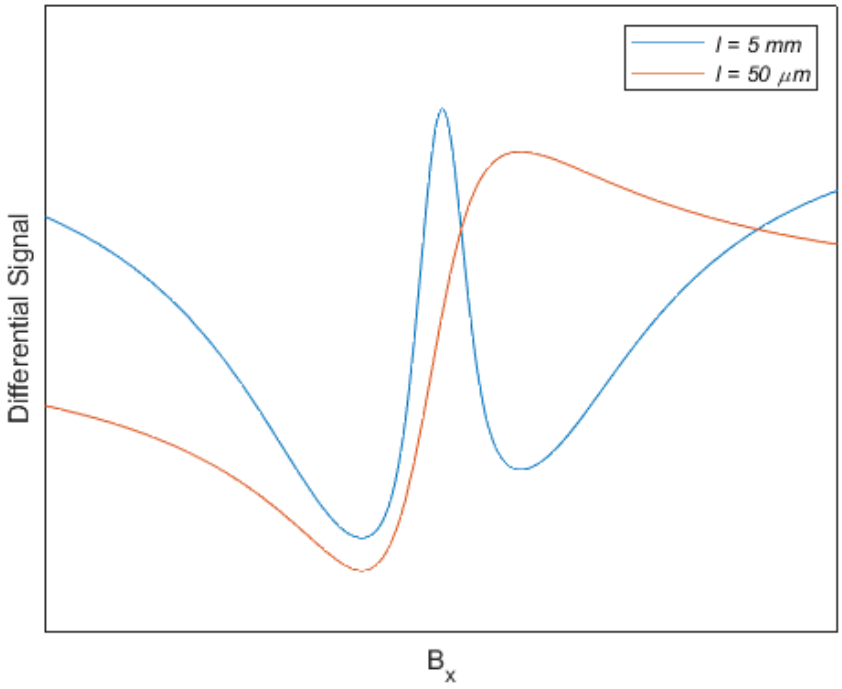

Figure 3-4 Simulated differential signal $\mathcal{D}$ due to circular dichroism for a vapor cell with optical path length of $5\ mm$(blue) and $50\ \mu m$(red). The figure is not to scale and only shows the overall shape of the signal.

Using the laser detuning, ellipticity, and linewidth specified in (Shah & Romalis, 2009), we rewrite the condition in equation (3.14) in terms of the figure of merit (FOM):

$$FOM = \left|\frac{(T_{+1y} - T_{-1y}) - (T_{-1x} - T_{+1x})}{(T_{-1x} - T_{+1x}) + (T_{+1y} - T_{-1y})}\right| \ll 0.707 \tag{3.16}$$

Considering that the FOM is bounded to ≤ 1, we therefore see that equation (3.14) can be easily satisfied. In addition, the signal can be further optimized by choosing a different ellipticity β and detuning $\nu_0 - \nu$. For a sufficiently small vapor cell such that $\Lambda = n\sigma l P_z \ll 1$, equation (3.14) is no longer required, and we can instead maximize the signal in the linear P_z regime:

$$\mathcal{D} = \xi E_0^2 e^{-\sigma n l} \cos 2\beta \sin\phi \tag{3.17}$$

3.2.2 Impact of metasurface PBS on magnetometer noise

We now discuss the impact of the metasurface PBS on the various noise sources accompanying the atomic magnetometer signal. It is shown in (Shah, Knappe, Schwindt, & Kitching, 2007) that in a single-beam, millimeter-scale magnetometer based on absorption measurement, the laser intensity noise dominates. The laser intensity noise can arise from laser current fluctuations or light polarization drifts that are converted into amplitude noise by a linear polarizer at the input. The SERF scheme we adopted for miniaturization in this paper uses balanced polarimetry as well as spin modulation with lock-in detection, which are capable of suppressing the intensity noise (Shah & Romalis, 2009; Chen, et al., 2022). A sensitivity of 7 $fT/\sqrt{Hz}$ was reported in a centimeter-scale cell in (Shah & Romalis, 2009), with the dominant noise source being the Johnson noise from the magnetic shield.

The residual laser intensity noise will contribute to the overall technical noise (which also includes electronic noise) which will limit the signal-to-noise ratio (SNR) of the measurement. Since the metasurface PBS scales the differential signal amplitude by $\xi \cong 0.788$, we expect the SNR of the metasurface-integrated magnetometer to scale by a similar amount. Based on the inverse relationship between sensitivity and SNR (Lucivero, Anielski, Gawlik, & Mitchell, 2014), the magnetic field sensitivity will thus degrade by about a factor of 1.27.

In addition to its impact on detection, laser intensity noise also affects the optical pumping rate and light shifts experienced by atoms (Krzyzewski, Perry, Gerginov, & Knappe, 2019; Wylie, 2012). The light shift effect is equivalent to a fictitious magnetic field along the light propagation direction (z) with its amplitude proportional to the laser intensity. In (Shah & Romalis, 2009), the light shift effect is countered by applying a magnetic field in the opposite direction that minimizes the magnetic resonance linewidth. If the laser intensity noise is present, there will always be a small fictious field δB_z that is not balanced. Fortunately, if the noise amplitude is small enough such that $\gamma \delta B_z \tau \ll 1$, then it is shown in (Cohen-Tannoudji C. , Dupont-Roc, Haroche, & Laloë,

1970) that the induced change in atomic polarization P_z is of second order in δB_z, rendering the error negligible.

3.3 Nonlinear magneto-optical rotation magnetometer using the metasurface PBS

3.3.1 Basic theory of NMOR

Magneto-optical rotation describes the rotation of the polarization plane of a (linearly) polarized light as it propagates through the medium under an external magnetic field (Grosz, Haji-Sheikh, & Mukhopadhyay, 2017). First discovered by Faraday in 1845 in solids and later by Macaluso and Corbino in gases, it quickly become a field of active research interest and leads to the discovery of many other magneto-optical effects (Rochester, 2010).

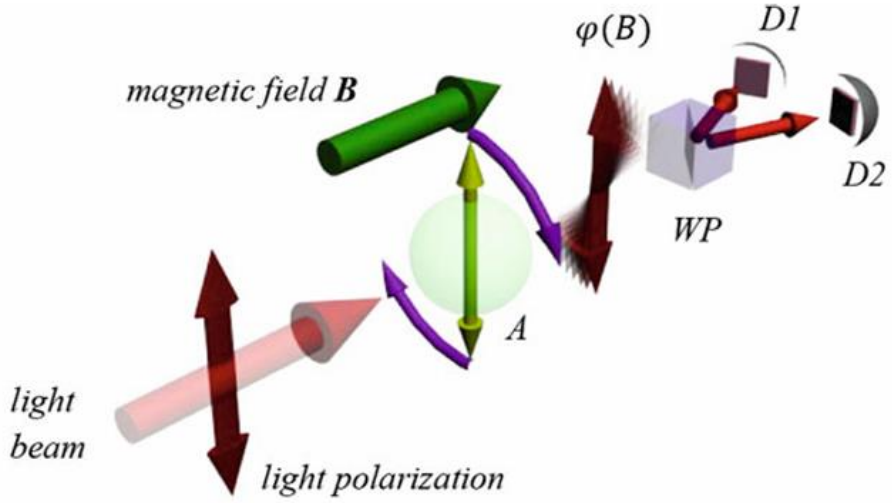

Figure 3-5 Demonstration of Faraday rotation. The linearly polarized light goes through medium A under a longitudinal magnetic field B. The magnetically induced rotation of the polarization plane $\varphi(B)$ is detected by a balanced polarimetry setup consisting of a Wollaston prism (WP) and two photodiodes. Figure reproduced from (Grosz, Haji-Sheikh, & Mukhopadhyay, 2017).

The Faraday effect is essentially a magnetic field induced circular birefringence of the medium. We will restrict ourselves to atomic medium in the following discussion. As shown in Figure 3.5, a linearly polarized light, which can be decomposed into an equal superposition of left-handed circularly (LHC) polarized light and right-handed circularly (RHC) polarized light, is passing through an atomic medium under the influence of a longitudinal magnetic field B_z. Suppose the light is near resonant with an $F = 1 \rightarrow F' = 0$ transition, the external field B_z shifts the ground

state $m_F = \pm 1$ level by $\Delta\omega = \pm g_F \mu_B B_z$. It can then be shown that the refractive index for the LHC (n_+) and RHC (n_-) is (Budker, Kimball, & DeMille, Atomic physics: an exploration through problems and solutions, 2004):

$$n_\pm = 1 + 2\pi\chi_0 \frac{\gamma_0}{2\left(\Delta\omega \mp g_F \mu_B B_z\right) + i\gamma_0} \tag{3.18}$$

Here χ_0 is the linear susceptibility, $\Delta\omega$ is the light detuning and γ_0 is the decay rate of the excited state. The optical rotation φ due to this circular birefringence can be expressed as:

$$\varphi = \frac{\omega l}{2c} Re(n_+ - n_-) = \frac{2\pi\chi_0 \omega l}{c} \frac{b[1 + b^2 - (2\Delta/\gamma_0)^2]}{(2\Delta/\gamma_0)^2 + [1 + b^2 - (2\Delta/\gamma_0)^2]^2} \tag{3.19}$$

where ω is the laser frequency, l is the length of the medium, $b = \frac{2 g_F \mu_B B_z}{\gamma_0}$.

It is obvious that the Faraday rotation curve forms a resonance around $B_z = 0$ with the magnetic linewidth determined by the optical transition linewidth γ_0. In a thermal vapor, γ_0 can be on the order of GHz due to various broadening mechanisms (Doppler broadening, pressure broadening, etc.), making high sensitivity magnetometry a challenge. However, for very low light intensities, narrow features that depend on light intensity occur near the zero of the magneto-optical rotation curve. This effect is called nonlinear magneto-optical rotation (NMOR). While several mechanisms can contribute to NMOR, the one that gives the narrowest linewidth and explored in this work for magnetometry is due to ground state coherence (Grosz, Haji-Sheikh, & Mukhopadhyay, 2017).

Let us again consider the atomic transition $F = 1 \rightarrow F' = 0$. Just as a circularly polarized light pumps the atomic medium towards the stretched state $|m_F = \pm 1\rangle$ and creates atomic polarization, a linearly polarized light along x leaves atoms in $|m_F = 0\rangle$ and $(|m_F = -1\rangle + |m_F = 1\rangle)/\sqrt{2}$ since they are dark states for x polarized light. This creates atomic alignment (magnetic quadrupole) along x in the medium, making it more transparent to x polarization while more absorbing to y polarization, similar to a linear polarizer. Just like atomic polarization, atomic alignment also undergoes Larmor precession under magnetic field, and this precession makes the alignment a 'rotating polarizer' until it eventually relaxes, thus creating a polarization rotation of the light due to linear dichroism. Since the ground state coherence exhibits much longer relaxation time than the excited state, extremely narrow NMOR feature can be obtained, making fT/$\sqrt{Hz}$ sensitivity possible in a dynamic range of 10^{-10} T (Budker, Yashchuk, & Zolotorev, Nonlinear magneto-optic effects with ultranarrow widths, 1998).

3.3.2 Effects of polarization-dependent transmittance and PER on NMOR magnetometry

Similar to section 3.2, we expect our imperfect metasuface PBS have a detrimental effect on the magnetometry signal (polarization rotation) when incorporated into the balanced polarimetry setup. However, we are going to show that, to the first order, the detected polarization rotation signal is only an attenuation of the real rotation signal, with no circular dichroism entering the detected signal. This result significantly simplifies the sensitivity analysis of the metasurface based NMOR magnetometry.

For NMOR magnetometers, the input light is linearly polarized: $|\psi\rangle = cos\alpha|\hat{x}\rangle + sin\alpha|\hat{y}\rangle$ with α_0 being the azimuth angle. For our metasurface PBS, the detected output becomes:

$$I_{-1} = T_{-1x}cos^2\alpha_0 + T_{-1y}sin^2\alpha_0 \tag{3.20}$$

$$I_{+1} = T_{+1x}cos^2\alpha_0 + T_{+1y}sin^2\alpha_0 \tag{3.21}$$

The output should be balanced when there is no optical rotation occurring, which sets the value of α_0:

$$tan^2\alpha_0 = \frac{T_{-1x} - T_{+1x}}{T_{+1y} - T_{-1y}} \tag{3.22}$$

After NMOR occurred, the output polarization state becomes $|\psi\rangle = (\cos(\alpha_0 + \alpha)cos\epsilon - isin(\alpha_0 + \alpha)sin\epsilon)|\hat{x}\rangle + (\sin(\alpha_0 + \alpha)cos\epsilon + icos(\alpha_0 + \alpha)sin\epsilon)|\hat{y}\rangle$ where $\alpha_0, \epsilon \ll 1$ are the newly acquired polarization rotation and ellipticity change. It can be shown that:

$$\alpha_{det} = \frac{I_{-1} - I_{+1}}{2(I_{-1} - I_{+1})} = \sqrt{(T_{-1x} - T_{+1x})\big(T_{+1y} - T_{-1y}\big)}\,\alpha - cos2\alpha_0(\alpha^2 + \epsilon^2) \tag{3.23}$$

which proves the assertion at the beginning of this Chapter. For our fabricated metasurface PBS, we expect the attenuation coefficient $\eta = \sqrt{(T_{-1x} - T_{+1x})(T_{+1y} - T_{-1y})} = 0.3$.

3.3.3 Experiment apparatus and setup for metasurface-integrated NMOR magnetometer

In this section, we describe our implementation of an NMOR magnetometer with the metasurface PBS serving as part of the signal detection system. The experiment setup for our metasurface-based atomic magnetometry is shown in Figure 3.6a. The same DBR laser that is used to characterize the metasurface PBS now serves as both the pump and probe beam. Aside from the laser controller, a reconfigurable laser servo (Vescent D2-125) containing a tunable PI^2D loop is used for frequency locking purposes. The error signal for locking is the derivative of the saturated spectroscopy signals which is generated by first modulating the laser current with a 4 MHz

dithering signal and then demodulate the output signal from the photodiode relative to the dither signal. This enables us to lock the laser to the optical transition peaks (dips) from the atomic spectroscopy. We lock the laser to the hyperfine transition $F = 2 \rightarrow F' = 1$ of the D1 line of ^{87}Rb since it generates the largest optical rotation signal in our setup.

Before the frequency locked laser is coupled into a polarization-maintaining fiber, a polarimeter is used to make sure the laser polarization before coupling gives the best extinction ratio. This procedure ensures a lower polarization noise. The laser beam then passes through a linear polarizer (PER > 10^5) to clean up the polarization before going into a liquid crystal noise eater (Thorlabs NEL03A) to stabilize the optical intensity. We found the intensity stabilization necessary for our NMOR magnetometer as the lack of optical or RF modulation results in a magnetometry signal heavily affected by the low frequency noise. The noise eater has a bandwidth of 2.5 kHz and a > 150 noise attenuation factor at 10 Hz. A half waveplate sets the polarization angle before it enters the vapor cell. The vapor cell is a 25 mm×75 mm cylinder containing isotopically enriched 87Rb and is coated with Paraffin, an anti-relaxation coating which prolongs the atomic polarization lifetime, leading to a much narrower NMOR feature. The vapor cell is being heated by a flexible resistive foil heater (Thorlabs HT10K) with an integrated NTC10k thermistor. Temperature stabilization is managed by an alternating current heater controller (Twinleaf TCHF). The heater controller outputs AC current up to 500kHz which minimizes stray field perturbations to atomic polarization. The vapor cell is housed within a four layer magnetic shield (Twinleaf MS-1L) with a shielding factor of 10^6 to reduce the ambient magnetic noise. The built-in three-axis and gradient coil system inside the shield allows precise magnetic field control in the center of the shielded volume. The coils are powered by a three-channel low noise bipolar current supply (Twinleaf CSBA) with pA/$\sqrt{Hz}$ level current noise density and $\pm$30 mA range. The current can be adjusted manually through a turning knob or voltage-modulated through the analog servo input. For field calibration during the measurements, a 3-axis magnetoresistive probe (AlphaLab MR3) was co-located with the vapor cell and gives real-time reading of the magnetic field.

After passing through the vapor cell, the laser beam is re-collimated by a pair of achromatic doublets to a waist diameter of 0.67mm to accommodate for the size of the metasurface PBS. To set up the balanced polarimetry for measuring NMOR, a half waveplate before the metasurface sets the polarization angle so that the intensity difference between the designed output L1 and R1 from the metasurface is zero when the longitudinal magnetic field B_z is zero. A free space balanced amplified photodetector (Thorlabs PDB210A) with a common mode rejection ratio of 40 dB measures the optical power difference between L1 and R1 and generates a voltage signal proportional to that difference, which is also proportional to the optical rotation of the laser. Finally, the differential output from the balanced detector was collected and analyzed by a National Instrument multifunction I/O device (PCIe 6363). The PCIe 6363 has a maximal sampling rate of 2 Ms/s and 16bits analog input resolution (1660 μV in absolute accuracy at full scale). For each

magnetometry measurement (at a specific B_z value), we collect data for 10s with a sampling rate of 1 Ms/s and take the average value.

3.3.4 Magnetometry results and discussions

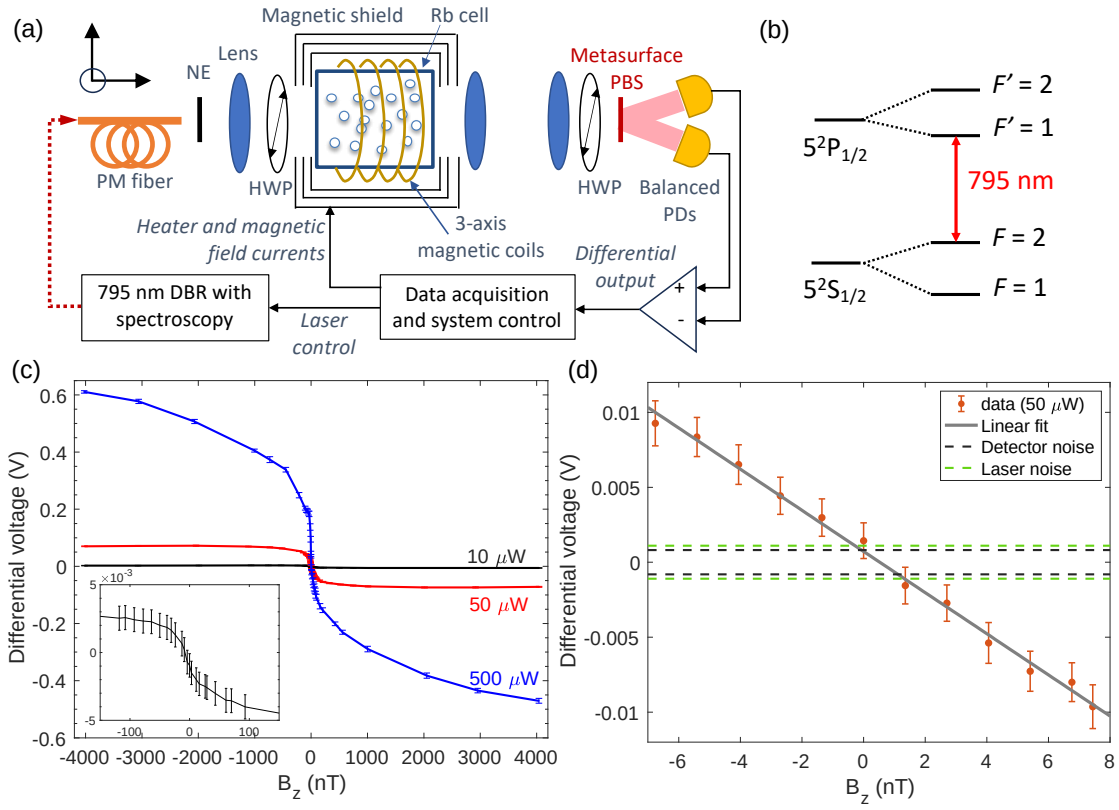

Figure 3-6 (a) Schematic of the atomic magnetometry setup in which polarimetry is performed with a metasurface PBS. PM fiber: polarization-maintaining fiber; NE: noise-eater; HWP: half-wave plate; PD: photodiode. (b) Energy level diagram for the NMOR measurement, in which the incident beam is tuned to the $F = 2 \rightarrow F' = 1$ transition in ^{87}Rb. (c)-(d) Differential voltage signal as a function of applied magnetic field, for different optical powers. The inset in (c) shows the signal around zero field for a pump power of 10 μW, while (d) shows the signal around zero field for a pump power of 50 μW. The error bars at each data point indicate the standard deviations in the recorded time trace, while the dotted lines represent the standard deviations of the non-magnetic noise contributions from the detector and laser.

Figure 3.6c shows the differential voltage output from the balanced detector under different optical powers as the longitudinal field is manually swept across zero. The curves all show magnetic sensitivity in the differential voltage near zero field ($|B_z| < 100$ nT). At each input power, the sharp slope observed near the zero-field point is attributed to the paraffin coating preserving the atomic alignment over thousands of atom-wall collisions (Budker D. , Kimball, Rochester, Yashchuk, & Zolotorev, 2000; Rochester, 2010). As predicted by the calculation in (Rochester, 2010), a lower light intensity gives rise to a narrower NMOR feature. However, operating under

20 μW was not ideal in our setup due to the limited signal-to-noise ratio (SNR) in the photo-detection. In our setup, we found that $P = 50\ \mu\text{W}$ (corresponding to $I = 400\ \mu\text{W/cm}^2$) yielded the best magnetic sensitivity as a compromise between SNR and magnetic linewidth. As the reference magneto-resistive probe measurements became unreliable with longitudinal fields below 5 nT, we performed a finer characterization of the differential signal with respect to small longitudinal field at this light intensity by a slow sweeping of the current around zero field. Figure 3.6d shows the differential voltage signal swept across a few nTs (with the values of the applied magnetic field calculated using specifications by the coil manufacturer). The linear fit of the differential signal gives a slope of $-1.373\ \text{mV/nT}$, which translates to a noise-equivalent magnetic field of 0.8660 nT at $B_z = 0$ based on a voltage noise of $\sigma(V_{diff}) = 1.189\ \text{mV}$ (measured by the standard deviation of the differential voltage near zero field).

We will now analyze the sensitivity of the metasurface NMOR magnetometer. Consider the measured (voltage) signal $V(t)$ of the magnetometer. Let us assume that the time-dependent signal follows a stationary process, which means we ignore the long term drifting of the experimental parameters and make the assumption that the mean and variance of the measured magnetometry signal does not change with time. Then the signal can be expressed as $V(t) = S + x(t)$, where S is the 'real' magnetometry signal and $x(t)$ is the noise involved in the process with $\langle x(t) \rangle = 0$. For an evaluation of the magnetometer sensitivity, we define the noise equivalent magnetic field (or minimum detectable field) B_{min} as the field value when

$$S = \sqrt{\langle x(t)^2 \rangle} \tag{3.24}$$

Under this model, the long term drifts as well as the magnetometer accuracy are not considered, although they are important issues to address in real applications.

In the experiment, we selected a sampling rate f_s as well as a total sampling time $T = n_s f_s$, where n_s is the total number of samples. Increasing T allows more samples to be collected and leads to a better estimation of magnetometry signal or noise power, but is prone to long-term drifting errors. According to the Nyquist criterion, the reconstructed function $V_s(t)$ is bandwidth limited to $\frac{f_s}{2}$, i.e. the Fourier transform $\widehat{V_s}(f)$ is 0 when $f > \frac{f_s}{2}$. At this bandwidth-limited condition, the noise amplitude is given by

$$\sigma = \sqrt{\frac{2}{T}\int_0^{\frac{f_s}{2}} |\hat{x}(f)|^2 df} \tag{3.25}$$

Sometimes, the magnetometry signal is recovered by phase-sensitive lock in detection. In such cases, the integration range is further suppressed by the time constant τ of the lock in amplifier, which is related to the cutoff frequency f_c by:

$$f_c = \frac{1}{2\pi\tau} \tag{3.26}$$

Essentially, choosing a large time constant results in better noise suppression, at the cost of detection bandwidth (i.e. unable to respond to fast-varying signals).

Fundamentally, the sensitivity of any optically pumped atomic magnetometer is limited by the projection noise $\delta B_{pj} = \frac{h}{g\mu_B}\sqrt{\frac{1}{NT_2\tau}}$, the photon shot noise $\delta B_{ph} \propto \sqrt{\frac{1}{N_{ph}\tau}}$ and the probe light back-action (AC stark shift)[2017]. Here, N is the atom number, T_2 is the spin relaxation time, N_{ph} is the photon flux impinged on the detector and τ is the measurement time related to measurement bandwidth BW by $BW = \frac{1}{2\tau}$. We can estimate the contribution of δB_{pj} and δB_{ph} as follows: $N = nV = nSL = 10^{11}\ cm^{-3} \times 0.94\ cm^3 = 9.4 \times 10^{10}$ where S and L are the laser beam area and cell length, respectively. For our paraffin-coated cell, $T_2 \approx 1\ ms$ and measurement time $\tau = 1\ \mu s$. Therefore, $\delta B_{pj} \approx 1.05 \times 10^{-17}\ T$. For an estimation of δB_{ph}, notice that an alternative way of expressing the photon shot noise is through the uncertainty of the measured optical rotation: $\delta\theta = \sqrt{\frac{1}{4\Phi\tau}}$ where $\Phi = \frac{P\lambda}{hc} \approx 2 \times 10^{13} s^{-1}$ is the photon flux from either of the PBS channels when operating in balanced polarimetry mode. Here $P \approx 5\ \mu W$ is the approximate optical power detected at a single PBS output channel in the experiment. We can convert the measured optical rotation into photodetector output voltage by using $\delta\theta \approx \frac{\Delta P}{2P} = \frac{A\Delta V}{2P}$ which results in a voltage uncertainty of $\Delta V \approx 0.335 mV$. Here $A = 300 \times 10^3\ V/W$ is the conversion gain of the photodetector. Therefore, the photon shot noise $\delta B_{ph} = \frac{0.335 mV}{1.373 \frac{\text{mV}}{\text{nT}}} = 0.244$ nT.

In reality, magnetometers typically perform worse than these limits due to technical noises stemming from non-ideal operating conditions. One major source of technical noises comes from environmental fluctuations along the light propagation path caused by mechanical vibrations, thermal drifts, air turbulence, etc., which results in alterations in the intensity, polarization, wavefront and profile of the laser and laser-atom interactions. Another source of technical noise comes from electronics such as power supplies, electromagnetic pickups, photodetectors and data acquisition systems (Grosz, Haji-Sheikh, & Mukhopadhyay, 2017). Unlike the spin projection noise or the photon shot noise which are white noises, technical noises usually exhibit unique frequency spectrums.

We first examined the electronic noises by blocking out the laser and collected 10^7 sample points in 10 s. The standard deviation among the sample points was 0.8449 mV, which is assumed to be the RMS noise caused by electronics. Since the sampling rate is 1 Ms/s, the measurement bandwidth $BW = \frac{1}{2\tau} = 500$ kHz. The photodetector has a noise density of 0.66 μV/$\sqrt{Hz}$, which

contributes to a noise of $\sigma_{det} = 0.4667$ mV if we assume a white noise-like characteristic. For the data acquisition system PCIe 6363, we estimated an RMS noise of < 17 μV. The rest of the noise can be attributed to the AC line clearly visible in the noise spectrum in Figure 3.7, where harmonics of 50 Hz and 60 Hz are present.

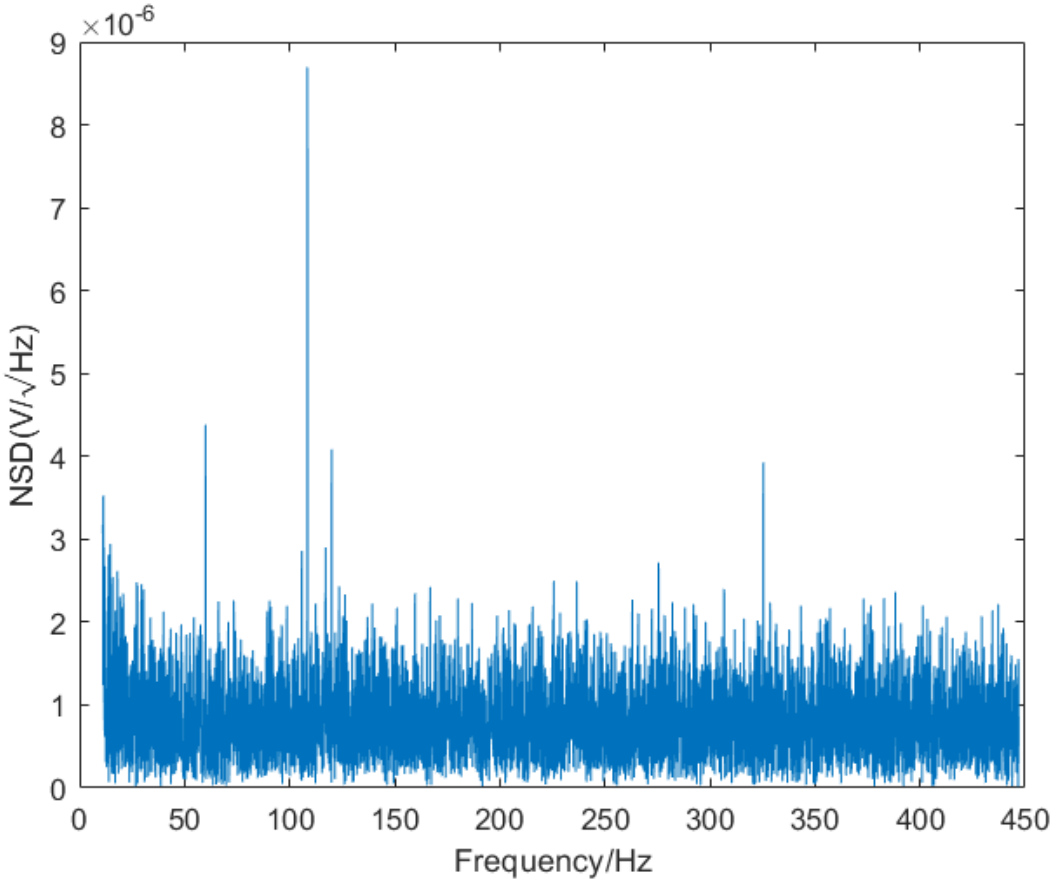

Figure 3-7 Noise spectrum density (NSD) of the measured magnetometry signal where the AC line noises (harmonics of 50 & 60 Hz) are visible.

We then characterized the laser noise contribution due to intensity and polarization instability (which converts to intensity noise through polarizing optics like linear polarizer and PBS). To decouple the laser noise from the magnetic noise, we detuned the laser far from any atomic transitions of rubidium by > 10 GHz, where both the linear and nonlinear magneto-optical effects are small. We measured a voltage noise of 1.111 mV with the same sampling condition and an incident laser power of 50 μW. The results indicate that the detection is limited mainly by photodetector noise and laser noise. Therefore, increasing the polarization splitting efficiency of the metasurface will directly improve the SNR and boost the magnetic sensitivity. Other possible

improvements include using a higher-quality cell coating (Graf, et al., 2005) for increased ground state alignment lifetime, performing detection at frequencies where technical noises are suppressed through modulation techniques (Lorenz, Dai, Green, Asnicar, & Cundiff, 2008), and varying the transverse field to obtain a sharper magnetic resonance feature (Budker, Yashchuk, & Zolotorev, Nonlinear magneto-optic effects with ultranarrow widths, 1998).

3.4 Conclusion and outlooks

We have successfully demonstrated rubidium atomic magnetometry using an SOS metasurface PBS operating in the linear polarization basis. By measuring the differential voltage signal proportional to the optical rotation without any phase sensitive (lock-in) detection, we directly measured the magnetometer sensitivity using the outputs of the metasurface PBS. Our experiment shows the effectiveness of the metasurface PBS in magnetometry signal detection and paves the way for nanophotonic integration of atomic magnetometers on an SOS platform.

The magnetometry scheme used for this demonstration is based on DC NMOR near zero field and thus prone to low-frequency noise especially without lock-in detection. Therefore, our sensitivity is limited by low-frequency photodetector and laser noise. Moreover, the dynamic range of DC NMOR is severely limited and actually exhibits an inverse relationship versus sensitivity (formula 3.19). This makes sensitive magnetic field detection beyond nanotesla range unfeasible. However, as first discovered by Bell and Bloom (Bell & Bloom, 1957), the obstacle can be alleviated by modulating the light at $2\omega_L$ to achieve synchronous optical pumping, where ω_L is the Larmor frequency corresponding to the external field amplitude. This method essentially shifts the detection to twice the Larmor frequency and circumvents the low frequency technical noises. The dynamic range of NMOR can be also extended to near geo-field level, limited by nonlinear Zeeman effect and alignment to orientation conversion (Grosz, Haji-Sheikh, & Mukhopadhyay, 2017).

In section 3.2, we showed that the detected differential signal under an imperfect PBS (for example, one that demonstrates linear dichroism and transmission loss) is attenuated by a coefficient $\xi < 1$ that depends on its transmission and PER (Yang, Benelajla, Carpenter, & Choy, 2023). Therefore, a magnetometer system dominated by the photodetector noise will benefit from an improvement in the metasurface PBS performance by increasing ξ and thus gaining higher SNR. Furthermore, an increase in the optical rotation signal allows one to operate in a lower optical power region, which can lead to a narrower magnetic resonance linewidth. In the near-term, the transmission efficiency of the metasurface PBS may be improved by incorporating antireflection coatings and the use of doped silicon to mitigate fabrication imperfections caused by charging. Additionally, the device area, limited to the order of mm^2 in this work, can be significantly increased by using 193 nm immersion lithography (Sanders, 2010; Hu, et al., 2018) whose resolutions are compatible with our metasurface design. Our work shows that SOS is a powerful

platform for integrating nanophotonics with atomic sensing. The high transparency in the near-infrared and ultra-low gas permeability in the sapphire substrate are well suited for integration with miniaturized rubidium or cesium vapor cells, while the high refractive index silicon enables efficient light manipulation, resulting in highly integrated atomic sensing platforms. Together with recent progress in photonic integrated circuits and laser technology, chip-scale atomic sensors with exceptional sensitivity, low footprint and high portability may be feasible in the future.

4 Progress towards a miniaturized and ruggedized cold atom gravimeter

4.1 Introduction

There has been continued interest in using cold atoms for inertial measurements. The working principle behind these sensors lies in the wave property of laser-cooled atoms. By spatially splitting the atomic wave packet through Raman or Bragg transition, two interferometry arms are formed as they sample through different space-time regions which induces a phase difference between them. This phase difference $\Delta\phi$ is highly sensitive to acceleration and rotation and can be extracted by recombining the split wave packets at the end of the interferometry for them to interfere and measuring the population difference of the two states involved. For a standard Mach-Zehnder interferometer measuring a uniform acceleration $\boldsymbol{a}$, the shot noise limited sensitivity is given by $\Delta a = \frac{1}{C\sqrt{N}k_{eff}T^2}$ where N is the atom number being interrogated, k_{eff} is the effective wavevector describing the momentum transferred to the atom by the light pulses and T is the interrogation time (Szigeti, Hosten, & Haine, 2021). State-of-the-art cold atom gravimeters have demonstrated an acceleration sensitivity level of $10^{-8}\, ms^{-2}\tau^{-1/2}$, while the cold atom gyroscope has achieved short-term sensitivities below $10^{-9}\, rads^{-1}\tau^{-1/2}$ level (Rosi, Sorrentino, Cacciapuoti, Prevedelli, & Tino, 2014; Mcguirk, Foster, Fixler, Snadden, & Kasevich, 2002; Durfee, Shaham, & Kasevich, 2006; Gustavson, Landragin, & Kasevich, 2000).

Compared to mechanical accelerators, cold atom inertial sensors do not have moving parts, and the proof mass (laser-cooled atom ensemble) is not coupled to the sensor case, making them less prone to in-run bias drift and nonlinear response. Since atoms are identical with well-known and stable physical properties, they are not susceptible to performance degradation and offer superior long-term stability with less calibration needs. Present and potential applications of cold atom inertial sensors include testing fundamental physics (Panda, et al., 2024; Yuan, Wu, & Yang, 2023; Herrmann, Dittus, Lämmerzahl, & others, 2012), high precision inertial navigation (Battelier, et al., 2016; Wright, et al., 2022; Garrido Alzar, 2019) and gravity field survey (Bidel, et al., 2020; Wu, et al., 2023).

However, cold atom inertial sensors seldom find their applications outside well-controlled laboratory environments (Butts, 2011). First, they are often limited in dynamic range and bandwidth compared to mechanical and fiber-optical sensors, and have dead times during cold atom preparation stage, making them generally unsuitable for capturing fast dynamics. Second, they require bulky and delicate infrastructures such as ultra-high vacuum, laser optics and control electronics, which severely limit the system's robustness when they are deployed in dynamic environment. In order to facilitate the transition of cold atom sensors from laboratory to field-deployable platforms, several issues such as power consumption, sensor footprint, complexity and transportability. In this Chapter, we report our progress towards building a cold rubidium atom

gravimeter as a testing platform for achieving ruggedization and miniaturization of the sensor capable of operating outside the laboratory while maintaining sensitivity superiority against classical sensors. I would like to thank my collaborator Steven Carpenter and Pree Mukherjee for helping building the cold atom experiment setup, including the vacuum system, optical setup and experiment control electronics. We would like to acknowledge Prof. Mikhail Kats and his group member Sanket Deshpande, for their collaboration on implementing the grating magneto-optical trap. Finally, we would like to acknowledge Prof. Deniz Yavuz and his group member David Gold for their helpful device in atom trapping and cooling, and thank David Gold and Steven Carpenter for developing the data processing tool for cold atom temperature measurement.

4.2 Theory of Raman light pulse cold atom interferometry

It is convenient to formulate atomic interferometry in Feynman's path integral setting, since in most situations the semiclassical approximation can be made for which the problem reduces to a calculation of the action S along the classical path. Further simplifications can be adopted if the Lagrangian L is quadratic, which is the case for atoms in a gravitational field. The following derivation is mainly adopted from (Storey & Cohen-Tannoudji, 1994).

Consider the transition amplitude or quantum propagator $K(z_2t_2, z_1t_1) = \langle z_2|U(t_2, t_1)|z_1\rangle$ of an atom to arrive at spacetime (z_2, t_2) starting from (z_1, t_1). According to Feynman's rule,

$$K(z_2t_2, z_1t_1) = \int [Dz] e^{\frac{i}{\hbar}S} \tag{4.1}$$

where the action $S = \int_{t_1}^{t_2} L\big(z(t), \dot{z}(t)\big)dt$ is path dependent. The integration on $[Dz]$ means summing over all paths connecting the end points in spacetime. At classical limit where $S \gg \hbar$, the complex exponent oscillates fast and cancels out between neighboring paths except near the classical path where S is extremal and the neighboring paths constructively interfere. For a Lagrangian that does not contain cubic or higher power terms, it can be shown that

$$K(z_2t_2, z_1t_1) = Ae^{\frac{i}{\hbar}S_c} \tag{4.2}$$

where S_c is the action along the classical path and A is a prefactor obtained from the Gaussian integral over small fluctuations around the classical path and is independent of z_1 and z_2.

Finally, we will assume that the atom's initial wavefunction is a plane wave:

$$\langle z|\psi_0\rangle = \frac{1}{\sqrt{2\pi\hbar}} e^{\frac{i}{\hbar}(p_0 z - E_0 t)} \tag{4.3}$$

With $E_0 = \frac{p_0^2}{2M}$.

We will now apply the path integral method to atomic interferometry. The interferometry starts by a $\frac{\pi}{2}$ pulse that coherently splits the wave packet to form two interferometer arms, followed by free evolution for a time duration of T, a π (mirror) pulse that interchanges the state for two interferometer arms, another free evolution of T, and finally another $\frac{\pi}{2}$ pulse to recombine the wave packets and form interference.

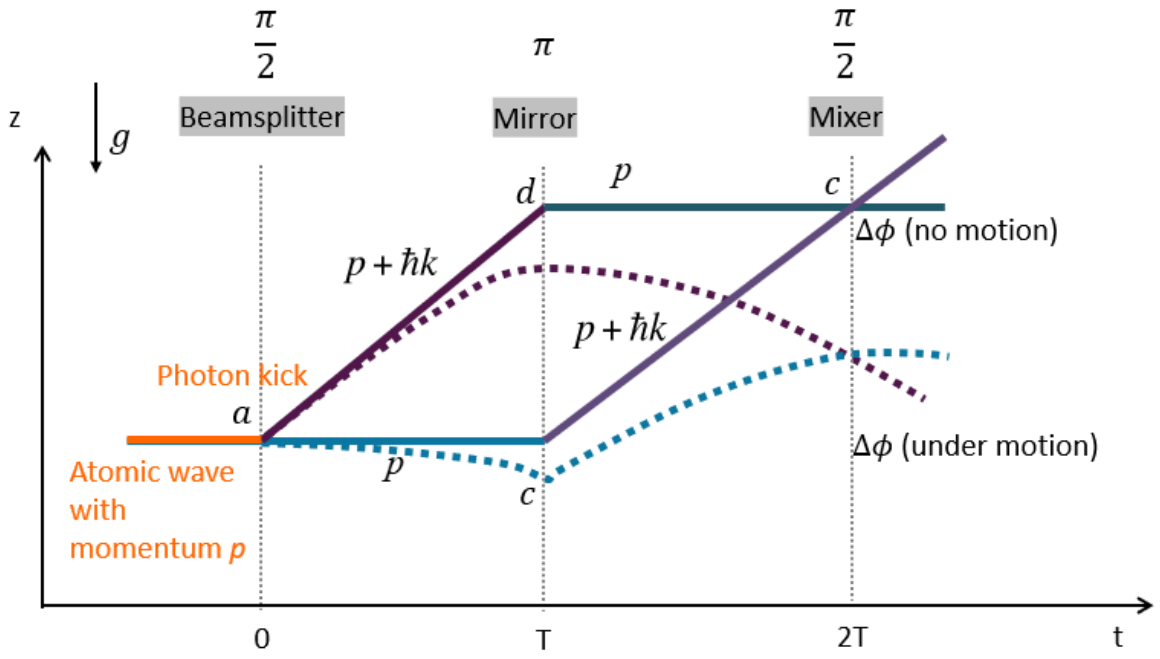

Figure 4-1 Trajectory of the $\frac{\pi}{2} - \pi - \frac{\pi}{2}$ interferometer paths for atoms propagating freely (bold) and under gravity $a = -g\hat{z}$ (dashed).

4.2.1 Propagation under gravitational field

The Lagrangian for a particle falling under gravitational field is:

$$L(z, \dot{z}) = \frac{1}{2}M\dot{z}^2 - Mgz \tag{4.4}$$

We can calculate the classical path by solving the Euler-Lagrange equation:

$$\frac{\partial L}{\partial z} - \frac{d}{dt}\left(\frac{\partial L}{\partial \dot{z}}\right) = 0 \tag{4.5}$$

which gives:

$$z(t) = z_0 + v_0(t - t_0) - \frac{1}{2}g(t - t_0)^2 \tag{4.6}$$

$$\dot{z}(t) = v(t) = v_0 - g(t - t_0) \tag{4.7}$$

The classical action along path $(z_1, t_1) \rightarrow (z_2, t_2)$ gives:

$$S_c(z_2 t_2, z_1 t_1) = \int_{t_1}^{t_2} L dt = \frac{M}{2}\frac{(z_2 - z_1)^2}{t_2 - t_1} - \frac{Mg}{2}(z_2 + z_1)(t_2 - t_1) - \frac{Mg^2}{24}(t_2 - t_1)^3 \tag{4.8}$$

Assume that the pulse duration is much smaller than T and the atoms start at $z_1 = 0, t_1 = 0$. Notice that the two wave packets overlap at the second $\frac{\pi}{2}$ pulse:

$$z_d = z_d^{(1)} = z_a + \left(2v_a + \frac{\hbar k_{eff}}{M}\right)T - 2gT^2 = z_d^{(2)} \tag{4.9}$$

The phase difference between the two wave packets due to free evolution during the first T:

$$\Delta S_{prop,1} = \frac{M}{2T}(z_b + z_c - 2z_a)(z_b - z_c) - \frac{MgT}{2}(z_b - z_c) \tag{4.10}$$

For the second free propagation:

$$\Delta S_{prop,2} = \frac{M}{2T}(2z_d - z_b - z_c)(z_c - z_b) - \frac{MgT}{2}(z_c - z_b) \tag{4.11}$$

Note that $z_b + z_c - 2z_a = (v_b + v_c)T - gT^2 = 2z_d - z_b - z_c$, which means $\Delta S_{prop,1} + \Delta S_{prop,2} = 0$, i.e. equal propagation time between pulses under uniform gravitational field yields zero phase difference as wave packets spend equal time in the two states and overlap at the end.

4.2.2 Atom-Laser interaction

In our experiment, the Raman laser pulses coherently manipulate the internal state of the atoms and generate the momentum kick needed to split the atomic wave packet. Again, we assume the pulse duration is so short that we can ignore the motion of the atom along the gravitational axis during the atom-laser interaction. This means that the three Raman pulses happen at definite points in spacetime: $(z_a, 0), (z_b(z_c), T), (z_d, 2T)$. The following derivation is mainly adopted from (Butts, 2011) and (Dunning, 2015).

For simplicity, we assume a three-level system: two ground state $|g_1\rangle$, $|g_2\rangle$ separated by the hyperfine splitting and a single excited state $|e\rangle$. Consider the Hamiltonian of the laser-atom interaction:

$$H = H_0 + V \tag{4.12}$$

where $H_0 = \frac{\boldsymbol{p}^2}{2M} + \hbar(\omega_1|g_1\rangle\langle g_1| + \omega_2|g_2\rangle\langle g_2| + \omega_3|e\rangle\langle e|)$ and $V = -\boldsymbol{d}\cdot\boldsymbol{E}$. Here, $\boldsymbol{E} = \boldsymbol{E_1}\cos(k_1 z - \omega_{L1}t + \phi_1^0) + \boldsymbol{E_2}\cos(k_2 z - \omega_{L2}t + \phi_2^0)$ is the Raman laser field. We assume that $\boldsymbol{E_1}$ couples $|g_1\rangle$ and $|e\rangle$ while $\boldsymbol{E_2}$ couples $|g_2\rangle$ and $|e\rangle$. Taken into account the momentum kick imparted by the Raman pulses, we can work in the basis $\psi(t) = c_1(t)|g_1, p\rangle + c_2(t)|g_2, p + \hbar(k_1 - k_2)\rangle + c_3(t)|e, p + \hbar k_1\rangle\}$. Apply the rotating wave approximation and switch to interaction picture, the evolution equations of the coefficient are:

$$\dot{c}_1 = \frac{i}{2}\Omega_{13}^* e^{i\Delta_1 t} c_3 \tag{4.13}$$

$$\dot{c}_2 = \frac{i}{2}\Omega_{23}^* e^{i\Delta_2 t} c_3 \tag{4.14}$$

$$\dot{c}_3 = \frac{i}{2}\left(\Omega_{13} e^{-i\Delta_1 t} c_1 + \Omega_{23} e^{-i\Delta_2 t} c_2\right) \tag{4.15}$$

Here, $\Omega_{sq} = \frac{\langle q|\boldsymbol{d}\cdot\boldsymbol{E_p}|s\rangle}{\hbar} e^{i\phi_s}$ is the Rabi frequency where $\phi_s = \phi_s^0 + \boldsymbol{k_s}\cdot\boldsymbol{z}$, $\Delta_1 = \omega_{L1} - (\omega_3 + \frac{(p+\hbar k_1)^2}{2M\hbar} - \omega_1 - \frac{p^2}{2M\hbar})$, $\Delta_2 = \omega_{L2} - (\omega_3 + \frac{(p+\hbar k_1)^2}{2M\hbar} - \omega_2 - \frac{(p+\hbar(k_1-k_2))^2}{2M\hbar})$. For Raman transitions, the detuning $\Delta \gg \Omega$, and we can apply adiabatic elimination to the excited state and turn the problem into a two level system:

$$\dot{c}_1 = -i\Omega_1^{AC} c_1 - \frac{i}{2}\Omega_R e^{i\delta t} c_2 \tag{4.16}$$

$$\dot{c}_2 = -i\Omega_2^{AC} c_2 - \frac{i}{2}\Omega_R e^{-i\delta t} c_1 \tag{4.17}$$

where $\Omega_s^{AC} = \frac{|\Omega_{sq}|^2}{4\Delta}$ is the light shift for state s, $\Omega_R = \frac{|\Omega_{13}||\Omega_{23}|}{2\Delta} e^{i\phi_{eff}} (\phi_{eff} = \phi_2 - \phi_1)$ is the effective Rabi frequency for the Raman transition, and $\delta = \Delta_1 - \Delta_2 = \omega_{L1} - \omega_{L2} - (\omega_{HF} + \boldsymbol{k_{eff}}\cdot\boldsymbol{v} + \frac{\hbar k_{eff}^2}{2M})$ is the effective Raman detuning. Here, ω_{HF} is the hyperfine splitting frequency since we are using hyperfine qubits for interferometry, $\phi_{eff} = \phi_2 - \phi_1$ is the effective phase for the complex Raman Rabi frequency, $\boldsymbol{k_{eff}} = \boldsymbol{k_1} - \boldsymbol{k_2} \approx \boldsymbol{2k_1}$ is the effective Raman wavevector (for the counterpropagating, Doppler-sensitive Raman transition). In the expression of Ω_s^{AC} and Ω_R, we have assumed that $\Delta = \Delta_1 \approx \Delta_2$ since generally $\delta \ll \Delta_i$. Notice that the light shift difference for the two ground state level could also contribute to the Raman detuning.

In general, equations (4.16) and (4.17) can be solved with dressed state approach. For resonant Raman transitions ($\delta = 0$), there is a simple solution when the atom is initially in ground state $|g_1\rangle$ with $c_1(t_0) = 1, c_2(t_0) = 0$:

$$c_1(t_0 + \tau) = cos\left(\frac{|\Omega_R|\tau}{2}\right) \tag{4.18}$$

$$c_2(t_0+\tau) = -ie^{i\phi_{eff}} sin\left(\frac{|\Omega_R|\tau}{2}\right) \tag{4.19}$$

From equation (4.18) and (4.19) we determine the pulse length for the resonant case: $t_{\pi/2} = \frac{\pi}{2|\Omega_R|}, t_\pi = \frac{\pi}{|\Omega_R|}$. Notice that the phase of the optical field ϕ_{eff} is imprinted into the atomic state, which allows for sweeping across the interference fringes by simply adjusting the phase of the optical field. In our setup, this is achieved by controlling the phase of the RF signal sent into the electro-optical modulator (EOM).

Let us now calculate the contribution from laser interaction to the phase difference between the two interferometer arms. We see from the previous derivation that effectively, we can represent the Raman laser by a single EM wave: $E_{eff}(z,t) = E_{0,eff}\cos(k_{eff}z - (\omega_{L1} - \omega_{L2})t + \phi_{eff})$

$$\begin{aligned}\Delta\phi_{laser} &= \Delta\phi_{\pi/2}^{(1)} + \Delta\phi_\pi + \Delta\phi_{\pi/2}^{(2)} \\ &= k_{eff}gT^2 + \phi_{eff,a}^0 - 2\phi_{eff,\frac{b}{c}}^0 + \phi_{eff,d}^0\end{aligned} \tag{4.20}$$

Aside from the static phase ϕ_{eff}^0 determined by the optical field, the phase difference accumulated in the gravitational field $k_{eff}gT^2$ is directly proportional to the enclosed area formed by the interferometry arms. The effective wave vector of the Raman field k_{eff} serves as a ruler for measuring the atomic motion under gravity with $k_{eff} \approx 390nm$. In the experiment, the gravitational acceleration value g is extracted by chirping the Raman effective detuning frequency at $\alpha = k_{eff}g$ such that the accumulated phase is cancelled for all interrogation time T.

4.3 Experiment apparatus

4.3.1 Vacuum system

Ultrahigh vacuum (UHV) is a necessity for cold atom interferometry as collisions with particles in the air can quickly heat up the trapped atoms and cause them to escape. In experiment, we found that magneto-optical trap fails to form at pressures higher than 1×10^{-7} Torr. UHV environment also prolongs the coherence time of atoms which is critical in quantum sensing.

4.3.1.1 Vacuum cell

The vacuum cell is where the cold atom experiment takes place. It must be UHV compatible and provide abundant optical access for lasers to address the atomic ensembles as well as for imaging and detection. In our setup, a 2 cm × 2 cm × 5 cm UHV glass cell from Infleqtion serves this purpose. The high optical flatness of the cell walls combined with wideband AR coating from 450

– 1070 nm ensures all-around optical access with minimum distortion. At the bottom of the cell, a 1.33-inch ConFlat (CF) flange connects the glass cell to the rest of the vacuum system.

Compared to standard vacuum chambers made from metals such as stainless steel, a glass cell offers the following advantages: (1) It is strictly non-magnetic and will not interfere with the magnetic field profile for atom trapping and manipulation; (2) It naturally provides the necessary optical access without the need for installing viewports on the chamber openings; (3) It is generally more compact in size, which is favorable for our purpose of building a miniaturized cold atom gravimeter.

4.3.1.2 Vacuum fittings, flanges and feedthroughs

To ensure compatibility with UHV for the whole vacuum system, CF flanges and fittings are adopted. The CF flanges have knife edges which cuts into metal gaskets, forming a tight metal-metal seal and enables operation at extremely high vacuum levels down to 10^{-13} Torr.

In our system, a flange multiplexer is mounted on the CF port of the vacuum cell. The flange multiplexer increases the number of vacuum ports available from 1 to 5, of which the middle one is used for a quartz viewport that enables another optical access from the bottom of the cell. Of the remaining four CF ports, the bottom one is sealed off with a blank flange. The upper one is used for a copper pinch off tube that connects to a turbomolecular pump for the initial pump-down process. The copper tube is pinched off to form a metal seal once the preliminary pumping is finished. On the left port, two rubidium dispensers are mounted on the inner pins of a UHV electrical feedthrough. When current is applied through the outer electrical pins, the dispenser inside begins to heat up and release ultrapure rubidium, serving as the atom source for the experiment. The atom flux can be controlled by simply adjusting the current amplitude. The right port of the multiplexer connects to an ion pump (Agilent Starcell) via a CF flange reducing nipple. The ion pump is responsible for pumping down the system to UHV and maintaining the vacuum level against outgassing and leakage in the system, which we will elaborate on section 4.3.1.3.

4.3.1.3 Vacuum pumping and Bake-out

Even though some vacuum pumps such as ion pump and titanium sublimation pump are designed to operate under and maintain UHV, it cannot be achieved through directly pumping down the system at room temperature. This is due to the fact that the materials making the vacuum components are always slowly releasing volatile compounds that contaminate the vacuum environment, limiting the ultimate vacuum level achievable. To counter this, we need to perform the bake-out procedure, which is essentially using high heat to remove these volatile compounds and accelerate the outgassing process with the help of vacuum pumps.

Before the system undergoes the bake out process, it is important to make sure the vacuum components are dust free and absent of grease contamination by thoroughly clea ning them (The quartz viewport, glass vacuum cell and atom sources are exempt from the procedure as they are already clean from factory and can be easily damaged in the process). This is accomplished by first gently scrubbing the components with dish soap to get rid of visible dirt. Next, the components are soaked in acetone and sonicated for 10 minutes (this procedure can be repeated once if necessary). After the vacuum parts are taken out, they are immediately submerged in isopropanol (99.9%) followed by 15 minutes sonication. Finally, the parts are blow-dried with ultrapure nitrogen and wrapped in cleanroom wipes or aluminum foils ready for use.

The bakeout is carried out in an oven to ensure all the vacuum parts are heated uniformly without creating significant temperature gradient or hot spots, which could cause structure deformation and lead to leakage. Before bakeout, we remove the magnet from the ion pump. Once the system is placed in the oven, a turbomolecular pump connects to the free flange of the copper pinch tube through a gate valve and begins to pump down the system to a vacuum level of 10^{-5} Torr. The temperature inside the vacuum is then carefully ramped up to 160 ℃ at a rate of 0.5 ℃/min. The system pressure will briefly increase to 10^{-4} Torr due to heating and accelerated outgassing, but eventually goes down to 10^{-7} Torr after one or two weeks of baking. During bakeout, a constant current of 1.8 A is applied to both atom sources, and once the bakeout is finished but the system is still pumped by the turbomolecular pump, several cycles of 5 A/ 30 seconds current burst are applied to the sources until the magnitude of the pressure spikes associated with the current burst stops falling. These steps remove the volatile contaminants on the atom sources. At this stage, the oven temperature is ramped down to room temperature at the same rate and a vacuum level of 10^{-8} Torr is obtained, indicating the success of the bakeout procedure. The oven is now opened and the ion pump activated by the Agilent 4UHV Ion Pump Controller, with pressure being measured by the ionization gauge in the ion pump. The gate valve is then closed, and a hydraulic press is used to pinch and sever the copper tube into two parts, and sealant (Torr Seal) is applied to the edge of the pinched-off tube, forming a UHV compatible seal to the vacuum system. The ion pump will continue to pump the system down to 3×10^{-10} Torr, ready for the cold atom experiments.

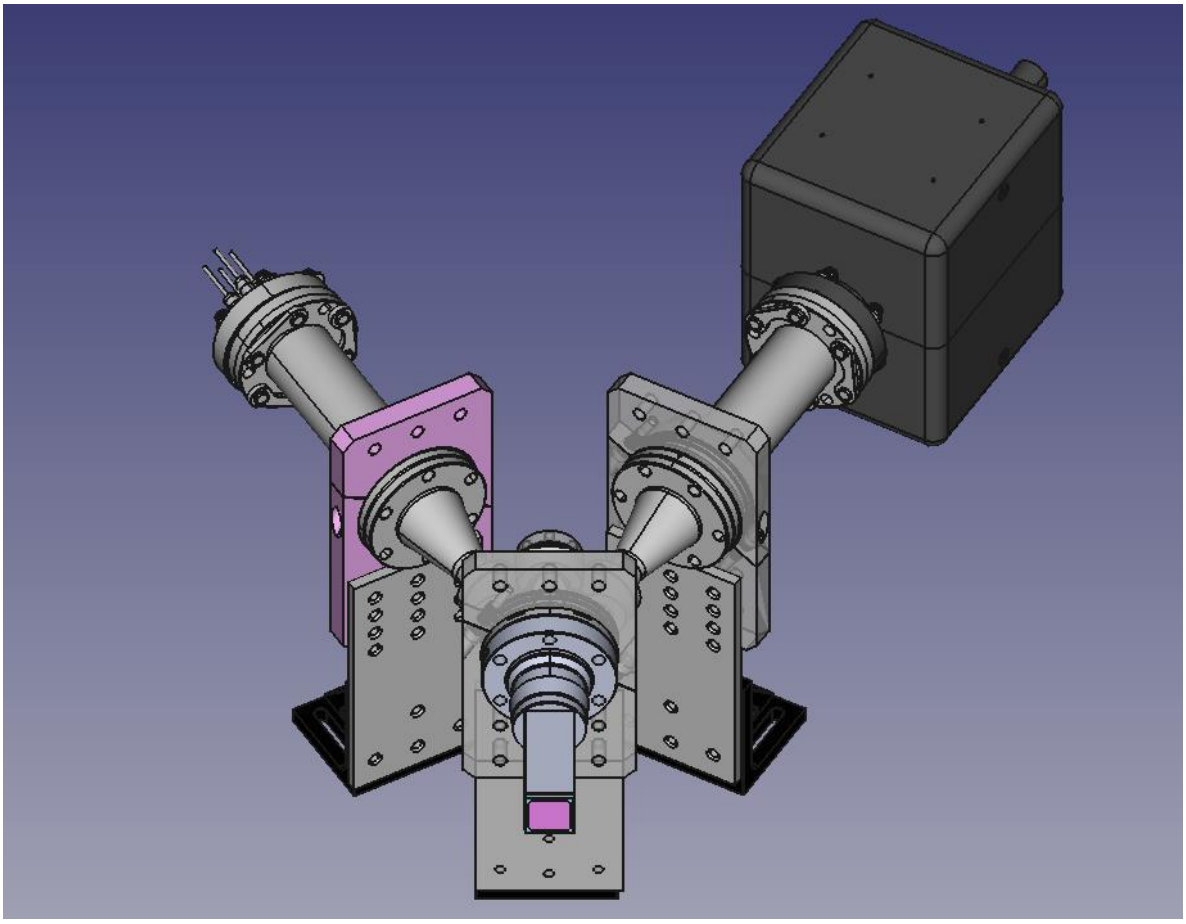

Figure 4-2 3D model of the vacuum system layout consisting of the vacuum glass cell, Conflat flanges, tubes and cone adapters, flange multiplexer, vacuum feedthrough and ion pump.

4.3.2 Optical system

4.3.2.1 Cooling and state preparation laser

The cooling laser drives the cycling transition $F = 2 \rightarrow F' = 3$ while state preparation in our atomic interferometry requires $F = 2 \rightarrow F' = 2$ transition. In addition, sub Doppler (red molasses) cooling requires agility in frequency and intensity control for the trapping beam. Figure 4.2 illustrates the optical setup of the cooling and state preparation beam. A 780 nm DBR laser (Photodigm PH780DBR180TS) provides >100 mW output power that diverges in free space (FWHM: $\theta_{\perp} \times \theta_{\parallel} = 6° \times 28°$). The laser beam is collimated with an aspheric lens (Thorlabs C230TMD-B) and a pair of cylindrical plano-convex lenses (Thorlabs LJ1695RM-B and LJ1653RM-B) with a focal length of 50 mm and 200 mm. The laser then goes through a combination of half-wave plate and PBS where 1.4 mW of power is directed into a home-built saturated absorption spectroscopy setup that generates the error signal required for frequency locking. The laser is locked to the crossover transition $F = 2 \rightarrow F' = 1,3$ which is about 211.8 MHz red detuned from the cycling transition. The rest of the laser power is split again, where ~10

mW goes into an acousto-optic modulator (AOM, Gooch&Housego 3080-122). The AOM is operating at 54.85MHz so that the -1 diffraction order from the output is resonant with $F = 2 \rightarrow F' = 2$ transition, which is then coupled to a PM fiber and directed to the vacuum cell for state preparation. Meanwhile, the remaining 60 mW power is sent through a double-pass AOM (Gooch&Housego 3100-125) system (ref) that provides the necessary red detuning from the cycling transition for normal MOT operation (6-18 MHz) as well as sub-Doppler cooling (> 48 MHz) by simply adjusting the AOM operating frequency. Finally, the light is amplified through a fiber-based booster optical amplifier (Thorlabs BOA785S) that provides up to 80 mW single mode fiber-coupled power. The cat's eye retroreflector configuration in the double-pass AOM apparatus ensures a relatively high fiber coupling efficiency across the whole AOM operating frequency range, leading to a wider parameter space (red detuning & intensity) for the cooling laser.

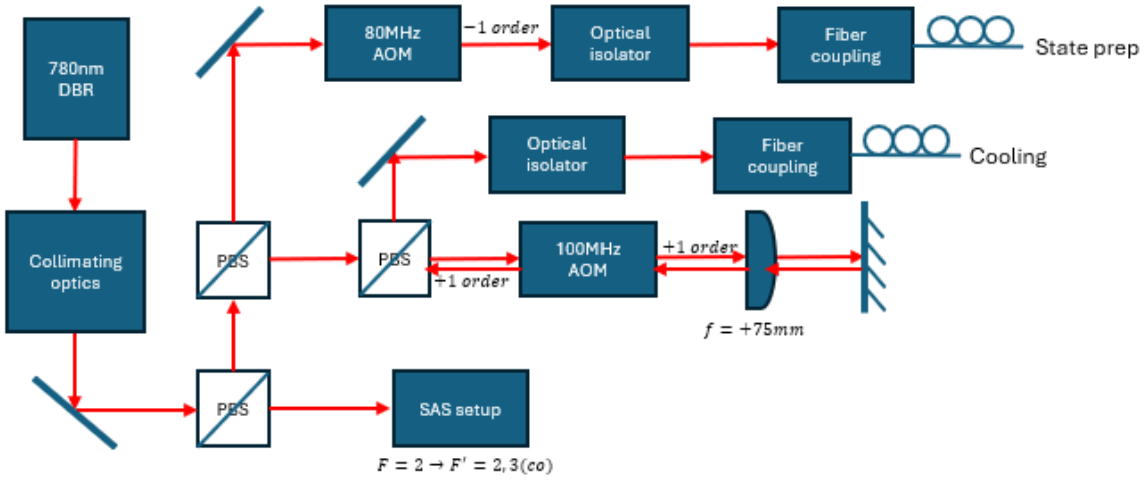

Figure 4-3 Schematic of the optical setup for the cooling & state preparation laser.

The cooling beam is expanded to 7.5 mm in diameter through an air-spaced doublet collimator (Thorlabs F810APC-780) and launched through a combination of wave plates and PBS for polarization cleaning and power control. Then the beam is split into three branches with equal intensity and directed into the geometrical center of the vacuum cell along three orthogonal directions to form the 3D MOT. For each direction, a quarter-wave plate sets the correct handedness of the circular polarization and the laser is retroflected through a quarter waveplate to form the $\sigma^+ - \sigma^-$ polarization configuration in combination with the magnetic field for trapping.

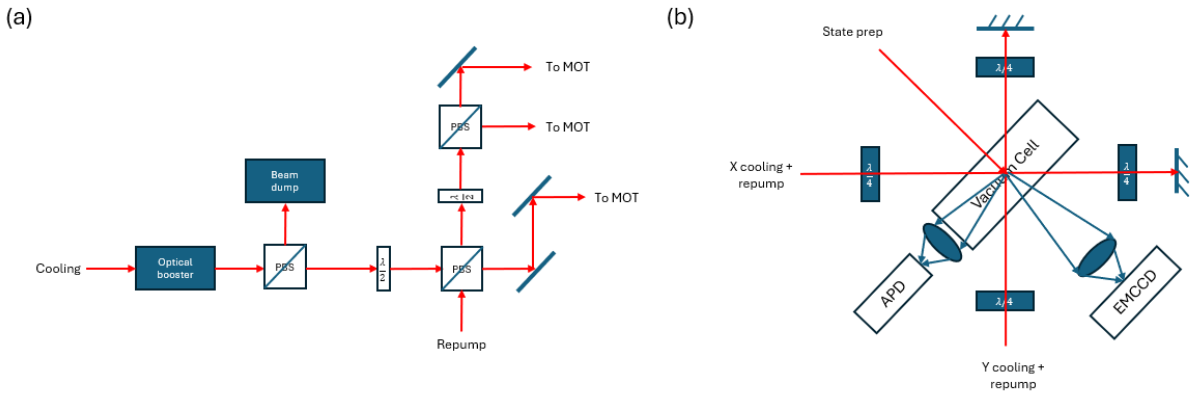

Figure 4-4 (a) Schematic of beam splitting, combing and delivery in free space to the vacuum cell; (b) Top view schematic of the optical setup around the vacuum cell for atom trapping, imaging and state detection.

4.3.2.2 Repump laser

In order to drive the cooling transition continuously, a repump laser is needed to pump the atoms out of the $F = 1$ manifold that is inaccessible for the MOT laser. The setup of the repump laser is shown in Figure 4.4. A 795nm DBR laser (Photodigm PH795DBR180TS) with > 100 mW output power in free space is collimated by an aspheric lens (Thorlabs) and a pair of cylindrical lenses with focal lengths of 50 mm and 150 mm. After beam shaping, ~ 1 mW laser power goes to a saturated absorption spectroscopy setup to keep the laser locked to the $F = 1 \rightarrow F' = 2$ transition. The remaining laser power is directed through two acousto-optic modulators (Gooch&Housego 3150) with an operating frequency of 150 MHz. To keep the repump laser resonant with the atomic transition, we select the +1 diffraction order for the first AOM and -1 for the second. After that, the beam passes through an optical isolator before getting coupled into a PM fiber, where it is launched with a fiber collimator and then combined with the cooling beam through a PBS.

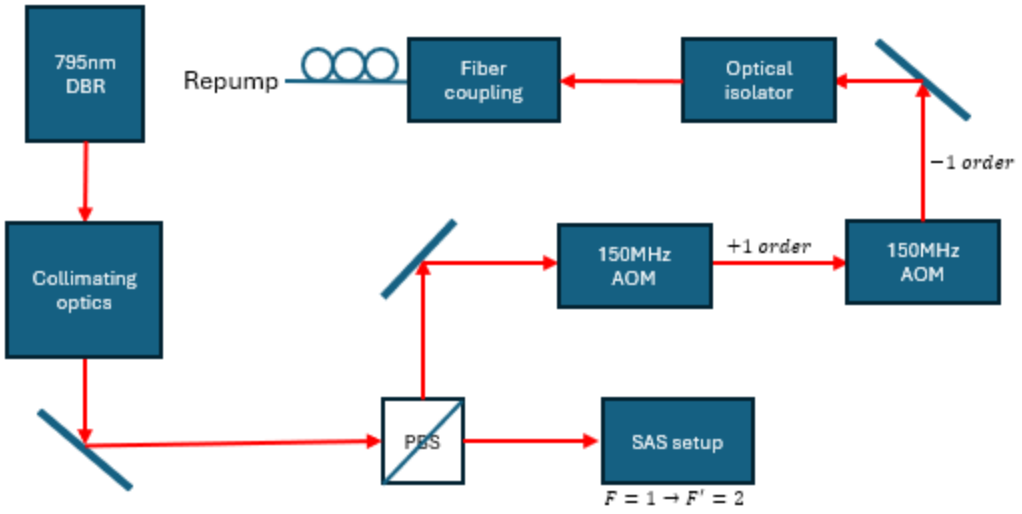

Figure 4-5 Schematic of the optical setup for the repump laser.

4.3.2.3 Raman beam generation

Raman beams are essential in our light pulse atomic interferometry for manipulating the momentum and internal state of the atoms. Figure 4.5 shows the optical setup in generating the Raman pulses. A 780nm DBR laser (Photodigm PH780DBR180TS) (~ 70 mW in free space) is collimated by a combination of aspheric and cylindrical lenses and split by a polarizing beam splitter. About 5 mW of power is coupled into a PM fiber and delivered to the trapping laser setup, where it is mixed with part of the trapping beam to form an optical beat note. This beat note is picked up by a multimode ultrafast detector (12 GHz bandwidth) and fed into an offset phase lock servo (Vescent D2-135), which enables a fixed, tunable frequency offset between the trapping and Raman laser. This is useful for optimizing the interferometry contrast. The remaining power of the laser is coupled into a fiber-based electro-optical phase modulator (ixblue NIR-MPX800-LN-10-00-P-P-FA-FA) to generate the sideband necessary for driving the Raman transition. The phase-modulated output of the EOM is then amplified by a homebuilt (Kangara, et al., 2014) tapered amplifier module (Toptica Eagleyard EYP-TPA-0780-03000-4006-CMT04-0000) that easily generates >3W optical power in free space. After collimation and beam shaping to reduce the diameter of the beam to 1 mm, the amplified beam is sent through an AOM (Gooch&Housego 3150) to serve as an optical switch for the light with a diffraction efficiency of 80% to the first order. The laser is finally coupled into a PM fiber for optical power delivery into the vacuum cell. To ensure that the high power reflection from the TA does not interfere with the offset phase lock signal, both input and output side of the TA is properly protected by high-power optical isolators (Edmund Optics 35-983).

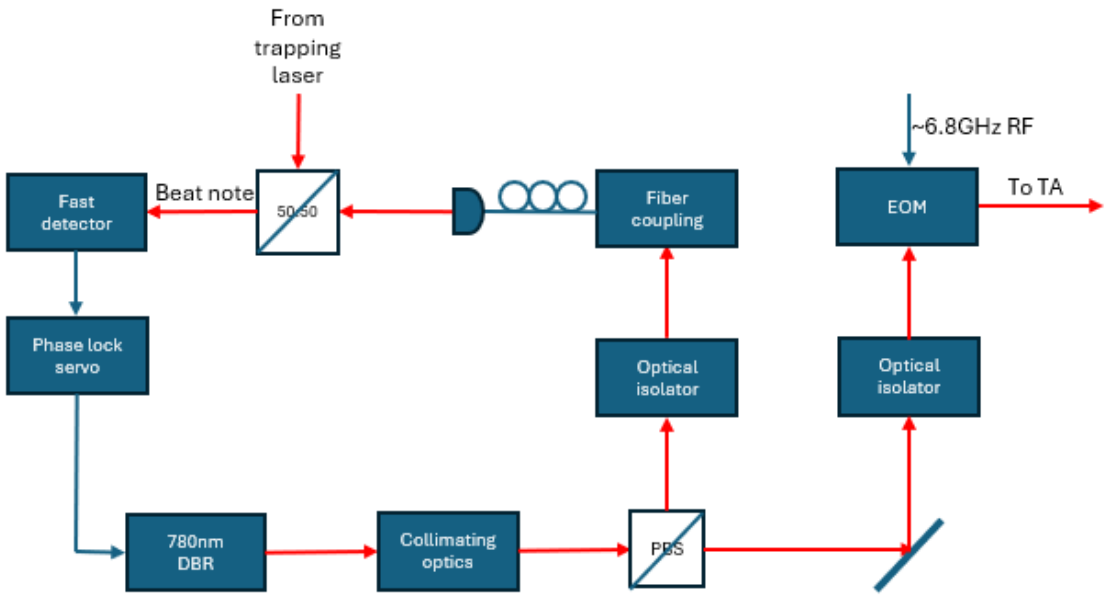

Figure 4-6 Schematic of the optical setup for the Raman laser.

Thanks to the high power output from the TA, we can obtain $> 400\ mW$ fiber-coupled Raman laser power with few optical alignment adjustment and optimization. The Raman beam is collimated to a diameter of 5.42 mm with a triplet fiber optic collimator (Thorlabs TC25APC-780). The superior design of the collimator ensures a very high beam quality with M^2 close to 1.

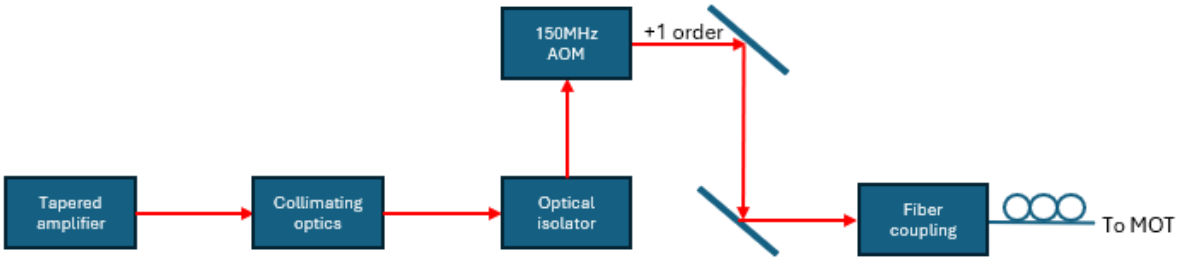

Figure 4-7 Schematic of the optical setup for amplifying and switching the Raman laser.

The Raman beam is mixed with the trapping beam along the z direction for sensitivity along the gravitational axis. A temperature-stabilized liquid crystal waveplate (Thorlabs LCC1111T-B) switches the polarization configuration between atom cooling ($\sigma^+ - \sigma^-$) and Doppler sensitive Raman interrogation ($lin \perp lin$) with sub-millisecond speed (See Appendix A9).

We note that sidebands produced by the EOM could form multiple Raman pairs. Ignoring higher order sidebands, the -1 order with frequency $\omega - \omega_{mod}$ and the carrier can also excite Raman transition if ω_{mod} is close to the hyperfine splitting. However, the effective Rabi frequency of this pair is lowered by a factor of $\frac{\Delta}{\Delta+\omega_{HF}} \ll 1$.

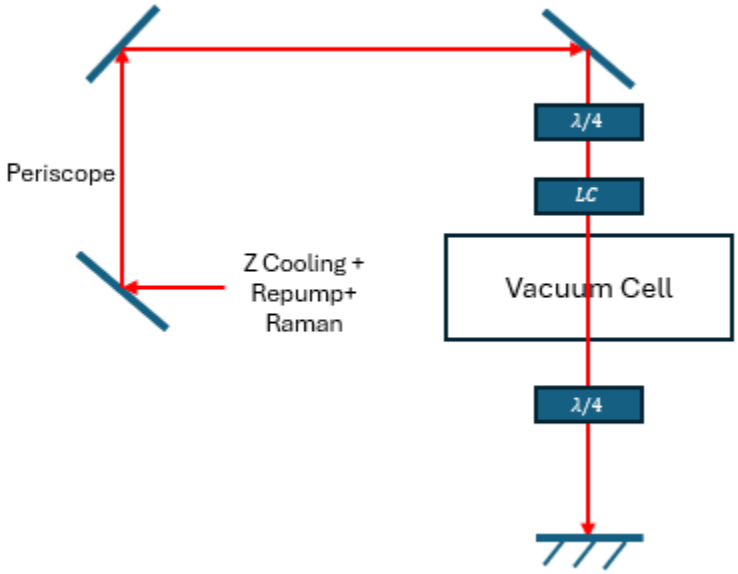

Figure 4-8 Raman beam delivery in free space. The Raman beam is mixed with the cooling and repump beam along the z direction via a PBS. The liquid crystal (LC) waveplate is capable of switching the polarization configuration between cooling and Raman interrogation.

4.3.2.4 Detection system

The detection system is responsible for characterization and readout of the system information, both classical and quantum, by detecting the fluorescence emitted from the atoms. The detection system consists of an electron multiplication CCD (EMCCD) camera (Andor ixon 897) and a free space avalanche photodetector (APD) (Thorlabs APD440A) (see Figure 4.3a). The EMCCD camera is a widefield characterization tool capable of achieving single photon sensitivity on individual pixels. However, it is hard to obtain quantified information on the light intensity across

a large number of pixels. Therefore, it is mainly used for applications where the spatial information is important, such as quick characterization on the position, intensity and shape of the MOT and TOF-based atom temperature measurement.

Meanwhile, the APD simply collects the atom fluorescence and converts it into a voltage signal. While it cannot provide spatial information directly, it can be placed closer to the trapped atoms due to its compact size, yielding a much higher photon collection efficiency. The linear conversion between the output voltage and incident optical power ensures the interoperability of the quantified measurement. Therefore, it is used for measuring the atom number and the internal state of the atomic ensemble.

4.3.3 Electronics system

The experiment is controlled by Artiq (Advanced Real-Time Infrastructure for Quantum physics), which uses a high-level programming language (Python) to control the dedicated FPGA hardware with nanosecond timing resolution and sub-microsecond latency. The hardware includes a FPGA carrier (Kasli) that controls the subsequent extension modules, two 8-channel TTL cards (Sinara 2128) that triggers the events on experiment instruments (RF switches, liquid crystal controller, camera, frequency tuning and general timings), one 16-bit DAC (Zotino) for low frequency arbitrary waveform generation (mainly for tuning the variable voltage attenuator controlling the RF amplitude sent to the AOMs) and two direct digital synthesizers (Urukul DDS 4410 & 4412) for generating agile RF waveforms (for AOMs and EOM).

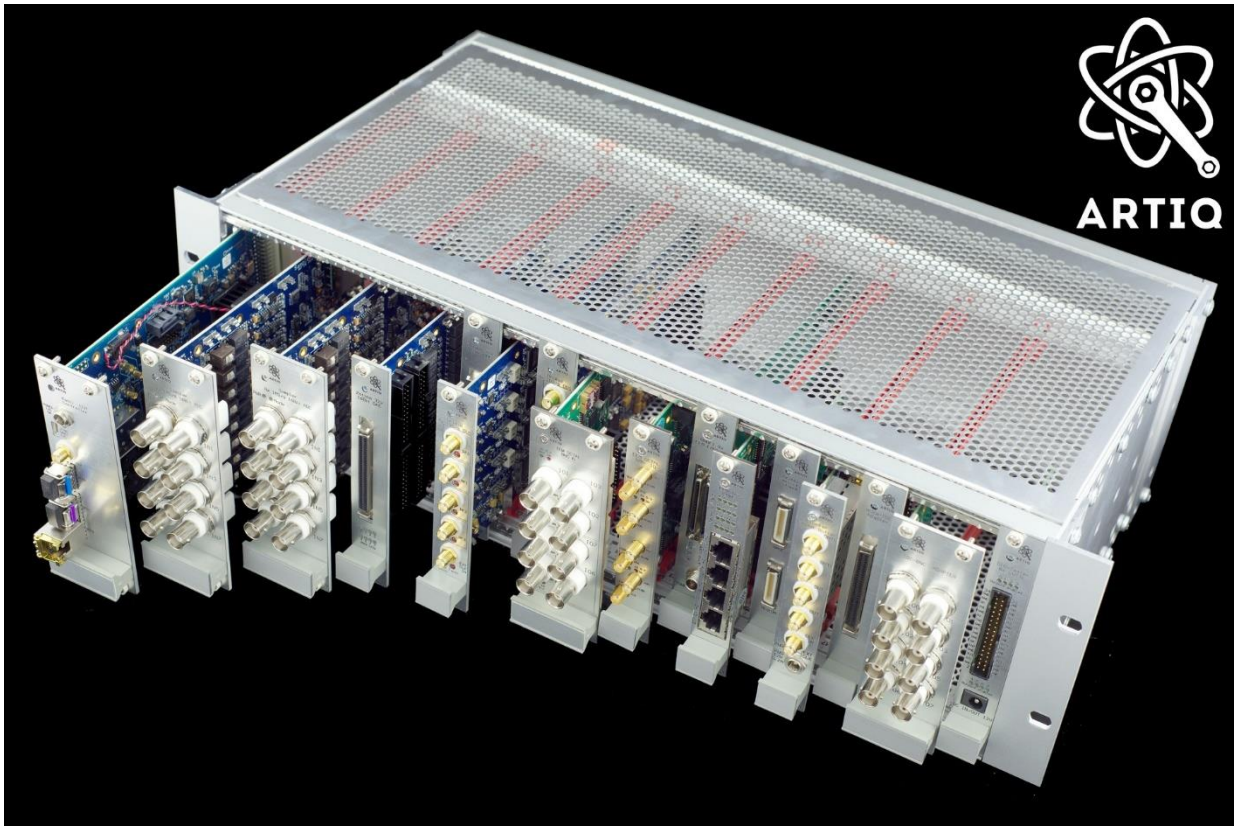

Figure 4-9 The Artiq Sinara hardware, consisting of a chassis, a FPGA controller and multiple extension modules. Adopted from https://m-labs.hk/experiment-control/artiq/.

To generate the $\sim 6.834\ GHz$ RF signal for generation of Raman sidebands with frequency and phase agility, we mix the output from a 6.8 GHz ultra-low noise phase-locked DRO oscillator (Microwave Dynamics PLO-2000) with a $\sim 30\ MHz$ output from the DDS, which offers controlled frequency sweeps and phase steps. We use single sideband mixer (Polyphase SSB3570A) with 34 dB sideband suppression to ensure the frequency purity from the output. The mixed signal is being amplified by a low-noise RF amplifier (Minicircuit) to drive the EOM. A directional coupler (Minicircuit) samples a small amount of RF power (-10 dB) to ensure the amplitude stability while running the experiment. Finally, the oscillator and two DDSs share a common 100 MHz reference from a crystal oscillator (Wenzel 500-07078).

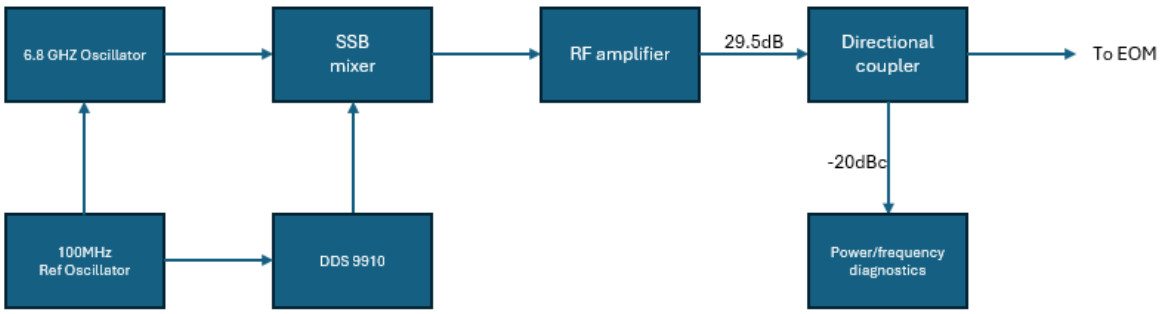

Figure 4-10 Diagram of the circuit for generating the microwave frequencies for the Raman EOM signals. The single sideband mixer adds the base 6.8 GHz signal (Microwave Dynamics PLO-2000) with the dynamic signal from the DDS (Urukul 9910), providing frequency sweeping and phase shifting capabilities.

4.4 Magneto-optical trap

The interferometry experiment starts by loading Rb atoms from thermal vapors into a MOT. For most cold atom experiments, MOT is the workhorse for cooling and confining a large population of atoms from thermal backgrounds and serves as the platform for the subsequent advanced cooling and trapping procedures.

The physics principle behind MOT is Doppler cooling. An atom moving with a velocity $\boldsymbol{v}$ and inside a laser field with wavevector $\boldsymbol{k}$ and frequency ω_L will experience a shifted laser frequency:

$$\omega_L' = \omega_L - \boldsymbol{k} \cdot \boldsymbol{v} \tag{4.21}$$

Consider the situation where the laser is near-resonant and red detuned: $\omega_0 - \omega_L = \delta > 0$. In (Cohen-Tannoudji, Dupont-Roc, & Grynberg, 1998) the (dissipative) force exerted on the atom is given by:

$$F = \hbar \boldsymbol{k} \frac{\Gamma}{2} \frac{\frac{\Omega^2}{2}}{(\delta + \boldsymbol{k} \cdot \boldsymbol{v})^2 + \frac{\Gamma^2}{4} + \frac{\Omega^2}{2}} \tag{4.22}$$

where Γ is the natural linewidth and Ω is the Rabi frequency. In our MOT setup, a pair of anti-Helmholtz coil provides a quadrupole field with a constant gradient at the center. Combined with the $\sigma^+ - \sigma^-$ polarization configuration, this gives an optical force (in 1D) (Patel, 2009):

$$F = \hbar k \frac{\Gamma}{2}\left[\frac{\frac{\Omega^2}{2}}{\left(\delta + \boldsymbol{k}\cdot\boldsymbol{v} - \frac{\mu_B g B(\boldsymbol{r})}{\hbar}\right)^2 + \frac{\Gamma^2}{4} + \frac{\Omega^2}{2}} - \frac{\frac{\Omega^2}{2}}{\left(\delta - \boldsymbol{k}\cdot\boldsymbol{v} + \frac{\mu_B g B(\boldsymbol{r})}{\hbar}\right)^2 + \frac{\Gamma^2}{4} + \frac{\Omega^2}{2}}\right] \quad (4.23)$$

Here, μ_B is the Bohr magneton, g is the Landé g factor of the involved atomic states, $B(r)$ is the magnetic field.

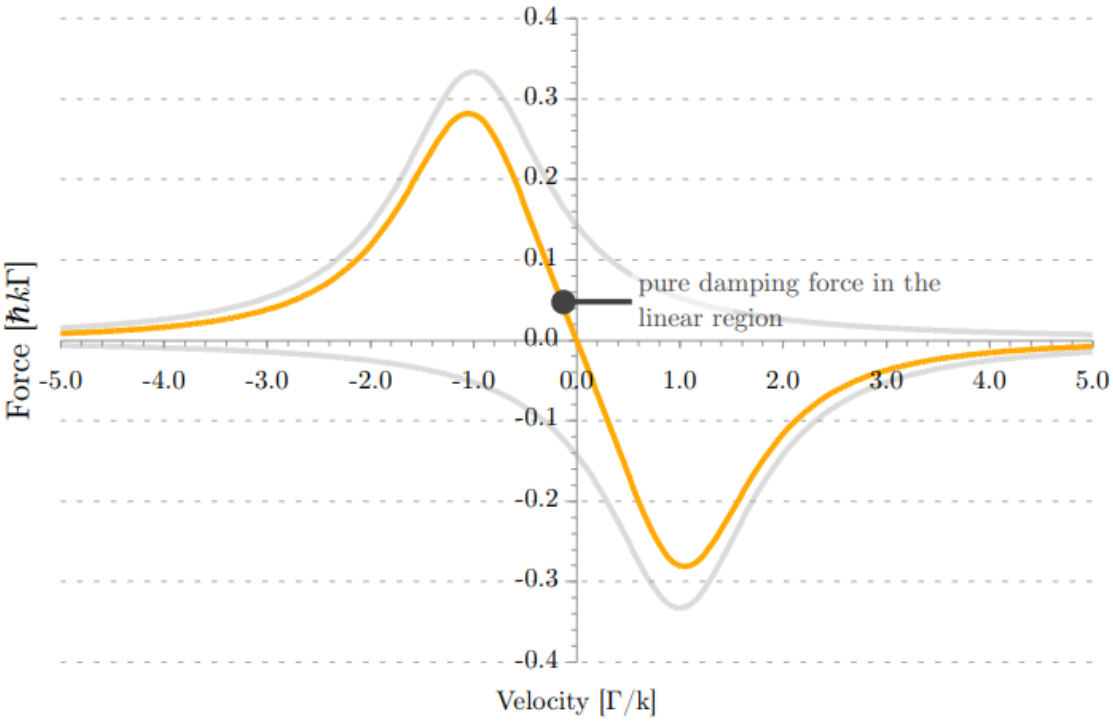

Figure 4-11 Optical force in a 1D molasses. Adopted from (Patel, 2009).

In the experiment, we form our MOT by operating the atomic source at 4.2 A, which allows for daily operation of nearly a year without depleting. The trapping beam has an optical power of 12 mW for each branch, corresponding to an intensity of 27 mW/cm^2. The total repump power is 2.7 mW, or around 7% of the trapping power. The anti-Helmoltz coil is operated at 3.8A, which corresponds to a field gradient of 17 G/cm at the center of the vacuum cell.

The characterization of the MOT is done through fluorescence imaging via the EMCCD camera. Figure 4.9 shows the captured image of the MOT at the steady state, with its size (x: 426 μm y: 370 μm) extracted through Gaussian fitting.

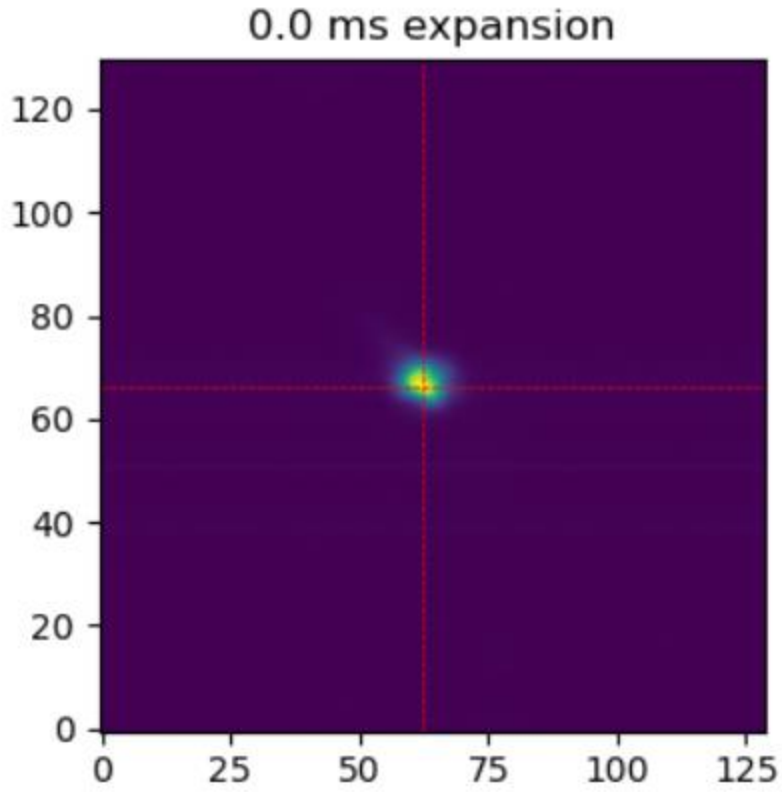

Figure 4-12 Image of the MOT at a steady state. The algorithm finds the brightest spot in the captured image and treats it as the center of the MOT for fitting its size.

For temperature characterization, we use time-of-flight (TOF) measurement, where the atom cloud is allowed to expand in darkness for a duration of τ. After expansion, the atoms are flashed with the trapping beam for $500\ \mu s$ to for fluorescence imaging without significantly disturbing the free expansion dynamics. The expanded image is fitted again to extract the cloud size $\sigma_{x,y}(\tau)$, and the temperature along the two axes extracted by fitting the formula

$$\sigma_{x,y}{}^2(\tau) - \sigma_{x,y}{}^2(0) = \frac{k_B T_{x,y}}{M} \tag{4.24}$$

For our MOT, we measured temperature of $T_x = 211.4\ \mu K$, $T_y = 157.6\ \mu K$, which generally agrees with the Doppler limit. The elevated temperature can be attributed to the relatively high optical power used for trapping, which causes intensive scattering and can lead to heating up atoms. Indeed, we observe a lower atom temperature when the trapping power is reduced to 6 mW per branch, albeit with less trapped atoms.

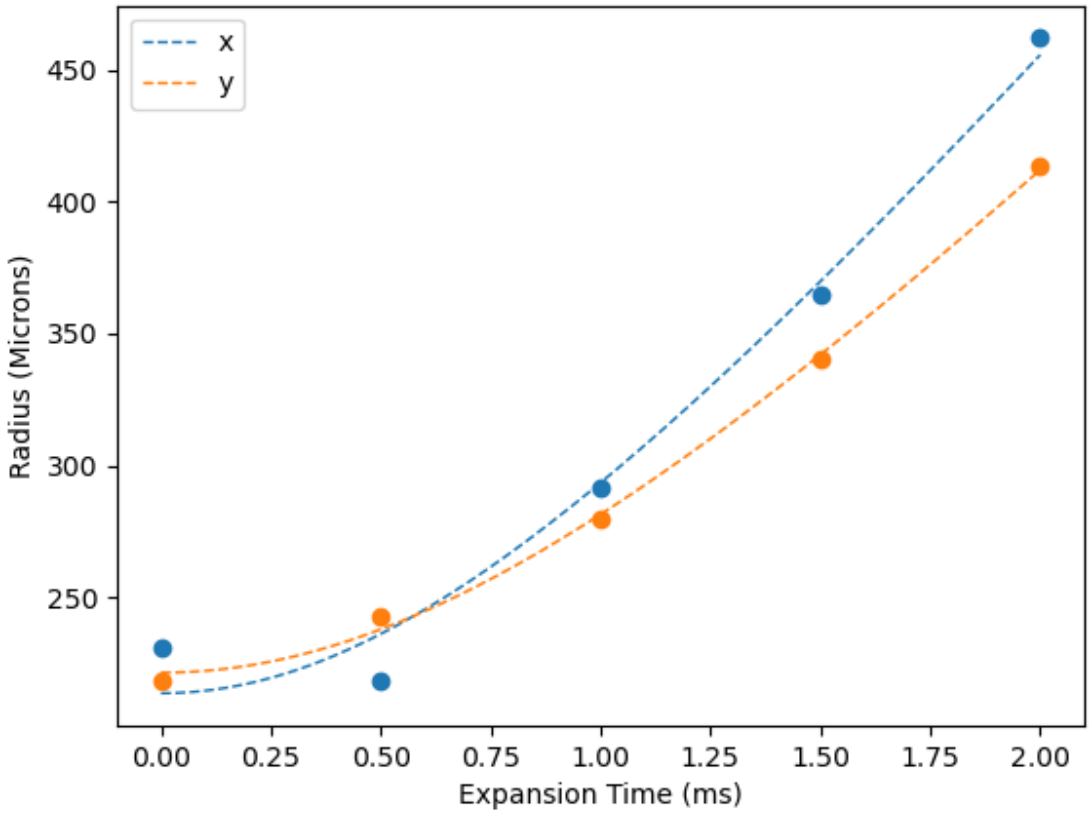

Figure 4-13 Obtaining the atom temperature through fitting the size of the expanding atom clouds. The difference between temperature along x and y direction is likely attributed to the imbalanced optical force and asymmetric magnetic field profile.

4.5 Sub-Doppler (Molasses) cooling

Depending on the experiment conditions like laser intensity, frequency detuning and magnetic field gradient, the temperature of our MOT are typically within the range of 100 – 200 μK, limited by the Doppler temperature $T_D = \frac{\hbar\gamma}{2k_B} = 146\,\mu K$. For cold atom interferometry, a colder atom ensemble is generally required, as higher temperature of the ensemble contributes to dephasing through increased Doppler broadening during the interferometry sequence.

Interestingly, not long after the Doppler cooling mechanism was proposed, Lett (Lett, et al., 1988) observed laser cooled sodium atoms reaching temperatures well below the Doppler limit. This and the subsequent similar observations prompted Dalibard and Cohen-Tannoudji (Dalibard & Cohen-Tannoudji, 1989) to develop theory of polarization gradient cooling (PGC) to explain the sub-doppler cooling behavior. They considered two different configurations that form polarization gradient: counter propagating circular polarized lights with opposite handedness

($\sigma^+ - \sigma^-$) and counter propagating lights with orthogonal linear polarization ($lin \perp lin$). While both involve the interplay between laser polarization and atomic magnetic sublevels and lead to the same cooling limit (recoil limit), the physics mechanisms behind are very different. For simplicity, we use the MOT laser beams for PGC and only introduce the cooling mechanism for the $\sigma^+ - \sigma^-$ configuration.

The superposition of counter propagating σ^+ and σ^- light leads to a field distribution of:

$$E_{tot} = Ee^{-i\omega t}(\sin(kz)\,\hat{x} + \cos(kz)\,\hat{y}) \tag{4.25}$$

i.e a linearly polarized light with the polarization angle rotating along $\hat{z}$ with a spatial periodicity of $\frac{\pi}{k}$.

Dalibard and Cohen-Tannoudji considered a simple $F = 1 \rightarrow F' = 2$ transition and 1D molasses model. Consider atoms at $z = 0$ (or equivalently, any point along $\hat{z}$) and set the quantization axis along $\hat{y}$, the local polarization direction. The π transition causes atomic population to accumulate more in $|m_F = 0\rangle_y$. Moreover, the ground state light shift $\Delta E \propto \frac{\left|\langle F' m_{F'}|F\ 1\ m_F\ q\rangle\right|^2}{\Delta}$ where Δ is the detuning, which means $\Delta_0' = \Delta E(m_F = \pm 1) = \frac{3}{4}\Delta E(m_F = 0) < 0$ for red-detuned MOT beams. Now consider an atom moving in the $\hat{z}$ direction with speed v: it will see the local polarization rotating at frequency kv. If we choose a rotating frame such that the polarization remains along $\hat{y}$, then an inertial term $H' = kvF_z$ must be added to the Hamiltonian. As long as $v \neq 0$, this term introduces mixing in the y eigenstates. It can be shown (assuming that the ground state relaxation rate $\Gamma' \ll |\Delta_0'|$ and also $kv \ll |\Delta_0'|$) that under this perturbation, unlike in the y basis, the atoms become oriented along $\hat{z}$: $\langle F_z\rangle = \frac{40\hbar kv}{17\Delta_0'}$. Therefore, when $v > 0$, $\langle F_z\rangle < 0$, and atoms are more likely to absorb σ^- photons moving towards negative z and vice versa, creating a damping force for atom cooling. PGC surpasses the limit imposed by Doppler mechanism and the ultimate achievable temperature is bounded by the one-photon recoil limit:

$$T_{rec} = \frac{\hbar^2 k^2}{2k_B M} \tag{4.26}$$

Our first attempt at polarization gradient cooling follows schematics shown in Figure 4.11. After loading the MOT from background vapor for ~ 2s with a cooling beam detuning of ~ -3Γ, the anti-helmholtz coil is rapidly switched off, while the cooling laser detuning is linearly ramped up to -8Γ and its intensity decreased to 10% in 5 ms. Meanwhile, the repump laser stays on for the whole sub-doppler cooling process without changing its intensity or frequency and remains on for an extra 1 ms to prepare the atoms in the $F = 2$ manifold (it was found later that stepping down the intensity of the repump in this case did not lead to improved cooling). To characterize the temperature of the molasses after PGC, the same cooling beam (with the same intensity and

detuning of the normal MOT) is flashed for 500 μs to induce fluorescence for imaging without significantly perturbing the atoms, and the temperature is again calculated by TOF method.

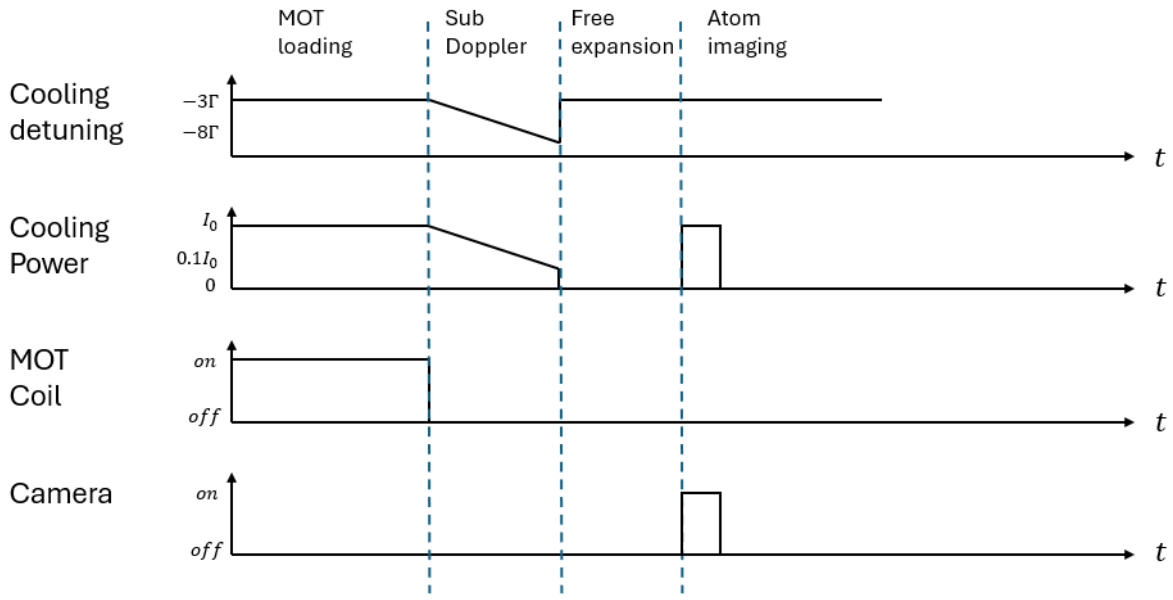

Figure 4-14 Schematics of our PGC Sub-doppler cooling sequence. The cooling start with loading the MOT from background vapor, followed by a 5 ms sub-doppler cooling procedure where the red detuning of the MOT laser increases to ~48 MHz and its intensity decreases to 10% of the initial power. Repump stays on while MOT coil shuts down during sub-doppler cooling. The same cooling beam is used to flash the atom to generate fluorescence collected by an EMCCD camera.

Figure 4.12 shows the temperature fitting after the PGC sequence. For both x and y directions, the atoms experience significant cooling, with temperatures decreasing to $47.85\mu K$ for x and $36.47\mu K$ for y. In the experiment, we also observed that atoms were moving upright during the sub-doppler cooling process, which was a sign of uncompensated stray magnetic field. This also explains why the temperature obtained after PGC is significantly higher than the recoil limit (0.36 μK), as PGC works best when the field is properly cancelled (Rosi, et al., 2018).

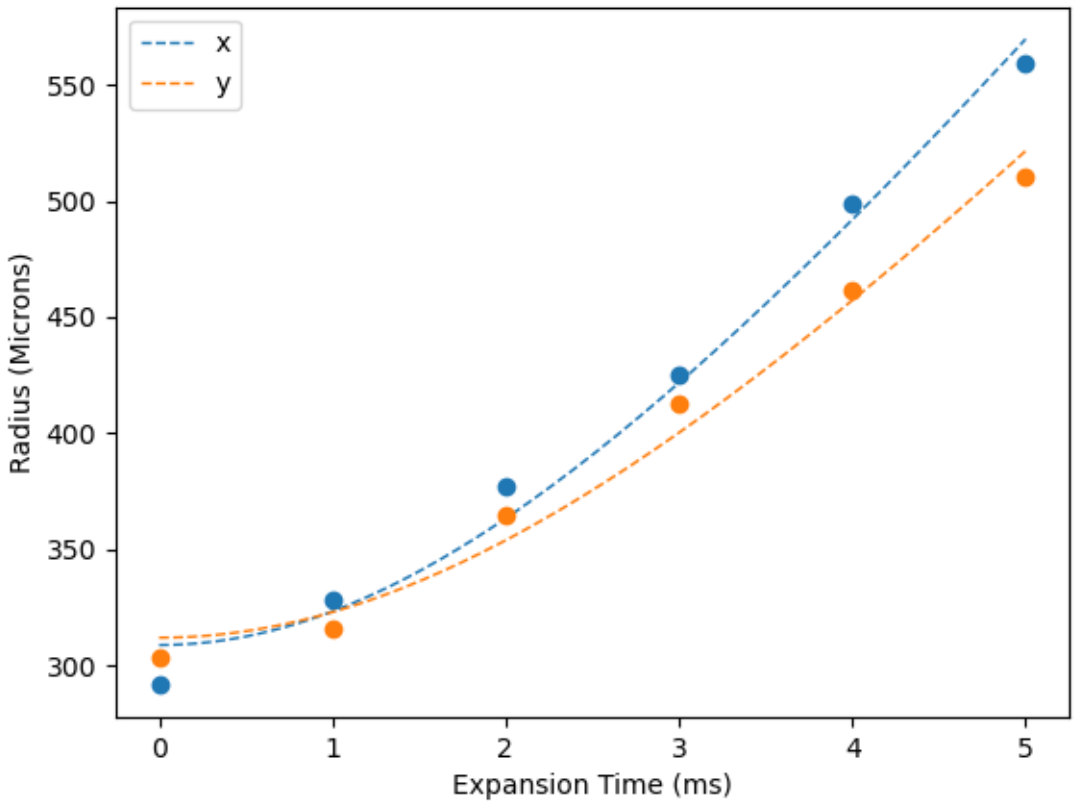

Figure 4-15 Temperature fitting for sub-doppler cooled atom cloud without stray field compensation.

For an improved sub-doppler cooling performance, ideally the system should be properly shielded from the surrounding magnetic field, although this is sometimes unnecessary for well-controlled lab environments and gravimeters with a short interrogation time. For now, we installed shim coils to cancel part of the stray fields at the center after the MOT coils are switched off. We observed lower atom temperatures ($T = 18\,\mu K$) when the shim coil along the z direction is operating at 0.4 A. However, the temperature fitting program fails to produce a meaningful fit for the expansion cloud figures when the shimming field is added, which is likely due to the distortion of the MOT cloud with the asymmetric field profile generated by the small shim coils. We therefore conclude that in order to effectively null the stray field without disturbing the atom ensemble, larger coils that adhere to Helmholtz condition $r = d$ are needed to produce a uniform shimming field at the position of the cold atom ensemble. Here r is the radius of the coil and d is the coil separation.

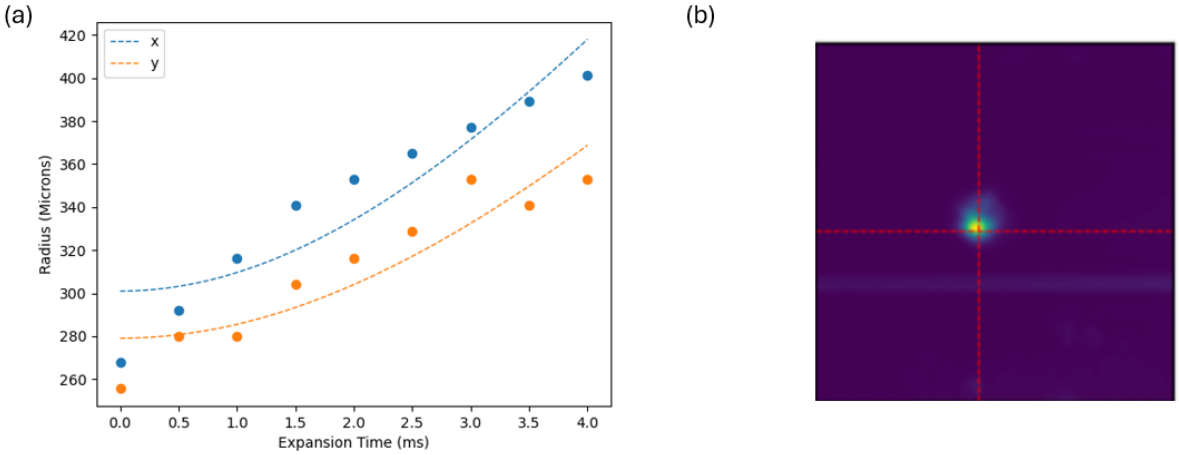

Figure 4-16 (a) Temperature fitting for sub-doppler cooled atom cloud with the z-shim coil running at 0.4A; (b) EMCCD image of the MOT under the z shimming field, showing its distorted shape, which is likely a result of inhomogeneous field from the shim coil.

4.6 State preparation

Atomic interferometry is generally sensitive to magnetic fields. As atoms move in space during the interrogation sequence, magnetic field variation could cause a time-dependent shift in their energy levels and lead to dephasing. Therefore, it is necessary to prepare the atoms in the magnetic-insensitive state $|F, m_F = 0\rangle$ before the interferometry sequence starts.

To accomplish this task, the following steps will be implemented in future experimental work. A bias magnetic field B_z under $1G$ will be applied to establish a quantization axis along the z-axis. This bias field will allow us to define a well-controlled energy level structure for the atoms, aiding in efficient state preparation. The state preparation laser resonant with the $F = 2 \rightarrow F' = 2$ transition is directed to the trapped atoms by a polarization maintaining fiber and collimated to a diameter of 5.42 mm ($1/e^2$) using the triplet fiber optic collimator (Thorlabs TC25APC-780) for a high beam quality. This state preparation laser could also be mixed with the horizontal (x or y) cooling beam with a 50-50 beam splitter to save one optical access for camera imaging. To drive π transitions in the atoms, the laser polarization will be aligned along the z-axis using a high extinction ratio linear polarizer (e.g., Thorlabs LPVIS). This will help suppress the spurious σ transitions and help accumulate atoms into the desired magnetic-insensitive state. Meanwhile, the repump laser stays on during the state preparation stage to pump the atoms out of the ground state $F = 1$ manifold so that the $F = 2 \rightarrow F' = 2$ transition is driven continuously. Since the selection rule forbids an electric dipole transition with $\Delta F = 0$ and $\Delta m_F = 0$, the atoms will accumulate in state $|F = 2, m_F = 0\rangle$ after sufficiently many cycles of optical pumping. We estimate that the state preparation process will only take a few hundred microseconds (Butts, 2011). This process will slightly heat up the atom through scattering of photons but will drastically improve the contrast of

the interference fringes and lead to a more sensitive gravity field measurement. Alternatively, a doppler-sensitive Raman transition can help selecting a atomic ensemble near recoil temperature, but at the cost of losing the available amount of atoms being interrogated (Butts, 2011; Dunning, 2015).

4.7 Interferometry sequence and state detection

We will use the standard $\frac{\pi}{2} - \pi - \frac{\pi}{2}$ interferometer to measure gravitational acceleration g. The Raman laser will be red or blue detuned from the $F = 2 \rightarrow F' = 2, 3(co)$ transition by $\Delta > 1\ GHz$ for a balance between the two-photon Rabi frequency and spontaneous emission rate. We linearly ramp the Raman detuning δ at rate $\alpha = k_{eff} g \approx 2\pi \times 25.1\ kHz/ms$ to ensure a resonant Raman condition as the atoms experience Doppler shift during free fall.

To generate interference fringes, according to equation (4.20), we fix the phase of the first $\frac{\pi}{2}$ and π pulses while scanning the phase of the second $\frac{\pi}{2}$ pulse. Since $|k_{eff}|$ is a large number, the interferometry experiment should begin with small dropping times T (ideally sub millisecond) to ensure a correct fringe count. The frequency chirp rate α can then be determined by making the phase shift invariant with respect to T.

Equation (4.20) does not account for the systematic phase shift arising from the different light shift of the $F = 1$ and $F = 2$ energy levels. From the expression of Ω_s^{AC} in section 4.2, we know it is possible to cancel this phase shift if we carefully tune intensity ratio of the two frequency components in the Raman field, which is in turn determined by the RF amplitude injected into the EOM. In (Butts, 2011), the author proposed using a microwave Ramsey interferometry to determine and cancel this phase shift. In the microwave interferometry, the Raman pulse is injected between the two $\frac{\pi}{2}$ microwave pulses, and the Ramsey sequence can readout this phase shift caused by atomic state evolution under the light shift caused by the Raman pulse. To suppress the state transfer by Raman transition, the Raman detuning δ is set to several MHz. The light shift, however, remains largely unchanged compared to the normal Raman pulses used in atomic interferometry sequence. The light shift phase is then canceled when the phase shift measured by the Ramsey interferometer is invariant with respect to different Raman pulse length. However, if the Raman field intensity is stabilized across individual shots of the interferometry, this phase shift is a fixed term and won't degrade the sensitivity of the atomic interferometer. Therefore, it is important to suppress the intensity and frequency noise of the Raman laser and the RF source.

At the end of interferometry sequence, we will need to measure the state population to extract the phase difference ϕ between the two interferometer arms (assume the initial state is $|F = 1\rangle$):

$$P(F = 1) = \frac{1}{2} + \frac{C}{2} cos\phi \tag{4.27}$$

Here, $P(F=1)$ is the fraction of population measured in $F=1$, $C=\frac{P_{max}-P_{min}}{P_{max}+P_{min}}$ is the contrast where P_{max} and P_{min} are the maximum and minimum $F=1$ population fraction measured.

We plan to measure the population fractions in the two states used in the interferometry as detailed in (Butts, 2011):

1. Tune the cooling laser frequency with AOM to near resonant with the cycling transition $F=2 \rightarrow F=3$ and collect the fluorescence from atoms with APD. The APD voltage V_2 is related to the population in $F=2$;
2. Shift the frequency of the cooling laser to be blue detuned from $F=2 \rightarrow F=3$ transition and push atoms in state $|F=2\rangle$ out of the interrogation region;
3. A repump pulse places all the atoms in $F=2$ again;
4. Repeat process 1 to obtain the $F=1$ population signal V_1;
5. $P(F=1)=\frac{V_1}{V_1+V_2}$.

By individually measuring V_1 and V_2 and normalizing the signal with respect to their sum, the measurement is less sensitive to atom number variation from shot to shot. In (Butts, 2011), it is reported that the primary limiting factor of the detection SNR is the intensity and frequency fluctuations of the probe laser, which cause atomic fluorescence to vary from individual measurements. The author proposed spatially separate imaging with atoms launching by moving molasses or simultaneous absorption imaging with two detectors using biochromatic probe beam to determine both populations simultaneously as solutions. In addition, we can leverage the ultranarrow linewidth integrated laser source reported in (Isichenko, et al., 2024) as the probe beam to suppress the unwanted laser frequency noise. This laser source, which is a Fabry-Pérot diode coupled to an on-chip splitter and a tunable resonator, is realized in the CMOS foundry-compatible silicon nitride platform, which could prove valuable for our research effort towards a compact and robust cold atom gravimeter.

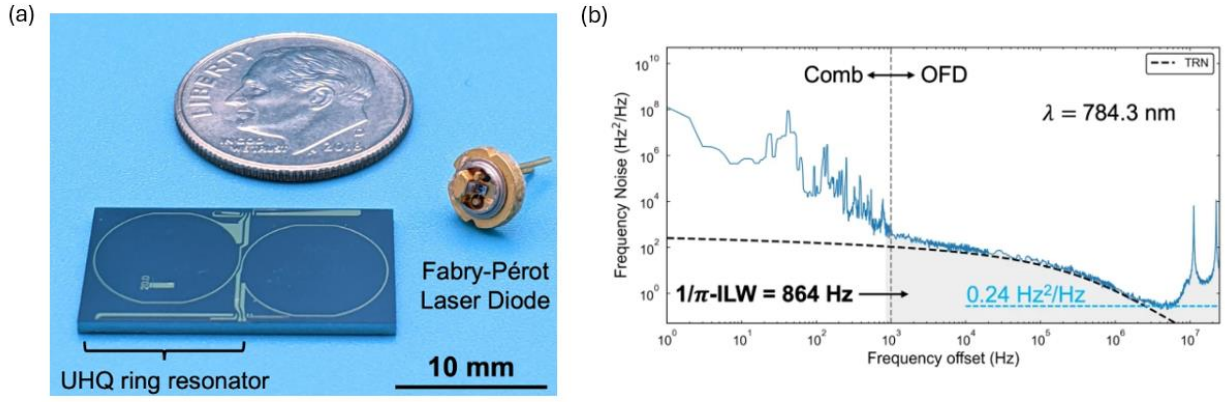

Figure 4-17 (a) Picture of integrated ultra-high-Q (UHQ) ring resonator and Fabry-Pérot laser diode (FPLD) composing the chip-scale ultra-narrow linewidth laser; (b) Frequency noise spectrum of the laser obtained with beat note measurement and optical frequency discriminator (OFD) showing a integrated linewidth of 864 Hz. (Isichenko, et al., 2024)

4.8 Progress on grating magneto-optical trap (GMOT)

As mentioned in the previous section, the core of every cold atom inertial sensor lies in the generation of magneto-optical traps that provide initial trapping and cooling of the atoms. Traditional six-beam MOT requires complex optical setups and frequent optical alignment procedures, which pose significant challenges for portability and scalability. For practical applications that demand compact, robust, and field-deployable gravimeters, these challenges must be addressed.

One promising approach is using a single diffraction grating to generate the laser beam configuration for the MOT. Unlike conventional MOT that needs multiple laser beams and elaborate optical arrangements, grating MOT (GMOT) requires only a single incident beam. This beam hits the grating to generate several reflected diffraction modes whose power and polarization are predesigned to form the necessary trapping configuration together with the incident beam. This reduction in optical complexity leads to a significant decrease in both the footprint and the power requirements of the setup, making GMOTs highly suitable for portable and integrated cold atom systems.

In this section, we describe the ongoing effort in incorporating the GMOT into our cold atom gravimetry system in collaboration with Kats research group. The diffraction grating design is adopted from (Nshii, et al., 2013) and (Yu, et al., 2024). As illustrated in Figure 4.15, the grating consists of three sets of linear patterns with 1.4 μm pitch size, 50% duty cycle and 210 nm in height. When the incident beam hits the linear gratings, they diffract the light into ± 1 orders to form a four-beam MOT (Nshii, et al., 2013). The fabricated grating exhibits a first diffraction order efficiency of 36% with an ellipticity of $\chi = 36°$ in their polarization when impinged with a

circularly polarized light at 780 nm. The grating size is $2mm \times 2mm$, a number chosen with a balance between fabrication feasibility and the height of the beam overlapping (trapping) region from the chip surface.

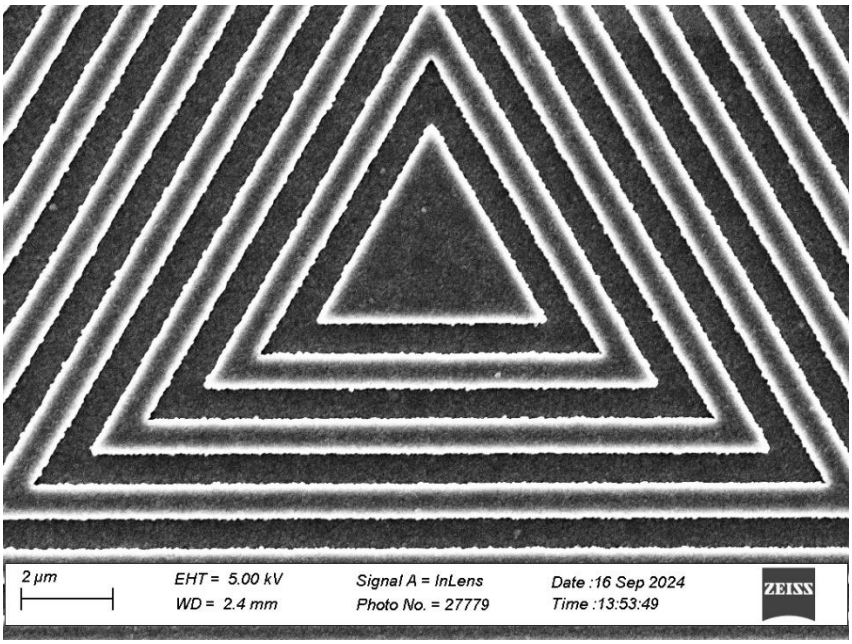

Figure 4-18 SEM image of the fabricated diffraction grating.

Figure 4.16 shows the optical setup for the GMOT experiment. The same cooling laser beam is sent into the tapered amplifier (TA) for the high optical power (> 100 mW) required to operate the GMOT. In order to efficiently cover the whole area of the diffraction grating and increase the beam overlap volume, we use a beam expander (Edmund Optics NIR Draconis® Broadband Beam Expander) to expand the gaussian beam waist diameter to ~37.5 mm. The beam expander has a reflection of $< 0.5\%$, with $< \frac{\lambda}{4}$ wavefront error. The expanded beam is sent through a quarter waveplate to give it a circular polarization and passes through the vacuum glass cell. The grating is mounted on a tip-tilt optical mount attached to an XY linear stage, giving the necessary degrees of freedom to align the input beam to the center of the grating pattern and the retroflected light to coincide with the incident beam. To prevent the grating chip from scratching the glass cell while ensuring the GMOT still forms inside the vacuum cell, the chip is intentionally mounted ~ 0.5 mm away from the bottom edge of the cell. Since the GMOT forms only a few mm away from the inner cell wall, we need to inject different currents into the anti-Helmholtz coil pair such that the quadrupole field zero point is shifted closer to the bottom inner edge of the vacuum cell. For repump, we use the same 795 nm laser as in the conventional MOT setup, but adjust its power at 10% of the cooling beam.

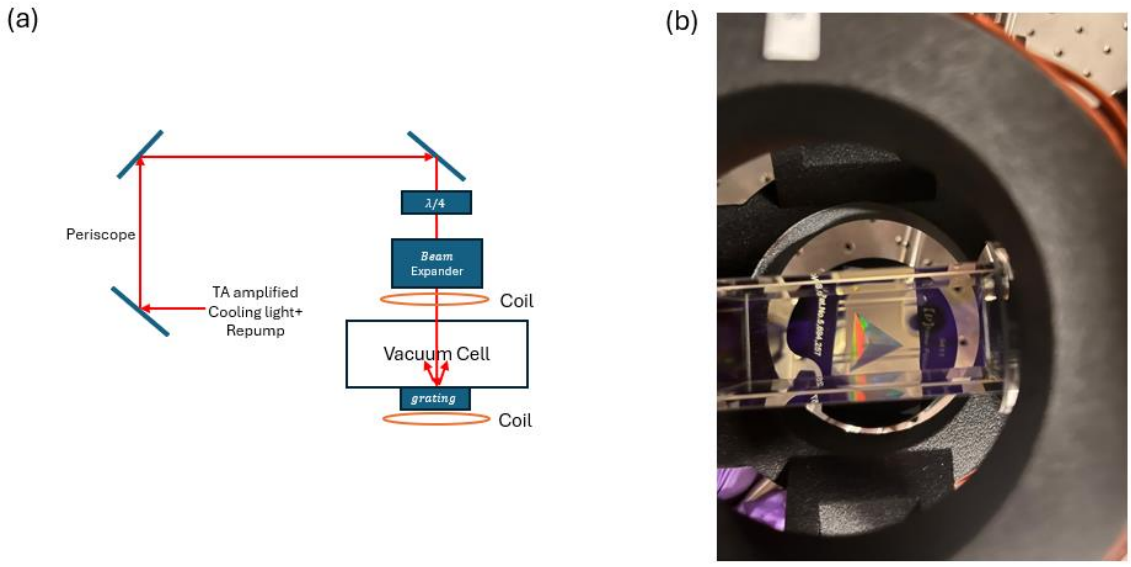

Figure 4-19 (a) Schematic of the GMOT testing setup; (b) Top view of the experiment setup showing the quadrupole field coils, the vacuum glass cell and the mounted grating.

Despite extensive parameter search including incident beam power ($20 - 130\ mW$), cooling laser detuning ($7 - 19\ MHz$), quadrupole field gradient ($10 - 20\ G/cm$) and sweeping the field zero point, we were unable to achieve atom trapping in our GMOT setup. During the trouble shooting process, several potential factors were ruled out, including the expanded beam quality and cell coating birefringence. To further investigate the potential issues, we decided to send the grating chip to a research group in University of Strathclyde where they were able to successfully achieve a GMOT, ruling out the grating chip itself being the limiting factor.

Based on current evidence, we suspect that magnetic field profile might be the important issue that frustrated our attempt at trapping atoms using the fabricated grating. During the experiment, it became apparent that the magnetic coils used in our setup might not have been properly aligned with respect to the grating chip due to the alignment procedure heavily dependent on visual estimation. Misalignment could lead to an asymmetrical magnetic field, resulting in poor overlap between the field zero point and the trapping region, which would adversely affect the ability to trap atoms. Similar issues were also discovered in our conventional MOT setup where a minor shift in the position of the magnetic coils led to significantly weakened MOT fluorescence.

The results from our tests highlight the critical importance of precise magnetic field control in achieving a GMOT. Moving forward, we are planning to replace the traditional anti-Helmholtz coil pair with a planar coil chip based on a PCB circuit board, where two groups of coils with opposite current generates a similar magnetic field profile for trapping. The grating chip will be directly mounted at the center of the coil chip, ensuring a precise alignment between the field center and the grating pattern. Magnetic field characterization will also be carried out for the PCB

board coil so that we can operate it at a favorable condition for the GMOT, making sure that zero-field position is appropriately located inside the trapping region.

4.9 Conclusion and outlooks

In this chapter, we have successfully built the infrastructure for a Raman light pulse cold atom gravimeter, including the vacuum system, the optical system, the RF circuits and the experiment control electronics, and succeeded in implementing the magneto-optical trap and sub-doppler cooling for rubidium 87 atoms. Future plans for state preparation, Raman interferometry and state detection procedures are also detailed in the above sections, with potential issues and challenges indicated.

Future efforts will focus on completing the gravity measurement with cold atom interferometry and further improving the robustness and portability of the apparatus. Specifically, we will focus on the integration of nanophotonic technologies into cold atom gravimeters. This includes:

1. Achieving grating magneto-optical trap (GMOT). This eliminates the need for bulky beam splitters and mirrors typically used in traditional MOT setups, making cold atom gravimeters more suitable for deployment in field applications where space and stability are critical.

2. Metasurfaces. This includes metasurface lenses that can serve in state detection system to enhance fluorescence collection efficiency and potentially integrate with diffraction grating to improve the MOT imaging. Metasurface tophat beam shaper can be used to ensure a uniform Rabi frequency across the atomic ensemble to improve pulse fidelity and achieve high contrast and precision in the interferometric fringes.

3. Chip scale narrow linewidth lasers. By leveraging photonic integrated circuit technology on a CMOS compatible platform, such lasers can achieve ultranarrow linewidth, frequency agility and beam delivery without external cavities and extended optical setups, drastically reducing the footprint while improving the robustness of the interferometry system. The improved frequency stability also enhances the measurement precision of the cold atom gravimeter.

5 Conclusion and future steps

In this work, we have developed multiple metasurface optics in silicon-on-sapphire tailored for various quantum applications based on neutral atom platforms, with successful demonstration on polarization optics for quantum magnetometry and metasurface optical trap array for quantum computing. For magnetometry, we integrate our millimeter scale metasurface PBS into an NMOR magnetometer and achieved an integrated sensitivity of 0.8660 nT across 500 kHz signal bandwidth, limited by the photo detector and the transmission loss of the metasurface. For atom trapping, we characterized the fabricated metasurface bottle beam trap generator and observed the predicted dark trap intensity profile at the focal plane. Both devices exhibit performance degradation compared to numerical simulation, which we attributed to (and backed up with simulation data) fabrication imperfection and optical alignment errors. We proposed multiple methods to mitigate these errors, including implementing AR coating on the metasurface substrate, acquiring dopped SOS sample to alleviate the charging issue during E-beam writing and improving the silicon etching recipe.

We have also noticed that the polarization insensitive metasurface beam shapers (such as the bottle beam trap generator) suffer less from performance deviation due to fabrication error than the birefringent beam deflecting devices such as the metasurface PBS. This is potentially due to two important factors: 1. Beam deflecting metasurfaces have other loss channels that degrade their performance, including the non-deflecting center order and higher order diffractions, which is non-existent in the transmissive beam shapers; 2. Polarizing optics such as PBS requires asymmetric meta-atoms for the birefringence, which is less tolerant to fabrication imperfection. One potential strategy is switching to metasurface based on geometric phase that arises from space-variant orientation of the meta-atoms. Usually, a single geometry of the meta-atom is selected such that it acts as a half waveplate when operating on the linear polarization $x - y$ basis. When the meta-atom is rotated by θ in the $x - y$ coordinate, the geometric phase imposed is given by $\Delta\phi_G = -2\sigma\theta$ where σ is photon helicity, equal to 1 and -1 for RCP and LCP polarizations. The metasurface can thus impose controlled circular birefringence while maintaining uniform transmission amplitude determined by the meta-atom geometry, resulting in high diffraction efficiency across broad operation spectrums. The orientation angle θ is less sensitive to fabrication error compared to the geometry (length and width) of the meta-atom, making the device performance robust against such imperfections. In addition, the single geometry of the meta-atom can be optimized by immediately doing in-situ optical polarimetry characterization across a variety of meta-atom shapes fabricated and selecting the one with the best birefringence behavior (McGehee, et al., 2021). This method also avoids the fabrication error caused by the long term parameter drift during E-beam writing and etching.

We have also successfully built our lab's first cold atom setup and demonstrated atom trapping and sub-doppler cooling, with detailed plans on the next steps – state preparation and atom interferometry. Throughout the experiment, it was found that the magnetic field profile played an

important role in the cold atom experiment, and less ideal field condition contributed to atom loss and decreased cooling efficiency. We plan to improve our magnetic coil system in the future, including implementing magnetic shielding, improving coil geometry and substituting some conventional coils with planar PCB board coils that are more compact and user-friendly.

We will also focus on introducing nanophotonic components into the cold atom gravimeter setup to achieve a ruggedized, miniaturized and energy efficient system. Specifically, we will continue to push on achieving grating MOT with our collaborators with the improved optical and magnetic coil setup. We will leverage our expertise in fabricating SOS metasurface optics to implement metasurface lenses for improved atom imaging and state detection as well as metasurface beam shaper for optimized pulse profile to improve interferometry contrast and resilience against environmental noises. Finally, we will adopt the chip scale narrow linewidth laser with ultrahigh Q PIC resonators developed by our collaborator at UCSB to reduce the size and complexity of the optical setup, while enhancing the sensitivity and accuracy of our cold atom gravimeter.

A Appendix

A.1 Volume analysis of metasurface-integrated magnetometer

We compare the volume of the polarimetry subsystem, consisting of the beam-splitting optic and detectors, for the metasurface PBS, cube PBS, and Wollaston prism. The metasurface PBS is estimated to provide a 15 to 35% reduction in volume in comparison to the other two approaches. This estimate takes into account a ~3 mm propagation distance of the split beams from the metasurface to the detector, which can be further reduced by incorporating focusing functionality in the metasurface design, so that the metasurface acts as both a PBS and lens (with short ~mm focal distance).

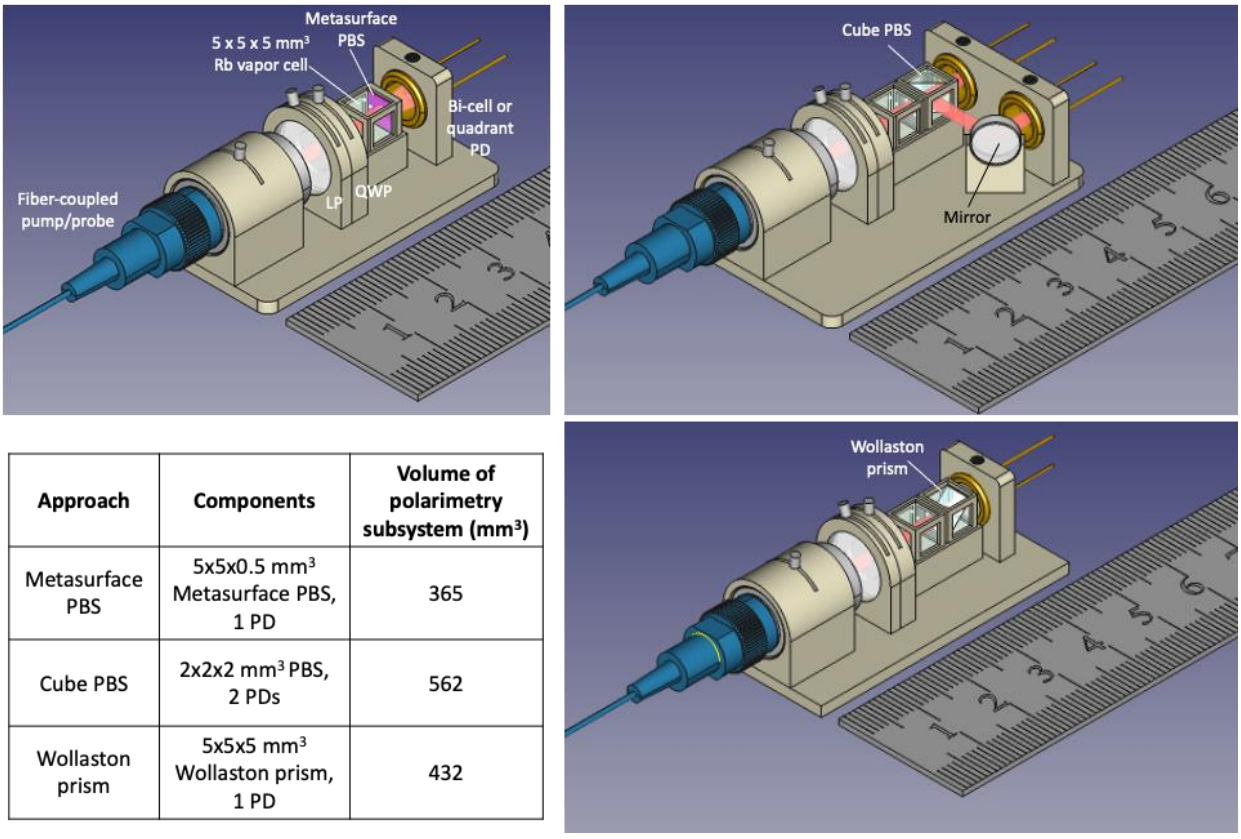

Approach	Components	Volume of polarimetry subsystem (mm³)
Metasurface PBS	5x5x0.5 mm³ Metasurface PBS, 1 PD	365
Cube PBS	2x2x2 mm³ PBS, 2 PDs	562
Wollaston prism	5x5x5 mm³ Wollaston prism, 1 PD	432

Figure A-1 CAD drawing of atomic magnetometers with metasurface PBS, cube PBS and Wollaston prism in the polarimetry subsystem. Volume estimations for the three models are also included.

A.2 Plane-wave approximation

Here we justify our assumption that the phase profile $\varphi(x, y)$ of our metasurface polarizing beamsplitter that is designed for a normal plane wave incidence would still apply to the case where

the incident beam has a Gaussian profile. Let us consider a Gaussian source polarized along the x direction:

$$U(x,y,z) = E_0\hat{x}\frac{w_0}{w(z)}\exp\left(-\frac{x^2+y^2}{w(z)^2}\right)exp\left(-i(kz + k\frac{x^2+y^2}{2R(z)} - \psi(z))\right) \quad (A.1)$$

where w_0 is the waist radius, $w(z) = w_0\sqrt{1+(\frac{\lambda z}{\pi w_0^2})^2}$ is the radius at which the field amplitudes decay to $\frac{1}{e}$ of their axial values, $R(z) = \frac{z^2+(\frac{\pi w_0^2}{\lambda})^2}{z}$ is the radius of curvature, $\psi(z) = \arctan(\frac{\lambda z}{\pi w_0^2})$ is the Gouy phase.

Our main argument here is that $U(x,y,z)$ *is* a solution to the paraxial Helmholtz equation, and can thus be well-approximated by a normal incident plane wave plus a small component of paraxial wave:

$$\begin{aligned} U(x,y,z) &= \iint u(k_x,k_y)e^{-i(k_x x+k_y y+k_z z)}dk_x dk_y \\ &= \iint e^{-ikz}u(k_x,k_y)e^{-i\left(k_x x+k_y y-\frac{1}{2k}(k_x^2+k_y^2)z\right)}dk_x dk_y \end{aligned} \quad (A.2)$$

where we have used the fact that $k_x, k_y \ll k_z$.

We claim that the elliptical posts will impose the same phase shift $\varphi(x,y) = \mp kxsin\Theta$ for a paraxial plane wave, so that the gaussian source after transmitting through the metasurface will become: $U'(x,y,z) = \iint e^{-ik(z\mp xsin\Theta)}u(k_x,k_y)e^{-i\left(k_x x+k_y y-\frac{1}{2k}(k_x^2+k_y^2)z\right)}dk_x dk_y$ which is just the gaussian beam deflected by angle $\mp\Theta$. In what follows, we justify our claim. Let us quantify this argument by calculating the Fourier component $u(\theta)$ of a Gaussian beam, where θ indicates the angle between the wavevector and the propagation direction $\hat{z}$. We write the k-vector in spherical basis: $k_x = Ksin\theta cos\varphi$, $k_y = Ksin\theta sin\varphi$, $k_x = Kcos\theta$. Here φ is the azimuth angle.

$$\begin{aligned} u(K,\theta) &= \iiint U(x,y,z)e^{i(k_x x+k_y y+k_z z)}dxdydz \\ &= E_0 w_0\int_{-\infty}^{+\infty}\frac{1}{w(z)}e^{i(Kcos\theta-k)z+\psi(z))}dz \\ &\quad\times\iint e^{-\frac{x^2+y^2}{w(z)^2}}e^{i(Ksin\theta sin\varphi x+Ksin\theta sin\varphi y-k\frac{x^2+y^2}{2R(z)})}dxdy \end{aligned} \quad (A.3)$$

It can be proven that

$$|u(K,\theta)| = C(w_0,\lambda,E_0)|g(z,)|e^{-\frac{K^2w_0^2}{4}sin^2\theta} \quad (A.4)$$

Here $C(w_0, \lambda, E_0)$ is a constant that only depends on the incident Gaussian beam parameters. $g = \int_{-\infty}^{+\infty} \frac{e^{i(Kcos\theta - k)z + \psi(z))}}{\sqrt{1+(\frac{\lambda z}{\pi w_0^2})^2}} dz$ is a complex function of θ.

If $\alpha = Kcos\theta - k \neq 0$, then $g(\alpha) = \int_{-\infty}^{+\infty} \frac{e^{i(\alpha z + \psi(z))}}{\sqrt{1+(\frac{\lambda z}{\pi w_0^2})^2}} dz$ converges, therefore the Fourier components that matter are the ones with $K = \frac{k}{cos\theta}$. We now have:

$$|u(\theta)| \propto e^{-\frac{k^2 w_0^2}{4} tan^2\theta} \tag{A.5}$$

The angular dependence of the Fourier component decays very fast with respect to θ. We define a cutoff angle θ_0 where its corresponding Fourier coefficient is only $e^{-4} \approx 1.8\%$ of that of the normal component. Then:

$$\theta_0 = arctan\left(\frac{4}{k w_0}\right) \tag{A.6}$$

For our simulation, $w_0 = 4\,\mu m$ and $k = 7.9 \times 10^6 m^{-1}$, the cutoff angle $\theta_0 = 7°$. For a realistic beam size $w_0 = 1\,mm$ in the magnetometer experiment, $\theta_0 = 0.03°$. It follows that the Gaussian source in the actual experiment is very well approximated by a normal incident plane wave. Indeed, simulated phase shift of a 795-nm plane wave with incident angle at the cutoff angle $\theta_0 = 0.03°$ shows less than 10^{-6} deviation from that for a normally incident plane wave.

A.3 Determination of transmittance and polarization extinction ratio

In this section we describe our method for calculating the transmittance T and the polarization extinction ratio (PER) of the metasurface PBS. The transmittance T_0 from the transmission of the field through the metasurface is first extracted from a field monitor placed a few wavelengths away from the metasurface. In the far-field projection, the transmitted field intensity $|E|^2$ is integrated at the two PBS outputs whose locations are determined by the splitting angle 2θ. The integration area is determined through the solid angle Ω of the projection hemisphere. We choose $\Omega = 2\pi(1 - cos7°)$ (half angle 7°) to ensure we have covered most of the scattered light and the two integration

areas do not overlap. The reported transmittance values in the main text take into account both the initial transmittance T_0 and the fraction of intensity within the solid angle:

$$T = T_0 \times \frac{\int_{cone}|E|^2}{\int_{hemisphere}|E|^2} \tag{A.7}$$

We now define I_{main} to be the integrated intensity in the far field that corresponds to the main polarization mode and I_{leak} to be the intensity corresponding to the orthogonal polarization mode, then the PER is calculated as:

$$PER = \frac{I_{main}}{I_{leak}} \tag{A.8}$$

A.4 Photon shot noise in balanced polarimetry based on a non-ideal PBS

In this section we derive the photon shot noise for a non-ideal PBS. The derivation follows mostly from (Budker, Kimball, & DeMille, Atomic physics: an exploration through problems and solutions, 2004). For a linearly polarized light whose polarization angle is φ measured from the y-axis, the number of photons received on each detection channel after going through the polarizing beamsplitter are:

$$N_1 = NT_{-1x}sin^2\varphi + Nb_yT_{-1y}cos^2\varphi \tag{A.9}$$

$$N_2 = NT_{1y}cos^2\varphi + Nb_xT_{1x}sin^2\varphi \tag{A.10}$$

Divide A.9 by A.10 and take differentiation, we have:

$$\frac{N_2\delta N_1 - N_1\delta N_2}{N_2^2} = \frac{N^2 sin2\varphi(T_{-1x}T_{1y} - T_{1x}T_{-1y})}{N_2^2}\delta\varphi \tag{A.11}$$

We can express $sin2\varphi$ in terms of N_1 and N_2:

$$sin2\varphi = 2\frac{\sqrt{N_1 - T_{-1y}N_2/T_{1y}}\sqrt{N_2 - T_{1x}N_1/T_{-1x}}}{N\sqrt{T_{-1x}T_{1y}}\left(1-(\frac{T_{1x}T_{-1y}}{T_{-1x}T_{1y}})\right)} \tag{A.12}$$

since photon numbers obey Poisson statistics, we have $\delta N_1 = \sqrt{N_1}, \delta N_2 = \sqrt{N_2}$. Assume the noises from two channels add in quadrature, we finally have:

$$\delta\varphi = \frac{1}{2}\sqrt{\left(\frac{N_1}{N_1 - T_{-1y}N_2/T_{1y}}\right)\left(\frac{N_2}{N_2 - T_{1x}N_1/T_{-1x}}\right)\frac{N_1+N_2}{N^2T_{-1x}T_{1y}}}$$
$$= \sqrt{\left(\frac{N_1}{N_1 - T_{-1y}N_2/T_{1y}}\right)\left(\frac{N_2}{N_2 - T_{1x}N_1/T_{-1x}}\right)\frac{N_1+N_2}{NT_{-1x}T_{1y}}}\delta\varphi_0 \quad (A.13)$$

Assuming small polarization rotation, which means the polarimeter operates near the balanced position, we can let $N_1 = N_2$ and solve for φ:

$$tan^2\varphi = \frac{T_{1y} - T_{-1y}}{T_{-1x} - T_{1x}} \quad (A.14)$$

Plug Eq. S back into Eq. S, we have $N_1 = N_2 = \frac{N(T_{-1x}T_{1y} - T_{1x}T_{-1y})}{T_{-1x} - T_{1x} + T_{1y} - T_{-1y}}$, and

$$\delta\varphi = \sqrt{\frac{2\left(1 - \frac{T_{1x}T_{-1y}}{T_{-1x}T_{1y}}\right)}{\left(1 - \frac{T_{1x}}{T_{-1x}}\right)\left(1 - \frac{T_{-1y}}{T_{1y}}\right)\left(T_{-1x} - T_{1x} + T_{1y} - T_{-1y}\right)}}\delta\varphi_0 \quad (A.15)$$

A.5 Extraction of the complex refractive index using spectroscopic ellipsometry

In order to extract the optical properties of silicon for the SOS wafer from Roditi, we employed generalized spectroscopic ellipsometry (Woollam, 2012) as well as the transmission/reflection spectroscopy. Figure S1(a, b) shows the raw measured ellipsometry data Ψ and Δ of A_{ne} (in green) and the corresponding model fitted data (in red) for the center region of the SOS wafer with the angle of incidence $\theta_i = 60°$. A_{ne} is the ratio between the two Fresnel coefficients r_{pp} and r_{ss}. R-plane cut sapphire is slightly anisotropic, but from the measurement we found out the cross-polarization terms A_{ps} and A_{sp} is close to zero. We also observe no obvious difference of the fitting results when considering anisotropy of sapphire or assuming sapphire as an isotropic substrate. Additionally, as shown in Figure S2, we measured reflection of the SOS wafer at normal incidence under different polarization of light and observe no shift of the Fabry–Pérot fringes.

$$A_{ne} = \rho = \frac{r_{pp}}{r_{ss}} = \tan\left(\Psi_{A_{ne}}\right) e^{i\Delta_{A_{ne}}} \tag{A.16}$$

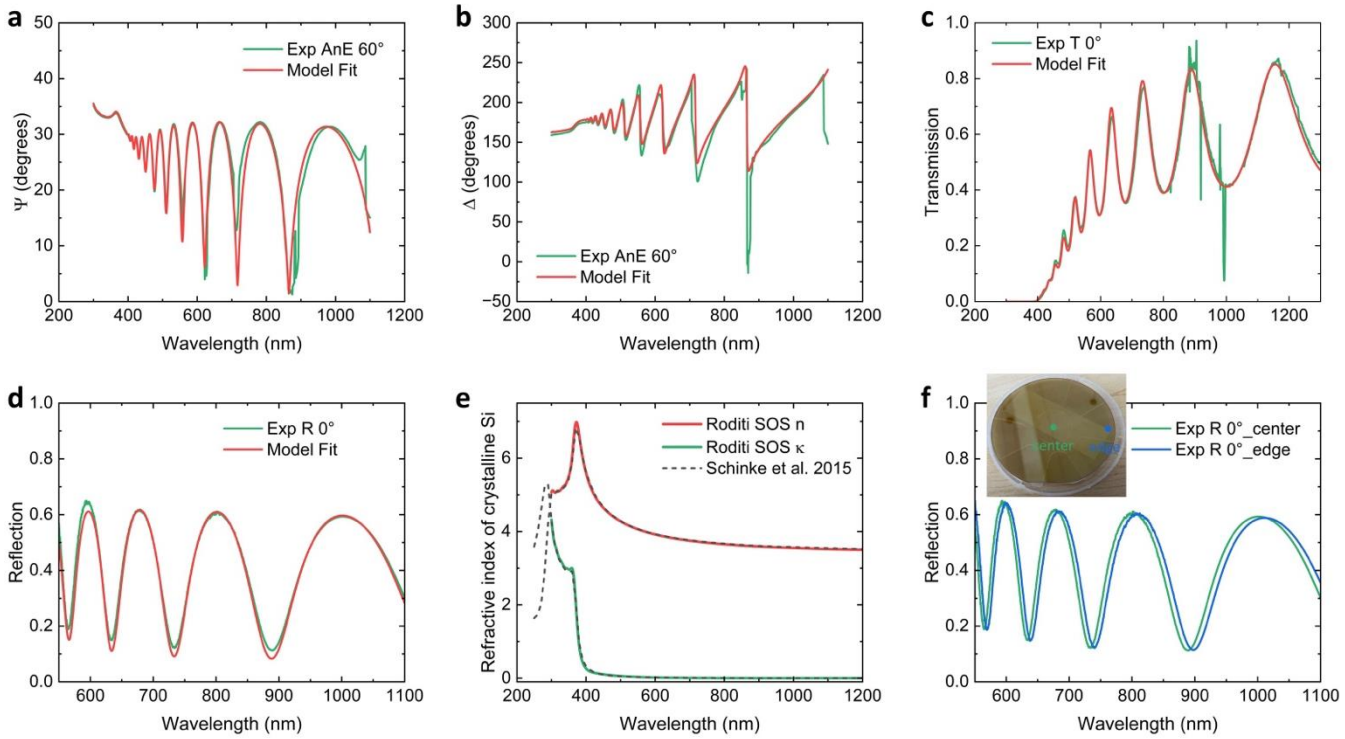

Figure A-2 Raw ellipsometry data Ψ (a) and Δ (b) of A_{ne} for silicon on sapphire wafer at $\theta_i = 60°$, transmission (c) and reflection (d) data at normal incidence, showing good consistence between the experimental data (green lines) and model fit data (red lines). (e) Extracted complex refractive index of single crystalline silicon of Roditi SOS wafer (solid lines), compared with single crystalline silicon data from literature[2] (dashed lines). (f) Measured reflection spectra of the SOS wafer at the center and edge, the shift of the fringes showing the variation of thickness.

$$A_{ps} = \frac{r_{ps}}{r_{pp}} = \tan\left(\Psi_{A_{ps}}\right) e^{i\Delta_{A_{ps}}} \quad (A.17)$$

$$A_{sp} = \frac{r_{sp}}{r_{ss}} = \tan\left(\Psi_{A_{sp}}\right) e^{i\Delta_{A_{sp}}} \quad (A.18)$$

We also included the transmission and reflection spectra into the model for fitting, and the extracted complex refractive index of silicon is shown in Figure S1(e), showing nice consistency with the data from recent literature (Schinke, et al., 2015). In addition, we examined different regions across the 4-inch wafer and found that there are small variations of the thickness of the silicon layer. The shift of the Fabry–Pérot fringes in Figure S1(f) clearly reveal that. According the fitting, we observe the thickness of the silicon layer is 494.0 ± 0.232 nm at the center, and 499.2 ± 0.076 nm at the edge of the wafer.

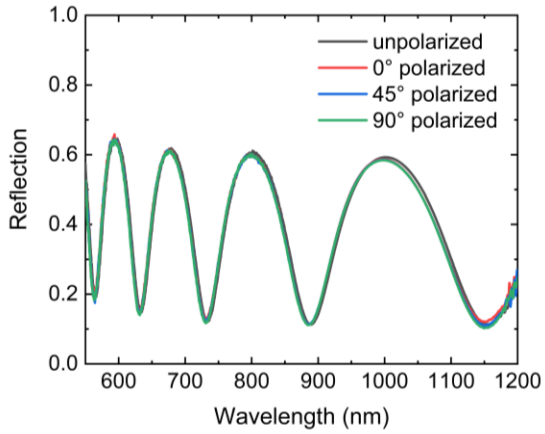

Figure A-3 Measured reflection spectra of the SOS wafer with normal incident light unpolarized, and polarized at different angles, showing no obvious difference.

A.6 Calculated transmission and reflection of the metasurface PBS design being fabricated in this work

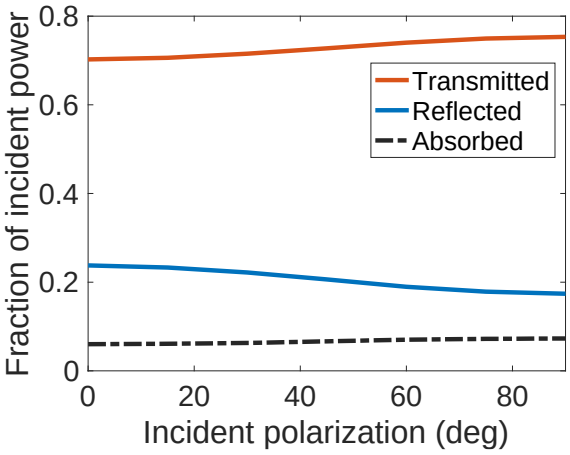

Figure A-4 Calculated total transmission, reflection, and absorption (in the device layer) for the metasurface PBS.

A.7 Simulation of non-ideal geometries

We modeled the effects of various deviations from metasurface design due to fabrication, such as the inclusion of a 50-nm-thick SiO_2 etch mask, a remaining silicon pedestal layer from under-etching, and tapering in the sidewall profile of the meta-atoms. The calculated transmission and reflection values at an incident polarization of 45° are shown in Table A.1. We note that this set of simulations does not account for the reflection of an incident beam at the first air-sapphire interface.

Table A-1 Calculated transmission and reflection through the metasurface PBS.

	Fraction of incident power				
	L1 (y)	R1 (x)	0^{th} order	Total transmitted	Total reflected
As designed	0.40	0.35	< 0.02	0.79	0.14
With SiO_2 etch mask	0.42	0.36	< 0.02	0.81	0.13
With 10 nm pedestal	0.36	0.30	< 0.02	0.70	0.23
With 15 nm pedestal	0.32	0.29	< 0.02	0.66	0.27
With 5° taper	0.16	0.17	0.37	0.76	0.17

Simulation results suggest that the SiO_2 etch mask does not alter the transmission or beam-splitting performance, while a silicon pedestal layer as thin as 10-15 nm can significantly increase reflection, thereby reducing transmission.

We modeled a tapered sidewall structure based on SEM images of the etched silicon. The simulated optical response of the metasurface PBS with a 5 degree sidewall tapering is plotted in Figure A.5 which shows a prominent zeroth-order mode and higher order scattering modes appearing in the far field.

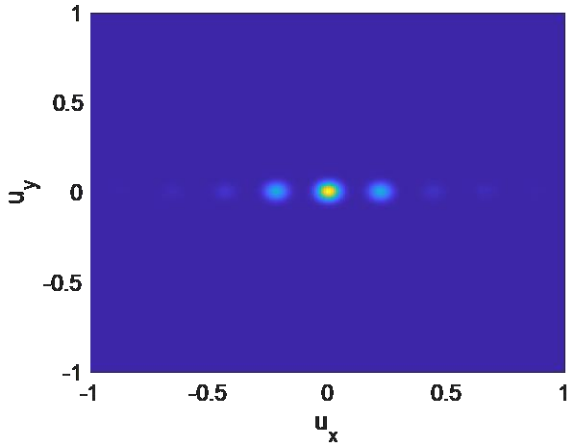

Figure A-5 Simulated far-field profile of the metasurface design with a 5° taper in the sidewall angle.

A.8 Modeling of single-layer MgF_2 AR coating

We modeled the transmission response of our metasurface design with a single-layer AR coating comprising of MgF_2 (thickness = 144.65 nm, $n \sim 1.38$ at 795 nm) deposited on the sapphire substrate and showed an improvement in transmission of around 10%. The MgF2 layer can be deposited via sputtering or atomic layer deposition prior to device fabrication.

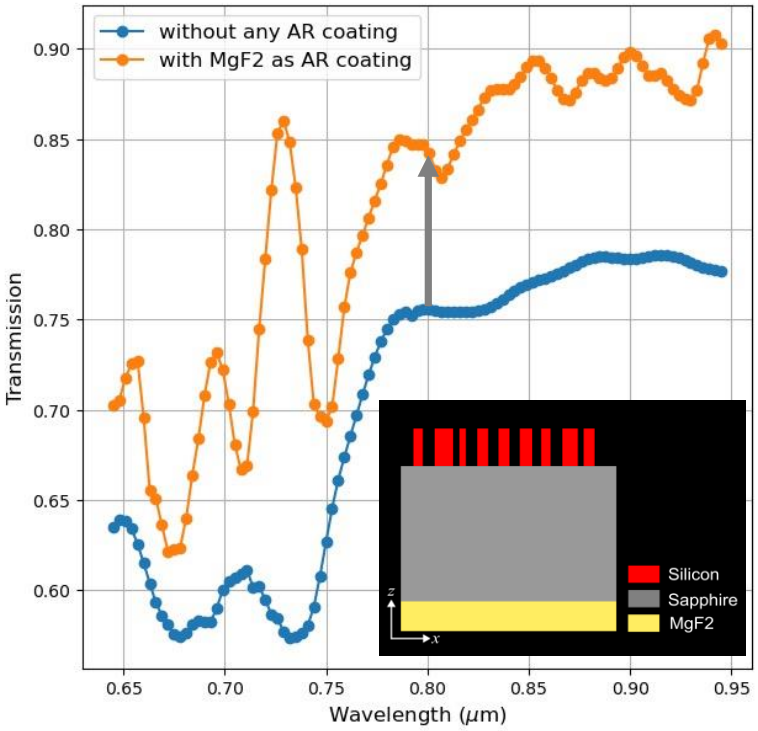

Figure A-6 Simulated transmission as a function of wavelength for the metasurface PBS design with and without a single-layer AR coating on the sapphire substrate.

A.9 Sub-millisecond polarization switching by liquid crystal (LC) waveplate

We have performed optical measurements to characterize the polarization switching time by the LC waveplate. Figure A.7 shows the optical setup for the polarization switching measurements. The incident beam gets converted to circular or linear polarization depending on the logic level of the control signal sent to the LC waveplate, with low being (the configuration to generate) circular polarization and high being linear polarization. The output from the LC waveplate is then sent to a polarizer with its axis orthogonal to the linear polarization generated by the LC waveplate in 1 state. A photo detector detects light intensity, with low output voltage indicating linear polarization and high output voltage circular.

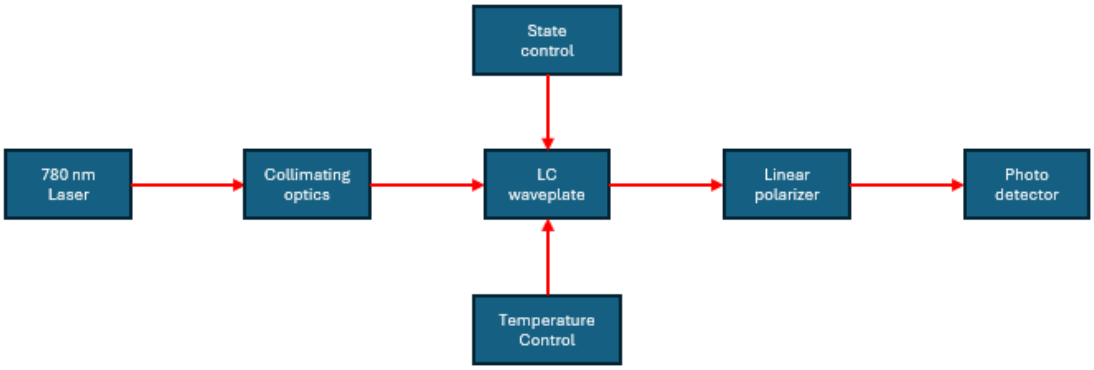

Figure A-7 Optical setup for characterizing the switching time of the LC waveplate.

Figure A.8 shows the time trace of the photo detector signal and control signal demonstrating the polarization transition in real time. The polarization switching is estimated to be around 0.3 ms from the trace, which is short enough for the polarization configuration to switch between cooling ($\sigma^+ - \sigma^-$) and Raman ($lin \perp lin$) without interfering with both processes.

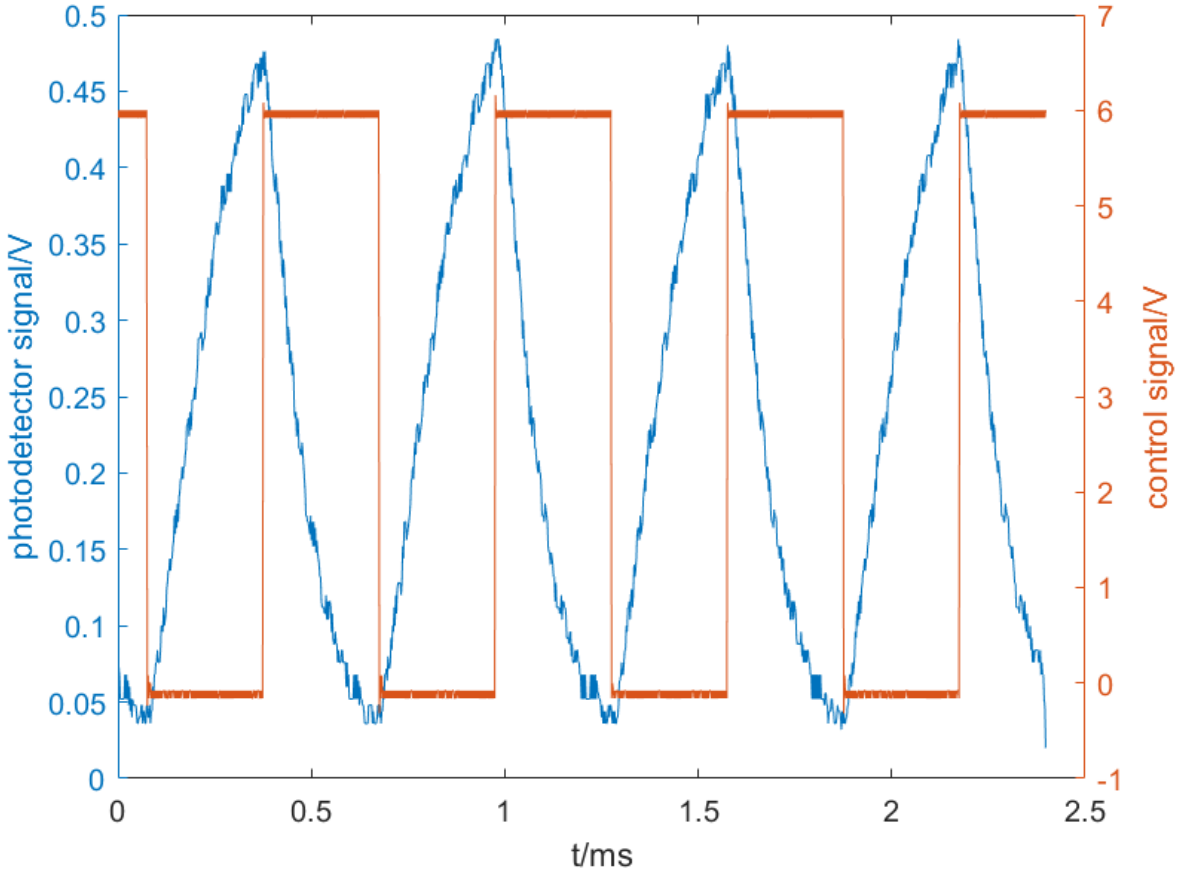

Figure A-8 Time trace showing the polarization transition. Blue – photo detector signal. High indicates circular polarization while low indicates linear polarization. Orange – control voltage. High level means linear polarization configuration while low means circular polarization configuration.

Bibliography

Adams, C. S., Pritchard, J. D., & Shaffer, J. P. (2019). Rydberg atom quantum technologies. *Journal of Physics B: Atomic, Molecular and Optical Physics, 53*, 012002.

Aeppli, A., Kim, K., Warfield, W., Safronova, M. S., & Ye, J. (2024). Clock with 8× 10-19 systematic uncertainty. *Physical Review Letters, 133*, 023401.

An, S., Zheng, B., Tang, H., Shalaginov, M. Y., Zhou, L., Li, H., . . . others. (2021). Multifunctional metasurface design with a generative adversarial network. *Advanced Optical Materials, 9*, 2001433.

Andreou, A. G., Kalayjian, Z. K., Apsel, A., Pouliquen, P. O., Athale, R. A., Simonis, G., & Reedy, R. (2001). Silicon on sapphire CMOS for optoelectronic microsystems. *IEEE Circuits and Systems Magazine, 1*, 22–30.

Antypas, D., Fabricant, A., Stalnaker, J. E., Tsigutkin, K., Flambaum, V. V., & Budker, D. (2019). Isotopic variation of parity violation in atomic ytterbium. *Nature Physics, 15*, 120–123.

Arbabi, A., Horie, Y., Bagheri, M., & Faraon, A. (2015). Dielectric metasurfaces for complete control of phase and polarization with subwavelength spatial resolution and high transmission. *Nature nanotechnology, 10*, 937–943.

Arnold, D., Siegel, S., Grisanti, E., Wrachtrup, J., & Gerhardt, I. (2017). A rubidium Mx-magnetometer for measurements on solid state spins. *Review of Scientific Instruments, 88*.

Basu, A., & Velásquez-García, L. F. (2016). An electrostatic ion pump with nanostructured Si field emission electron source and Ti particle collectors for supporting an ultra-high vacuum in miniaturized atom interferometry systems. *Journal of Micromechanics and Microengineering, 26*, 124003.

Battelier, B., Barrett, B., Fouché, L., Chichet, L., Antoni-Micollier, L., Porte, H., . . . Bouyer, P. (2016). Development of compact cold-atom sensors for inertial navigation. *Quantum optics*, *9900*, pp. 21–37.

Bekenstein, R., Pikovski, I., Pichler, H., Shahmoon, E., Yelin, S. F., & Lukin, M. D. (2020). Quantum metasurfaces with atom arrays. *Nature Physics, 16*, 676–681.

Bell, W. E., & Bloom, A. L. (1957). Optical detection of magnetic resonance in alkali metal vapor. *Physical Review, 107*, 1559.

Bidel, Y., Zahzam, N., Bresson, A., Blanchard, C., Cadoret, M., Olesen, A. V., & Forsberg, R. (2020). Absolute airborne gravimetry with a cold atom sensor. *Journal of Geodesy, 94*, 1–9.

Bruns, S., Vergöhl, M., Zickenrott, T., & Bräuer, G. (2016). Deposition of abrasion resistant single films and antireflective coatings on sapphire. *Surface and Coatings Technology, 290*, 10–15.

Budker, D., & Romalis, M. (2007). Optical magnetometry. *Nature physics, 3*, 227–234.

Budker, D., Kimball, D. F., & DeMille, D. P. (2004). *Atomic physics: an exploration through problems and solutions*. Oxford University Press, USA.

Budker, D., Kimball, D. F., Rochester, S. M., Yashchuk, V. V., & Zolotorev, M. (2000). Sensitive magnetometry based on nonlinear magneto-optical rotation. *Physical Review A, 62*, 043403.

Budker, D., Kimball, D. F., Yashchuk, V. V., & Zolotorev, M. (2002). Nonlinear magneto-optical rotation with frequency-modulated light. *Physical Review A, 65*, 055403.

Budker, D., Yashchuk, V., & Zolotorev, M. (1998). Nonlinear magneto-optic effects with ultranarrow widths. *Physical review letters, 81*, 5788.

Bui Dang, H., & Romalis, M. (2009). Atomic Magnetometry in the AttoTesla Regime. *APS Division of Atomic, Molecular and Optical Physics Meeting Abstracts*, *40*, pp. OPQ–30.

Butts, D. L. (2011). *Light pulse atom interferometry at short interrogation times for inertial navigation*. Ph.D. dissertation, Massachusetts Institute of Technology.

Canciani, A., & Raquet, J. (2016). Absolute positioning using the Earth's magnetic anomaly field. *NAVIGATION: Journal of the Institute of Navigation, 63*, 111–126.

Cantor, R., Lee, L. P., Matlashov, A., & Vinetskiy, V. (1997). A low-noise, two-stage DC SQUID amplifier with high bandwidth and dynamic range. *IEEE transactions on applied superconductivity, 7*, 3033–3036.

Chen, S., Liu, W., Li, Z., Cheng, H., & Tian, J. (2020). Metasurface-empowered optical multiplexing and multifunction. *Advanced Materials, 32*, 1805912.

Chen, Y., Zhao, L., Zhang, N., Yu, M., Ma, Y., Han, X., . . . Jiang, Z. (2022). Single beam Cs-Ne SERF atomic magnetometer with the laser power differential method. *Optics Express, 30*, 16541–16552.

Cohen-Tannoudji, C., Dupont-Roc, J., & Grynberg, G. (1998). *Atom-photon interactions: basic processes and applications*. John Wiley & Sons.

Cohen-Tannoudji, C., Dupont-Roc, J., Haroche, S., & Laloë, F. J. (1970). Diverses résonances de croisement de niveaux sur des atomes pompés optiquement en champ nul. I. Théorie. *Revue de physique appliquée, 5*, 95–101.

Cristoloveanu, S. (1987). Silicon films on sapphire. *Reports on Progress in Physics, 50*, 327.

Dalibard, J., & Cohen-Tannoudji, C. (1989). Laser cooling below the Doppler limit by polarization gradients: simple theoretical models. *JOSA B, 6*, 2023–2045.

Degen, C. L., Reinhard, F., & Cappellaro, P. (2017). Quantum sensing. *Reviews of modern physics, 89*, 035002.

Dunning, A. J. (2015). *Coherent Atomic Manipulation and Cooling: Interferometric Laser Cooling and Composite Pulses for Atom Interferometry*. Springer.

Durfee, D. S., Shaham, Y. K., & Kasevich, M. A. (2006). Long-term stability of an area-reversible atom-interferometer Sagnac gyroscope. *Physical review letters, 97*, 240801.

Fang, C., Kim, M., Czaplewski, D. A., Mei, H., Deshpande, S., Yu, Z., . . . others. (2024). Metasurfaces That Enable Bottle-Beam Arrays for Neutral Atom Trapping. *2024 Conference on Lasers and Electro-Optics (CLEO)*, (pp. 1–2).

Fu, R., Chen, K., Li, Z., Yu, S., & Zheng, G. (2022). Metasurface-based nanoprinting: principle, design and advances. *Opto-Electronic Science, 1*, 220011–1.

Gao, S., Park, C.-S., Lee, S.-S., & Choi, D.-Y. (2019). All-dielectric metasurfaces for simultaneously realizing polarization rotation and wavefront shaping of visible light. *Nanoscale, 11*, 4083–4090.

Garrido Alzar, C. L. (2019). Compact chip-scale guided cold atom gyrometers for inertial navigation: Enabling technologies and design study. *AVS Quantum Science, 1*.

Gehm, M. E. (2003). Properties of 6Li. *Jetlab,*.

Georgi, P., Massaro, M., Luo, K.-H., Sain, B., Montaut, N., Herrmann, H., . . . Zentgraf, T. (2019). Metasurface interferometry toward quantum sensors. *Light: Science & Applications, 8*, 70.

Graf, M. T., Kimball, D. F., Rochester, S. M., Kerner, K., Wong, C., Budker, D., . . . Yashchuk, V. V. (2005). Relaxation of atomic polarization in paraffin-coated cesium vapor cells. *Physical Review A—Atomic, Molecular, and Optical Physics, 72*, 023401.

Graham, T. M., Song, Y., Scott, J., Poole, C., Phuttitarn, L., Jooya, K., . . . others. (2022). Multi-qubit entanglement and algorithms on a neutral-atom quantum computer. *Nature, 604*, 457–462.

Griffith, W. C., Knappe, S., & Kitching, J. (2010). Femtotesla atomic magnetometry in a microfabricated vapor cell. *Optics express, 18*, 27167–27172.

Grosz, A., Haji-Sheikh, M. J., & Mukhopadhyay, S. C. (2017). *High sensitivity magnetometers* (Vol. 19). Springer.

Gustavson, T. L., Landragin, A., & Kasevich, M. A. (2000). Rotation sensing with a dual atom-interferometer Sagnac gyroscope. *Classical and Quantum Gravity, 17*, 2385.

Herrmann, S., Dittus, H., Lämmerzahl, C., & others. (2012). Testing the equivalence principle with atomic interferometry. *Classical and Quantum Gravity, 29*, 184003.

Holman, A., Xu, Y., Sun, X., Wu, J., Wang, M., Seo, B., . . . Will, S. (2024). Trapping of Single Atoms in Metasurface Optical Tweezer Arrays. *arXiv preprint arXiv:2411.05321*.

Hu, J., Liang, Z., Zhou, P., Liu, L., Hu, G., Du, P., & Ye, M. (2024). Integrated optical rotation detection scheme for chip-scale atomic magnetometer empowered by silicon-rich SiNx metalens. *Optics Letters, 49*, 3364–3367.

Hu, J., Lu, J., Liang, Z., Liu, L., Wang, W., Zhou, P., & Ye, M. (2022). Integrated polarization-splitting grating coupler for chip-scale atomic magnetometer. *Biosensors, 12*, 529.

Hu, T., Tseng, C.-K., Fu, Y. H., Xu, Z., Dong, Y., Wang, S., . . . others. (2018). Demonstration of color display metasurfaces via immersion lithography on a 12-inch silicon wafer. *Optics express, 26*, 19548–19554.

Hu, Y., Wang, X., Luo, X., Ou, X., Li, L., Chen, Y., . . . Duan, H. (2020). All-dielectric metasurfaces for polarization manipulation: principles and emerging applications. *Nanophotonics, 9*, 3755–3780.

Hu, Z., & Li, G. (2024). A dielectric metasurface for the generation of cold atoms. *Metamaterials XIV*, (p. PC1299020).

Huang, C., Zhang, C., Yang, J., Sun, B., Zhao, B., & Luo, X. (2017). Reconfigurable metasurface for multifunctional control of electromagnetic waves. *Advanced Optical Materials, 5*, 1700485.

Huang, R., Zhou, F., Li, X., Xu, P., Wang, Y., & Zhan, M. (2024). Metasurface optical trap array for single atoms. *Optics Express, 32*, 21293–21303.

Huang, X., Yuan, W., Holman, A., Kwon, M., Masson, S. J., Gutierrez-Jauregui, R., . . . Yu, N. (2023). Metasurface holographic optical traps for ultracold atoms. *Progress in Quantum Electronics, 89*, 100470.

Huber, M. E., Neil, P. A., Benson, R. G., Burns, D. A., Corey, A. F., Flynn, C. S., . . . Hilton, G. C. (2001). DC SQUID series array amplifiers with 120 MHz bandwidth (corrected). *IEEE Transactions on Applied Superconductivity, 11*, 4048–4053.

Hunter, D., Piccolomo, S., Pritchard, J. D., Brockie, N. L., Dyer, T. E., & Riis, E. (2018). Free-induction-decay magnetometer based on a microfabricated Cs vapor cell. *Physical Review Applied, 10*, 014002.

Imthurn, G. (2007). The history of silicon-on-sapphire. *Peregrine Semiconductor Corporation*.

Ipri, A. C. (1981). The properties of silicon-on-sapphire substrates, devices, and integrated circuits. *Silicon Integrated Circuits, Part A, Applied Solid State Science, Supplement, 2*, 253–395.

Isichenko, A., Chauhan, N., Bose, D., Wang, J., Kunz, P. D., & Blumenthal, D. J. (2023). Photonic integrated beam delivery for a rubidium 3D magneto-optical trap. *Nature communications, 14*, 3080.

Isichenko, A., Hunter, A. S., Bose, D., Chauhan, N., Song, M., Liu, K., . . . Blumenthal, D. J. (2024). Sub-Hz fundamental, sub-kHz integral linewidth self-injection locked 780 nm hybrid integrated laser. *Scientific Reports, 14*, 27015.

Jiang, X., & Henning, A. (2021). Precision metrology: from bulk optics towards metasurface optics. *Contemporary Physics, 62*, 199–216.

Jiménez-Martínez, R., Griffith, W. C., Wang, Y.-J., Knappe, S., Kitching, J., Smith, K., & Prouty, M. D. (2009). Sensitivity comparison of Mx and frequency-modulated bell–bloom Cs magnetometers in a microfabricated cell. *IEEE Transactions on Instrumentation and Measurement, 59*, 372–378.

Johnson, C. N., Schwindt, P. D., & Weisend, M. (2013). Multi-sensor magnetoencephalography with atomic magnetometers. *Physics in Medicine & Biology, 58*, 6065.

Johnson, C., Schwindt, P. D., & Weisend, M. (2010). Magnetoencephalography with a two-color pump-probe, fiber-coupled atomic magnetometer. *Applied Physics Letters, 97*.

Kangara, J. C., Hachtel, A. J., Gillette, M. C., Barkeloo, J. T., Clements, E. R., Bali, S., . . . others. (2014). Design and construction of cost-effective tapered amplifier systems for laser cooling and trapping experiments. *American Journal of Physics, 82*, 805–817.

Keder, D. A., Prescott, D. W., Conovaloff, A. W., & Sauer, K. L. (2014). An unshielded radio-frequency atomic magnetometer with sub-femtoTesla sensitivity. *Aip Advances, 4*.

Khorasaninejad, M., & Capasso, F. (2017). Metalenses: Versatile multifunctional photonic components. *Science, 358*, eaam8100.

Khorasaninejad, M., Chen, W. T., Devlin, R. C., Oh, J., Zhu, A. Y., & Capasso, F. (2016). Metalenses at visible wavelengths: Diffraction-limited focusing and subwavelength resolution imaging. *Science, 352*, 1190–1194.

Kitching, J. (2018). Chip-scale atomic devices. *Applied Physics Reviews, 5*.

Kitching, J., Knappe, S., & Donley, E. A. (2011). Atomic sensors–a review. *IEEE Sensors Journal, 11*, 1749–1758.

Knappe, S., Sander, T. H., Kosch, O., Wiekhorst, F., Kitching, J., & Trahms, L. (2010). Cross-validation of microfabricated atomic magnetometers with superconducting quantum interference devices for biomagnetic applications. *Applied Physics Letters, 97*.

Kominis, I. K., Kornack, T. W., Allred, J. C., & Romalis, M. V. (2003). A subfemtotesla multichannel atomic magnetometer. *Nature, 422*, 596–599.

Koyama, F. (2006). Recent advances of VCSEL photonics. *Journal of Lightwave Technology, 24*, 4502–4513.

Krzyzewski, S. P., Perry, A. R., Gerginov, V., & Knappe, S. (2019). Characterization of noise sources in a microfabricated single-beam zero-field optically-pumped magnetometer. *Journal of Applied Physics, 126*.

Kurashima, Y., Matsumae, T., Yanagimachi, S., Harasaka, K., & Takagi, H. (2019). An all-sapphire Cs gas cell for a chip-scale atomic clock. *Japanese Journal of Applied Physics, 58*, 096506.

Lalau-Keraly, C. M., Bhargava, S., Miller, O. D., & Yablonovitch, E. (2013). Adjoint shape optimization applied to electromagnetic design. *Optics express, 21*, 21693–21701.

Ledentsov, N. N., Makarov, O. Y., Shchukin, V. A., Kalosha, V. P., Ledentsov, N., Chrochos, L., . . . Turkiewicz, J. P. (2022). High speed VCSEL technology and applications. *Journal of Lightwave Technology, 40*, 1749–1763.

Lett, P. D., Watts, R. N., Westbrook, C. I., Phillips, W. D., Gould, P. L., & Metcalf, H. J. (1988). Observation of atoms laser cooled below the Doppler limit. *Physical review letters, 61*, 169.

Li, J., Zheng, J., Pan, S., Li, K., Yu, H., & Zheng, W. (2024). Metasurface-based optical system for miniaturization of atomic magnetometers. *Optics Express, 32*, 20538–20550.

Liang, Z., Zhou, B., Lu, J., Liu, Y., Hu, J., Zhou, P., . . . Ye, M. (2022). Metasurface enabled on-chip double-beam scheme for SERF atomic magnetometer. *Optics Communications, 525*, 128850.

Liew, L.-A., Knappe, S., Moreland, J., Robinson, H., Hollberg, L., & Kitching, J. (2004). Microfabricated alkali atom vapor cells. *Applied Physics Letters, 84*, 2694–2696.

Liu, H., Guo, C., Vampa, G., Zhang, J. L., Sarmiento, T., Xiao, M., . . . Reis, D. A. (2018). Enhanced high-harmonic generation from an all-dielectric metasurface. *Nature Physics, 14*, 1006–1010.

Liu, M., Zhu, W., Huo, P., Feng, L., Song, M., Zhang, C., . . . others. (2021). Multifunctional metasurfaces enabled by simultaneous and independent control of phase and amplitude for orthogonal polarization states. *Light: Science & Applications, 10*, 107.

Lorenz, V. O., Dai, X., Green, H., Asnicar, T. R., & Cundiff, S. T. (2008). High-density, high-temperature alkali vapor cell. *Review of Scientific Instruments, 79*.

Lucivero, V. G., Anielski, P., Gawlik, W., & Mitchell, M. W. (2014). Shot-noise-limited magnetometer with sub-picotesla sensitivity at room temperature. *Review of Scientific Instruments, 85*.

Mansouree, M., McClung, A., Samudrala, S., & Arbabi, A. (2021). Large-scale parametrized metasurface design using adjoint optimization. *Acs Photonics, 8*, 455–463.

Matsumae, T., Kurashima, Y., Higurashi, E., & Takagi, H. (2019). Surface activated bonding of Au/Cr, Au/Ta and Au/Pt/Ti films after degas annealing for Si/sapphire gas cell. *Microelectronic Engineering, 214*, 68–73.

McGehee, W. R., Zhu, W., Barker, D. S., Westly, D., Yulaev, A., Klimov, N., . . . McClelland, J. J. (2021). Magneto-optical trapping using planar optics. *New Journal of Physics, 23*, 013021.

McGilligan, J. P., Griffin, P. F., Elvin, R., Ingleby, S. J., Riis, E., & Arnold, A. S. (2017). Grating chips for quantum technologies. *Scientific reports, 7*, 384.

Mcguirk, J. M., Foster, G. T., Fixler, J. B., Snadden, M. J., & Kasevich, M. A. (2002). Sensitive absolute-gravity gradiometry using atom interferometry. *Physical Review A, 65*, 033608.

Nagel, H., Aberle, A. G., & Hezel, R. (1999). Optimised antireflection coatings for planar silicon solar cells using remote PECVD silicon nitride and porous silicon dioxide. *Progress in Photovoltaics: Research and Applications, 7*, 245–260.

Neuman, J. A., Wang, P., & Gallagher, A. (1995). Robust high-temperature sapphire cell for metal vapors. *Review of Scientific Instruments, 66*, 3021–3023.

Nshii, C. C., Vangeleyn, M., Cotter, J. P., Griffin, P. F., Hinds, E. A., Ironside, C. N., . . . Arnold, A. S. (2013). A surface-patterned chip as a strong source of ultracold atoms for quantum technologies. *Nature nanotechnology, 8*, 321–324.

Panda, C. D., Tao, M. J., Ceja, M., Khoury, J., Tino, G. M., & Müller, H. (2024). Measuring gravitational attraction with a lattice atom interferometer. *Nature, 631*, 515–520.

Patel, S. (2009). *A chirped, pulsed laser system and magneto-optical trap for rubidium*. Ph.D. dissertation, University of Southampton.

Prasad, A., Balakrishnan, S., Jain, S. K., & Jain, G. C. (1982). Porous silicon oxide anti-reflection coating for solar cells. *Journal of the Electrochemical Society, 129*, 596.

Ranjbar, A., & Grbic, A. (2019). Broadband, multiband, and multifunctional all-dielectric metasurfaces. *Physical Review Applied, 11*, 054066.

Rochester, S. M. (2010). *Modeling nonlinear magneto-optical effects in atomic vapors*. University of California, Berkeley.

Rosi, G., Sorrentino, F., Cacciapuoti, L., Prevedelli, M., & Tino, G. M. (2014). Precision measurement of the Newtonian gravitational constant using cold atoms. *Nature, 510*, 518–521.

Rosi, S., Burchianti, A., Conclave, S., Naik, D. S., Roati, G., Fort, C., & Minardi, F. (2018). Λ-enhanced grey molasses on the D 2 transition of Rubidium-87 atoms. *Scientific reports, 8*, 1301.

Saffman, M., Walker, T. G., & Mølmer, K. (2010). Quantum information with Rydberg atoms. *Reviews of modern physics, 82*, 2313–2363.

Sanders, D. P. (2010). Advances in patterning materials for 193 nm immersion lithography. *Chemical reviews, 110*, 321–360.

Santiago-Cruz, T., Gennaro, S. D., Mitrofanov, O., Addamane, S., Reno, J., Brener, I., & Chekhova, M. V. (2022). Resonant metasurfaces for generating complex quantum states. *Science, 377*, 991–995.

Sautter, J., Staude, I., Decker, M., Rusak, E., Neshev, D. N., Brener, I., & Kivshar, Y. S. (2015). Active tuning of all-dielectric metasurfaces. *ACS nano, 9*, 4308–4315.

Schäffner, D., Schreiber, T., Lenz, F., Schlosser, M., & Birkl, G. (2024). Quantum sensing in tweezer arrays: Optical magnetometry on an individual-atom sensor grid. *PRX Quantum, 5*, 010311.

Schinke, C., Christian Peest, P., Schmidt, J., Brendel, R., Bothe, K., Vogt, M. R., . . . others. (2015). Uncertainty analysis for the coefficient of band-to-band absorption of crystalline silicon. *Aip Advances, 5*.

Sebbag, Y., Naiman, A., Talker, E., Barash, Y., & Levy, U. (2020). Chip-scale integration of nanophotonic-atomic magnetic sensors. *ACS Photonics, 8*, 142–146.

Sebbag, Y., Talker, E., Naiman, A., Barash, Y., & Levy, U. (2021). Demonstration of an integrated nanophotonic chip-scale alkali vapor magnetometer using inverse design. *Light: Science & Applications, 10*, 54.

Sekiguchi, N., Sato, T., Ishikawa, K., & Hatakeyama, A. (2017). Spectroscopic study of a diffusion-bonded sapphire cell for hot metal vapors. *Applied Optics, 57*, 52–56.

Seong, J., Jeon, Y., Yang, Y., Badloe, T., & Rho, J. (2024). Cost-effective and environmentally friendly mass manufacturing of optical metasurfaces towards practical applications and commercialization. *International Journal of Precision Engineering and Manufacturing-Green Technology, 11*, 685–706.

Shah, V., & Romalis, M. V. (2009). Spin-exchange relaxation-free magnetometry using elliptically polarized light. *Physical Review A—Atomic, Molecular, and Optical Physics, 80*, 013416.

Shah, V., Knappe, S., Schwindt, P. D., & Kitching, J. (2007). Subpicotesla atomic magnetometry with a microfabricated vapour cell. *Nature Photonics, 1*, 649–652.

Shirmanesh, G. K., Sokhoyan, R., Wu, P. C., & Atwater, H. A. (2020). Electro-optically tunable multifunctional metasurfaces. *ACS nano, 14*, 6912–6920.

Singh, K., Anand, S., Pocklington, A., Kemp, J. T., & Bernien, H. (2022). Dual-element, two-dimensional atom array with continuous-mode operation. *Physical Review X, 12*, 011040.

Solntsev, A. S., Agarwal, G. S., & Kivshar, Y. S. (2021). Metasurfaces for quantum photonics. *Nature Photonics, 15*, 327–336.

Sorrentino, F., Ferrari, G., Poli, N., Drullinger, R., & Tino, G. M. (2006). Laser cooling and trapping of atomic strontium for ultracold atoms physics, high-precision spectroscopy and quantum sensors. *Modern Physics Letters B, 20*, 1287–1320.

Steck, D. A. (2001). Rubidium 87 D line data.

Steck, D. A. (2003). Cesium D line data.

Stern, A. G., & Cole, D. C. (2008). Design of a back-illuminated, crystallographically etched, silicon-on-sapphire avalanche photodiode with monolithically integrated microlens, for dual-mode passive & active imaging arrays. *Lidar Remote Sensing for Environmental Monitoring IX, 7153*, pp. 135–147.

Storey, P., & Cohen-Tannoudji, C. (1994). The Feynman path integral approach to atomic interferometry. A tutorial. *Journal de Physique II, 4*, 1999–2027.

Szigeti, S. S., Hosten, O., & Haine, S. A. (2021). Improving cold-atom sensors with quantum entanglement: Prospects and challenges. *Applied Physics Letters, 118*.

Talker, E., Han, Z., Dikopoltsev, M., Barash, Y., Mazurski, N., & Levy, U. (2022). High performance micrometer scale magnetometer based on dielectric metasurfaces. *2022 Conference on Lasers and Electro-Optics (CLEO)*, (pp. 1–2).

Tanuwijaya, R. S., Liang, H., Xi, J., Wong, W. C., Yung, T. K., Tam, W. Y., & Li, J. (2024). Metasurface for programmable quantum algorithms with classical and quantum light. *Nanophotonics, 13*, 927–936.

Tiecke, T. G. (2010). Properties of potassium. *University of Amsterdam, The Netherlands, Thesis*, 12–14.

Vangeleyn, M., Griffin, P. F., Riis, E., & Arnold, A. S. (2010). Laser cooling with a single laser beam and a planar diffractor. *Optics letters, 35*, 3453–3455.

Wambold, R. A., Yu, Z., Xiao, Y., Bachman, B., Jaffe, G., Kolkowitz, S., . . . Kats, M. A. (2020). Adjoint-optimized nanoscale light extractor for nitrogen-vacancy centers in diamond. *Nanophotonics, 10*, 393–401.

Wang, K., Chekhova, M., & Kivshar, Y. (2022). Metasurfaces for quantum technologies. *Physics Today, 75*, 38–44.

Wang, L., Kruk, S., Koshelev, K., Kravchenko, I., Luther-Davies, B., & Kivshar, Y. (2018). Nonlinear wavefront control with all-dielectric metasurfaces. *Nano letters, 18*, 3978–3984.

Wang, Y., Lv, Z., Qi, S., Liu, Y., & Long, H. (2022). Enhancement of light extraction efficiency of UVC-LED by SiO2 antireflective film. *Crystals, 12*, 928.

Woollam, J. A. (2012). Guide to Using WVASE® Spectroscopic Ellipsometry Data Acquisition and Analysis Software. *JA Woollam Company, Lincoln, NE, USA*.

Wright, M. J., Anastassiou, L., Mishra, C., Davies, J. M., Phillips, A. M., Maskell, S., & Ralph, J. F. (2022). Cold atom inertial sensors for navigation applications. *Frontiers in Physics, 10*, 994459.

Wu, B., Zhang, C., Wang, K., Cheng, B., Zhu, D., Li, R., . . . Zhou, Y. (2023). Marine absolute gravity field surveys based on cold atomic gravimeter. *IEEE Sensors Journal*.

Wylie, R. (2012). *The development of a multichannel atomic magnetometer array for fetal magnetocardiography*. Ph.D. dissertation, University of Wisconsin–Madison.

Xiao, Y., Yu, Z., Wambold, R. A., Mei, H., Hickman, G., Goldsmith, R. H., . . . Kats, M. A. (2021). Efficient generation of optical bottle beams. *Nanophotonics, 10*, 2893–2901.

Xu, Y., Xu, Y., Sun, J., Mao, Y., Chai, Z., & Li, J. (2024). Atomic Spin Detection Method Based on Spin-Selective Beam-Splitting Metasurface. *Advanced Optical Materials, 12*, 2301353.

Yang, W., Xiao, S., Song, Q., Liu, Y., Wu, Y., Wang, S., . . . Tsai, D.-P. (2020). All-dielectric metasurface for high-performance structural color. *Nature communications, 11*, 1864.

Yang, X., Benelajla, M., Carpenter, S., & Choy, J. T. (2023). Analysis of atomic magnetometry using metasurface optics for balanced polarimetry. *Optics Express, 31*, 13436–13446.

Yang, X., Mukherjee, P., Kim, M., Mei, H., Fang, C., Choi, S., . . . others. (2024). Atomic Magnetometry Using a Metasurface Polarizing Beamsplitter in Silicon-on-Sapphire. *ACS Photonics, 11*, 3644–3651.

Yang, Y., Kravchenko, I. I., Briggs, D. P., & Valentine, J. (2014). All-dielectric metasurface analogue of electromagnetically induced transparency. *Nature communications, 5*, 5753.

Yu, N., Genevet, P., Kats, M. A., Aieta, F., Tetienne, J.-P., Capasso, F., & Gaburro, Z. (2011). Light propagation with phase discontinuities: generalized laws of reflection and refraction. *science, 334*, 333–337.

Yu, Z., Zhu, Y., Yao, M., Qi, F., Chen, L., Zou, C.-L., . . . Liu, X. (2024). Low power consumption grating magneto-optical trap based on planar elements. *Optics Express, 32*, 8919–8928.

Yuan, L., Wu, J., & Yang, S.-J. (2023). Current Status and Prospects on High-Precision Quantum Tests of the Weak Equivalence Principle with Cold Atom Interferometry. *Symmetry, 15*, 1769.

Zhang, X., Jin, S., Qu, W., & Xiao, Y. (2021). Dichroism and birefringence optical atomic magnetometer with or without self-generated light squeezing. *Applied Physics Letters, 119*.